2019

Lipid-coated Magnesium Phosphate Nanoparticles for Intrapulmonary Protein Delivery in Mice

Mallika Vadlamudi
University of the Pacific, mallikav91@gmail.com

Recommended Citation
Vadlamudi, Mallika. (2019). *Lipid-coated Magnesium Phosphate Nanoparticles for Intrapulmonary Protein Delivery in Mice*. University of the Pacific, Dissertation. https://scholarlycommons.pacific.edu/uop_etds/3631

LIPID-COATED MAGNESIUM PHOSPHATE NANOPARTICLES FOR INTRAPULMONARY PROTEIN DELIVERY IN MICE

by

Mallika Vadlamudi

A Dissertation Submitted to the

Graduate School

In Partial Fulfillment of the

Requirements for the Degree of

DOCTOR OF PHILOSOPHY

Thomas J. Long School of Pharmacy and Health Sciences
Pharmaceutical and Chemical Sciences

University of the Pacific
Stockton, CA

2019

LIPID-COATED MAGNESIUM PHOSPHATE NANOPARTICLES FOR INTRAPULMONARY PROTEIN DELIVERY IN MICE

By

Mallika Vadlamudi

APPROVED BY:

Dissertation Advisor: Xin Guo, Ph.D.

Committee Member: Bhaskara R. Jasti, Ph.D.

Committee Member: Melanie Felmlee, Ph.D.

Committee Member: Vyacheslav Samoshin, Ph.D.

Committee Member: Raju Gadiraju, Ph.D.

Department Chair: William K. Chan, Pharm.D., Ph.D.

Dean of Graduate School: Thomas Naehr, Ph.D.

LIPID-COATED MAGNESIUM PHOSPHATE NANOPARTICLES FOR INTRAPULMONARY PROTEIN DELIVERY IN MICE

By

Mallika Vadlamudi

DEDICATION

This dissertation is dedicated to my grandfather, Prof. V. Subba Rao, who contributed to establishing pharmacy education in India.

ACKNOWLEDGMENTS

My sincere gratitude goes to Dr. Xin Guo for his continuous support and mentorship throughout my graduate studies. His constant guidance and encouragement have helped shape me into an independent researcher and develop excellent verbal and written communication skills. The work presented here could not have been accomplished without his insightful inputs. I thank my committee members, Dr. Bhaskara Jasti, Dr. Melanie Felmlee, Dr. Vyacheslav Samoshin, and Dr. Raju Gadiraju for their time, support, and invaluable suggestions on my dissertation. I am grateful for Dr. Li's constructive criticism during group meetings and my qualifying examination, which helped enhance my critical thinking. I would like to thank Dr. William Chan and Dr. John Livesey for providing access to instruments crucial for my research. I wish to express my gratitude to all the PCSP faculty for enriching my knowledge through the courses offered. I thank Lynda Davis and Kathy Kassab for their immense kindness and help on uncountable occasions.

I thank all my past and current lab mates for instilling a friendly and collaborative work environment in our lab. During my PhD, I enjoyed working with Yifan Lu on research projects, teaching assignments as well as Pacific's AAPS student chapter. I am thankful for Yifan's help, specifically for sharing his expertise in tail-vein injections. I am grateful to Yingbo Huang, for giving me a second set of hands during complex animal experiments. I thank Harshavardan Gurrala, Ruiqi Huang, Xinyu Pei, Zhongyue Yuan and Zizhao Xu for all their support and assistance in my animal experiments. It has truly been a pleasure working with all of them over the years.

I thank my friends, Michael Ng, Swetha Arikatla, Jensen Spear, Jieyun Cao, Hao Wei, Fang Liu, Dengpan Liang, Poonam Dattani, Prathyusha Naidu, Shen Zhao, Md Tariqul Tuhin, Md Rahatullah Razan, Md Zahir Uddin, Farjana Akther, Elizabeth Wilson, Jinyun Chen and Yujuan Zheng for making my time at Pacific fun and memorable.

I am blessed and grateful for the encouragement, love and support that both the Vadlamudi and Patlolla families have showered upon me. I thank my brother Ravikiran Vadlamudi for pushing me to embark on this journey. Finally, the best outcome from the past five years at Pacific was finding my best friend, Karthik Patlolla, who later became my soulmate and husband. Karthik has been an infinite source of inspiration and motivation during the challenging times of this journey. I cannot thank him enough for all the unconditional love and support.

Lipid-coated Magnesium Phosphate Nanoparticles for Intrapulmonary Protein Delivery in Mice

Abstract

By Mallika Vadlamudi

University of the Pacific
2019

Proteins are a diverse category of biomolecules with great therapeutic potential. Intracellular delivery of proteins can augment the deficient activities of dysfunctional or poorly expressed innate proteins and therefore represents a promising strategy to treat the associated diseases. One major barrier to intracellular protein delivery is the translocation of the protein across the cellular membrane. Endocytosis provides an important pathway for protein nanocarriers to enter cells across the plasma membrane. However, the cargo protein must then promptly escape from the endosomes to avoid degradation in the lysosome and to exert its cellular function.

Previously, we reported a cationic lipid-coated magnesium phosphate nanoparticle (LPP) system for intracellular protein delivery. The intracellular delivery of catalase, an antioxidant enzyme, by LPP protected MCF-7 cells from a lethal level of exogenous H_2O_2 and lowered the reactive oxygen species (ROS) levels in EA.hy926 cells. These findings prompted us to further develop LPP to evaluate its protein delivery in animals.

Two categories of LPP formulations, catalase-encapsulated (CE) LPP and catalase-complexed (CC) LPP, were successfully prepared by a modular approach.

Catalase-encapsulated liposomes (CE LP) were prepared by hydrating a thin-film of lipids with catalase solution followed by extrusion. However, extrusion of CE LP resulted in substantial loss of catalase activity. Catalase-complexed liposomes (CC LP) were prepared by first extruding cationic liposomes with a LIPEX extruder and then mixing with catalase solution. The resultant CC LP was much smaller than CE LP and preserved all the catalase activity. Magnesium phosphate nanoparticles (MgP NP) were prepared by the microemulsion precipitation technique. CE LP or CC LP were mixed with MgP NP to yield LPP formulations (CE LPP or CC LPP, respectively). The formulations were then rendered isotonic with glucose (5% w/v). Transmission electron microscopy (TEM) confirmed the proposed structure of LPP comprising a shell of lipid bilayers with a core of MgP NP. Furthermore, TEM showed drastic morphological changes of LPP formulations at acidic pH, consistent with an osmotic explosion.

The LPP formulations were administered by intravenous or intranasal routes to CD-1 mice. LPP formulations of fluorescently labeled catalase distributed substantially into the lung following intranasal administration, whereas intravenous administration of the same formulations caused catalase distribution mainly into the liver. In addition, intranasal administration of both the LPP formulations yielded higher pulmonary catalase activity and lowered the ROS levels in the healthy lung compared to free catalase solution. Based on these results, LPP's antioxidant effects were further evaluated in mice with lipopolysaccharide-induced acute lung injury (ALI).

Lack of LPP distribution into the lung following intranasal administration indicated that intranasal dosing did not deliver catalase substantially into inflamed lungs. In corroboration, the inflammatory biomarker tumor necrosis factor-alpha (TNF-α) remained unchanged after intranasal dosing of LPP formulations. Intratracheal dosing of LPP formulations delivered the fluorescently labeled catalase deep into the lung and significantly reduced TNF-α production in the inflamed lungs compared to free catalase solution. CC LPP, which was smaller and which better preserved catalase activity than CE LPP, showed greater intrapulmonary catalase activity compared to CE LPP in both healthy and inflamed lungs. Taken together, LPP represents a promising nanocarrier for intracellular protein delivery.

TABLE OF CONTENTS

Chapter 5: Evaluation of the Potential Therapeutic Efficacy of LPP in a Murine Inflammatory Lung Disease Model 105

LIST OF TABLES

Table

LIST OF FIGURES

Figure

LIST OF ABBREVIATIONS

ALI	Acute lung injury
ARDS	Acute respiratory distress syndrome
AuNP(s)	Gold nanoparticles
BALF	Bronchoalveolar lavage fluid
CC LP	Catalase-complexed liposomes
CC LPP	Catalase-complexed lipid-coated magnesium phosphate nanoparticles
CE LP	Catalase-encapsulated liposomes
CE LPP	Catalase-encapsulated lipid-coated magnesium phosphate nanoparticles
Chol	Cholesterol
COPD	Chronic obstructive pulmonary disease
CRISPR	Clustered regularly interspaced short palindromic repeats
Cas9	CRISPR associated protein 9
D	Hydrodynamic diameter
DLS	Dynamic light scattering
DOTAP	1,2-dioleoyl-3-trimethylammonium-propane
ELISA	Enzyme-linked immunosorbent assay
f-CC LPP	Fluorescent catalase-complexed lipid-coated magnesium phosphate nanoparticles
f-CE LPP	Fluorescent catalase-encapsulated lipid-coated magnesium phosphate nanoparticles
Free CAT	Free catalase in solution
Free f-CAT	Free fluorescent catalase in solution
FRET	Forster resonance energy transfer
IL-6	Interleukin-6
IN	Intranasal
IT	Intratracheal

IV	Intravenous
L-f-CAT	Liposomal formulation of fluorescent catalase
L-CAT	Liposomal formulation of catalase
LPP	Lipid-coated magnesium phosphate nanoparticles
LPS	Lipopolysaccharide
MgP NP	Magnesium phosphate nanoparticles
MSN(s)	Mesoporous silica nanoparticles
NLC(s)	Nanostructured lipid carriers
PBS	Phosphate-buffered saline (pH 7.4)
PDI	Polydispersity index
PECAM	Platelet-endothelial cell adhesion molecule
PEG	Polyethylene glycol
PTA	Phosphotungstic acid
RES	Reticuloendothelial system
ROS	Reactive oxygen species
SLN(s)	Solid lipid nanoparticles
TEM	Transmission electron microscopy/microscope
T-PER	Tissue protein extraction reagent
TS	Tissue supernatant

Chapter 1: Introduction

1.1 Protein Therapeutics: Advantages and Challenges

Proteins represent a large, complex and diverse category of biomolecules that have great therapeutic potential. Since the development of human insulin, recombinant protein therapy has been extensively investigated. Compared to small molecule drugs, proteins can achieve higher specificity, more complex functions, higher biocompatibility and lower immune responses [1]. Recombinant protein therapeutics may also overcome drawbacks associated with gene therapy, such as oncogenic effects of viral gene vectors and undesirable immune responses [2]. On average, clinical development and FDA approval are faster for protein therapeutics than small molecule drugs [1]. Currently, most of the commercially available proteins therapeutics are being used for extracellular targets [3].

Intracellular delivery of proteins can augment the deficient activities of dysfunctional or poorly expressed innate proteins and therefore represents a promising strategy to treat the associated diseases. Moreover, proteins can be delivered into cells to counter a number of pathological developments such as inflammation, oxidative stress, neurodegeneration, and cancer cell growth [4, 5]. One major barrier of intracellular protein delivery is the translocation of the protein across cellular membranes. Endocytosis is the main mechanism for cellular uptake and trafficking across the plasma membrane (Fig. 1). Cellular uptake mechanisms such as clathrin-mediated endocytosis, phagocytosis, micropinocytosis and caveolae-mediated endocytosis often lead to varying levels of degradation, exocytosis or endosomal escape

[3]. The early endosome serves as a major sorting station, where the endocytosed protein is either recycled back to the plasma membrane or sorted into the late endosome for degradation in the lysosome [6]. During the maturation process, a stable pH gradient is maintained in different endosomal compartments: early endosomes at pH 6.5; late endosomes at pH 5.5; and lysosomes at pH 4.5 [7].

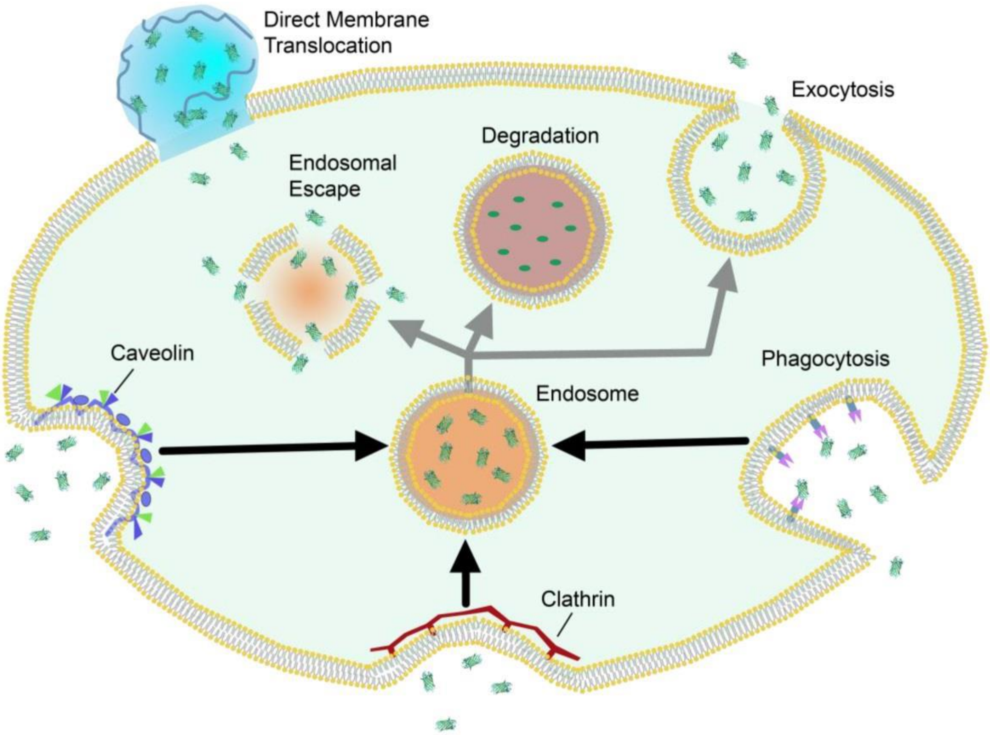

Fig. 1.1. Illustration of selected intracellular trafficking mechanisms and their generalized pathways (Adapted from ref. [3])

Although endocytosis provides an important pathway for protein delivery systems to enter the cells across the plasma membrane, the cargo protein must then promptly escape from the endosomes to exert its cellular function, and to avoid degradation in the lysosome [8, 9]. Furthermore, the large size, delicate structure and excess surface charge of most proteins subject them to denaturation, enzymatic deactivation, clearance by the reticuloendothelial system (RES), or elimination by renal filtration. These hurdles have inspired the development of numerous strategies for intracellular protein delivery.

1.2 Current Protein Delivery Systems

Nanocarriers are colloidal delivery systems whose diameter is in the nanometer range. Over the past decade, various nanocarrier systems based on polymers, inorganic compounds, proteins or lipids have been developed to enhance the intracellular delivery of their cargo proteins [3, 10]. Nanocarriers can protect the cargo proteins from denaturation, enzymatic degradation and renal/hepatic elimination, thereby improving their stability in blood circulation. Nanocarriers can also be rendered to have physicochemical properties (e.g. suitable size, shape, charge, surface coating, grafting of targeting ligands, etc.) that enhance the distribution of the cargo proteins to the target site [11, 12].

1.2.1 Inorganic nanoparticles. Inorganic nanocarriers composed of silica are commonly used delivery systems due to their versatility and flexibility [3]. Bale *et al.* [13] functionalized silica nanoparticles with a hydrophobic n-octadecyltrimethoxysilane moiety on their surface to immobilize functional proteins by hydrophobic interactions. These hydrophobic silica nanoparticles delivered ribonuclease A and an antibody against phospho-Akt intracellularly to initiate cell death in MCF-7 breast cancer cells as well as rat neural stem cells [13].

Silica nanoparticles that contain networks of mesopores (aka, mesoporous silica nanoparticles, MSNs) are capable of encapsulating both small and/or large molecules. MSNs are potentially advantageous in a) promoting high cargo adsorption/loading by their large surface area and high pore volume, b) controlling release kinetics by adjusting the pore size, c) enabling targeted delivery by modifying their surface, d) allowing simultaneous drug delivery and imaging by loading a combination of therapeutic cargo with magnetic and/or luminescent compounds and e) promoting bone regeneration due to their excellent surface properties and porosity [14]. In a recent study, Lin *et al.* [15] used MSNs for synergistic co-delivery of superoxide dismutase and glutathione peroxidase to help scavenge reactive oxygen species (ROS) in HeLa cells. In another study, Yang *et al.* [16] reported an MSN nanocarrier coated with a fusogenic lipid bilayer that promoted MSN's fusion with cell membranes for intracellular protein delivery. The cargo protein cytochrome C, loaded in the MSN core was delivered into the cytosol, as indicated by the apoptosis of HeLa cells. Yuting *et al*. [17] studied the advantage of roughened silica nanoparticles, whose surface was subjected to octadecyl-decorated hydrophobic modifications, in cellular uptake by MCF-7 and SCC-25 cells when compared to smooth silica nanoparticles. In this study, the authors demonstrated that both roughness and surface functionalization contributed to enhanced cellular uptake, and only the latter triggered enhanced endosomal release of the cargo protein to the cytosol.

Gold nanoparticles (AuNPs) are another type of inorganic nanocarriers that have been widely investigated as delivery platforms for both large and small molecules due to the non-toxic characteristic of gold, and the ease of surface functionalization in these nanocarriers [3]. Functionalized AuNPs have been studied for the intracellular delivery of β-Galactosidase, a 473 KDa, negatively charged membrane-impermeable enzyme [18]. In this study, AuNPs delivered the functional protein into HeLa cells as monitored by an X-Gal enzymatic activity assay. In another study, Mout *et al.* [19] fabricated a two-component protein-AuNP nanoassembly, which was evaluated for intracellular delivery of multiple fluorescent proteins. The fluorescent signal from these proteins spread into the cytosol followed by quick nuclear uptake, indicating the presence of a transient membrane-fusion based mechanism for direct intracellular protein delivery.

AuNPs have also been explored to deliver proteins for genome editing, where the Cas-9 protein, guide RNA and donor DNA need to be delivered simultaneously as a genome editing machinery. Clustered, regularly interspaced short palindromic repeats (CRISPR) associated with protein 9 (Cas9) has the potential to revolutionize the treatment of genetic diseases by correcting genetic mutations. Lee *et al.* [20] developed a 'CRISPR-Gold' nanocarrier system to deliver the CRISPR/Cas9 genome editing machinery into the cells by endocytosis followed by polymer-mediated endosomal release. The CRISPR-Gold complex was coated with a cationic polymer to improve the biological stability and the ability to disrupt the endosome. CRISPR-Gold demonstrated 5.4% efficiency in a Duchenne muscular dystrophy murine model, where the animals showed enhanced muscular capability in response to the repair of the dystrophin mutation [20].

1.2.2 Polymeric nanocarriers. Polymeric nanocarriers include micelles, nanogels, nanospheres, nanofibers, rods, vesicles, capsules and dendrimers. They are versatile structures that can be engineered to obtain high loading efficiency, tunable release kinetics and targeted delivery. Proteins can directly interact with or be encapsulated into polymeric nanocarriers. Polymeric micelles are often designed to facilitate triggered release in response to stimuli such as pH, temperature or chemical triggers such as glucose concentration [21].

Gao *et al.* [22] developed a negatively charged pH-sensitive micelle using a degradable block copolymer methoxy poly(ethylene glycol)-poly(β-amino ester) with piperidine and imidazole rings, which remained negatively charged under physiological pH to increase its circulation time and turned positively charged under acidic conditions to promote its cellular uptake. After intravenous administration of such polymeric micelles that were labeled with Cy5.5 and loaded with albumin, near-infrared fluorescence imaging showed selective accumulation of the micelles in the ischemic area of the brain in rats.

Polymeric nanogels were loaded with both β-galactosidase and a lipophilic small molecule, which were then delivered concurrently into HeLa cells [23]. Shi *et al.* [24] studied the influence of PEGylation of catalase in a mouse model of H1N1 influenza-induced pneumonia. The PEGylation increased the half-life and enhanced the therapeutic efficacy of native catalase in the disease model.

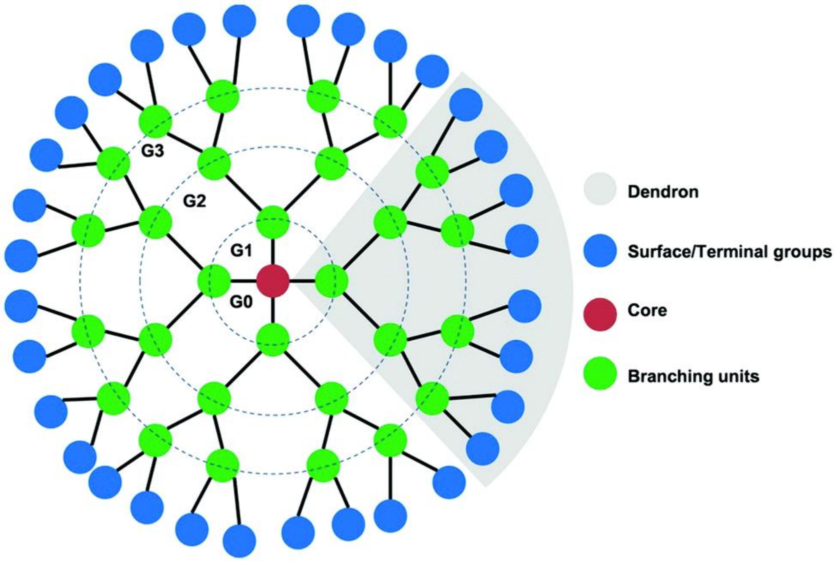

Fig. 1.2. Schematic of the molecular structure of a dendrimer (Adapted from ref. [25])

Dendrimers are polymeric molecules that are repetitively branched in a spherical manner (Fig. 1.2). Dendrimers have been investigated as delivery systems for both small and large molecules. Fluorinated dendrimers have been investigated by Lv *et al.* for their ability to self-assemble and to deliver a variety of proteins (albumin, β-galactosidase, saporin and a cyclic hendecapeptide) into the cytosol of HeLa cells [26, 27]. The lead A6-2/saporin fluorodendrimer-protein complex, which was coated with anionic hyaluronic acid, suppressed tumor growth in a murine model of breast cancer [26]. Dendrimers that are functionalized by guanidinobenzoic acid have also been reported to promote the intracellular delivery of R-phycoerythrin and β-galactosidase in HeLa cells [28].

1.2.3 Lipid-based nanocarriers. Lipid-based nanocarriers such as liposomes, lipoplexes, solid lipid nanoparticles (SLNs) and nanostructured lipid carriers (NLCs) have been investigated as delivery systems for both small and large molecules.

Liposomes are lipid assemblies of spherical vesicles that contain a shell of lipid bilayers, which can entrap hydrophobic cargo molecules, and an aqueous core, where hydrophilic drugs can be encapsulated. Liposomes are versatile nanocarriers, whose size, charge, lipid composition and surface can be engineered to assume desirable characteristics for drug delivery (Fig. 1.3). Due to their modularity and ease of preparation, liposomes have been widely used for intracellular delivery of antibodies, enzymes and cytokines [10]. Sarker *et al.* [29] studied the intracellular delivery efficiency of lysine-based cationic liposomes and confirmed that it delivered albumin and antibodies labeled with FITC into the cytosol of HeLa cells by confocal laser scanning microscopy. The complexes were endocytosed by a caveolae-mediated mechanism based on inhibition experiments [29]. Kim *et al.* [30] developed a targeted and PEGylated lipid nanocarrier consisting of cationic lipids (DOTAP/DOPE), apolipoprotein and DSPE-PEG to deliver cytochrome C into cancer cells. The authors reported massive apoptosis in H460 cells treated with the cytochrome C lipid nanocarriers. Additionally, the nanocarriers selectively accumulated in the tumor tissue and provoked tumor regression in a mouse xenograft model after intravenous administration.

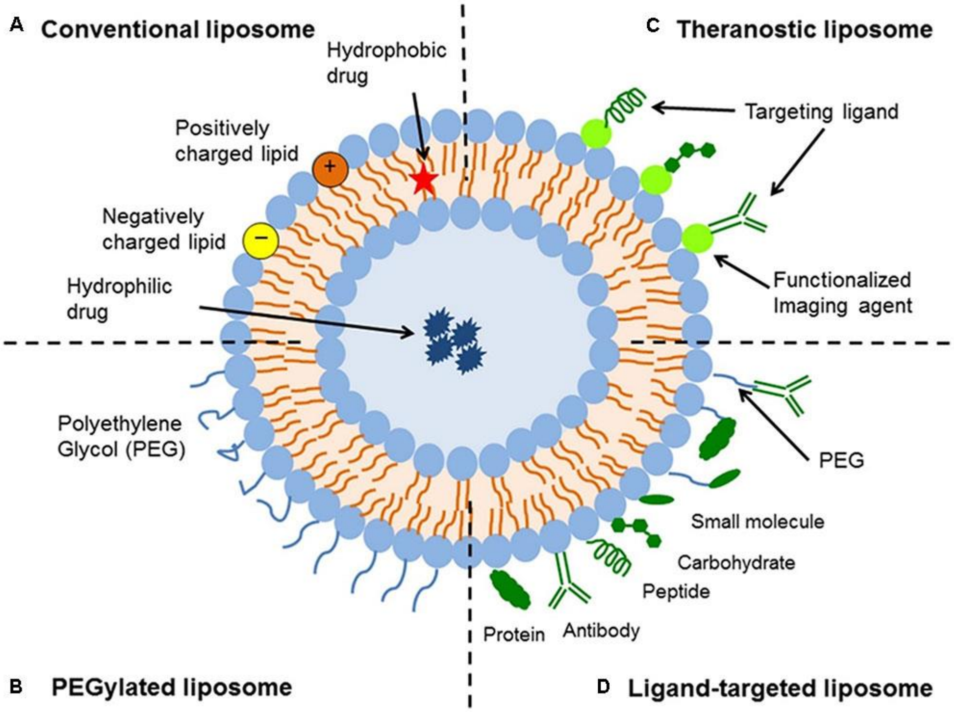

Fig. 1.3. Schematic representation of a conventional liposome (A), PEGylated liposome (B), theranostic liposome (D) and a ligand-targeted liposome (D) (Adapted from ref. [31])

Cationic lipids are often employed in the nanocarriers designed for protein or gene delivery because a) they can enhance loading efficiency by electrostatic interaction with negatively charged proteins, DNA or RNA molecules and b) they can facilitate cellular uptake by interacting with the negatively charged cell membrane and by triggering endocytosis. Yamaguchi *et al.* [32] demonstrated that a mixture of commercially available cationic lipid reagent (BioPORTER) and Wr-T transporter peptide aided cytosolic delivery of a variety of proteins into HeLa and MRC-5 cells. Another study reported a guanidinium-based cationic liposome that delivered functional β-galactosidase and anti-cytokeratin8 antibodies into HeLa cells [33]. Although liposomal encapsulation of proteins can improve their cellular uptake, there is a risk of protein activity loss during the preparation steps including extrusion and freeze-thawing [34].

Solid lipid nanoparticles (SLNs) are made of lipids that are solid at body temperature, and of emulsifiers for stability. SLNs can be prepared by high-pressure homogenization, solvent emulsification-evaporation, microemulsion, and spray drying techniques [35]. SLNs are advantageous in protecting the cargo protein from the environment, ease of scale-up, biocompatibility and biodegradability with the use of appropriate lipids. However, their crystalline structure can hinder drug loading, expulse the loaded drug during storage, or trigger polymorphic transitioning coupled with accelerated drug release [36]. In contrast to SLNs, nanostructured lipid carriers (NLCs) consist of lipids in both solid and liquid phases. As a result, NLCs have an unstructured lipophilic matrix that can overcome SLN's limitation of drug expulsion at high drug-loading capacity. Almeida *et al.* [37] evaluated SLNs as antigen carriers using lysozyme as a model protein. The authors reported that lysozyme loaded into SLNs retained its stability even after being subjected to the harsh high-pressure homogenization procedure. Another study reported that lysozyme loaded into SLNs that consisted of triglycerides or diglycerides exhibited a lipase-mediated, degradation-based release, which would find applications in oral delivery of peptides/proteins [38].

The foregoing review shows that extensive progress has been made over the last decade, which leads to several promising strategies to deliver proteins. Most of these strategies have shown successful applications at a cellular level. However, they are still far from clinical application. The biodistribution and toxicity of nanocarriers are influenced by their composition, colloidal properties and administration route, thus emphasizing the need to comprehensively evaluate the nanocarriers in disease models *in vivo* in order to make them safe enough for clinical applications [10, 14].

1.3 Cationic Lipid-coated Magnesium Phosphate Nanoparticles (LPP)

Previously, we reported a cationic lipid-coated magnesium phosphate nanoparticule (LPP) delivery system for intracellular protein delivery [39].

1.3.1 Proposed mechanism of endosomal escape. LPP is a novel protein delivery system comprising a shell of concentric cationic lipid bilayers, a core of magnesium phosphate nanoparticle (MgP NP) and the cargo protein, catalase, an ubiquitous antioxidant enzyme [40].

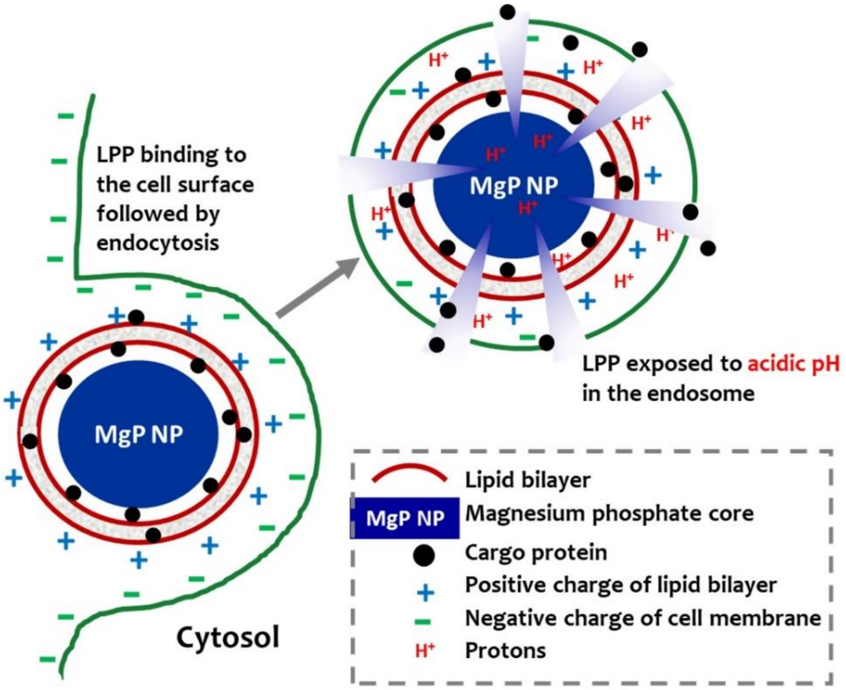

Fig. 1.4. Illustration of the proposed intracellular protein delivery mechanism by LPP (Adapted from ref. [39])

Fig. 1.4 illustrates the proposed mechanism of intracellular delivery of catalase by LPP. The cationic lipids on the LPP surface would first interact with the negatively charged cell membrane to trigger endocytosis. The MgP NP core of LPP would then dissolve in response to the acidic pH inside the endosome to form a high-salt solution, which would then elevate the osmotic pressure in the endosome. This induces water influx and consequently the swelling and destabilization of the endosome, thereby releasing the cargo catalase into the cytosol [41].

1.3.2 *In vitro* activities of LPP. The reported LPP formulation of catalase carried a diameter of 250 nm and was positively charged with a ζ-potential of 46 mV. LPP showed sensitivity to a mildly acidic pH of 5.5, at which a higher amount of catalase was released from the nanoparticles, than at a neutral pH of 7.4 (Fig. 1.5a). TEM images confirmed its osmotic explosion in response to acidic pH (Fig. 1.5c, d), demonstrating that LPP could destabilize endosomes to facilitate intracellular delivery of catalase.

Treatment by the LPP formulation protected MCF-7 cells from H_2O_2-induced cell death (Fig. 1.6a). Additionally, LPP lowered the ROS levels in EA.hy926 cells by more than 40% of the untreated-media control (Fig. 1.6b). Both the cellular experiments indicated that LPP successfully delivered functional catalase into the cell. Overall, the LPP system is a viable protein nanocarrier that could find potential clinical applications.

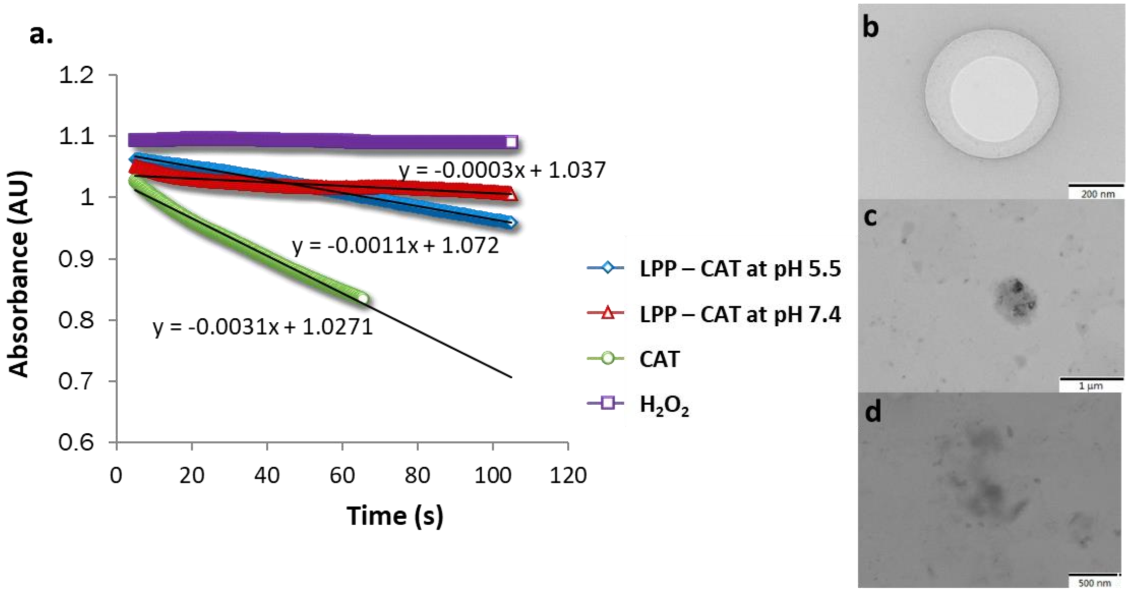

Fig. 1.5. pH-dependent decomposition of H_2O_2 by LPP (a) and TEM images of LPP at pHs 7.4 (b) and 5.5 (c, d) (Adapted from ref. [39])

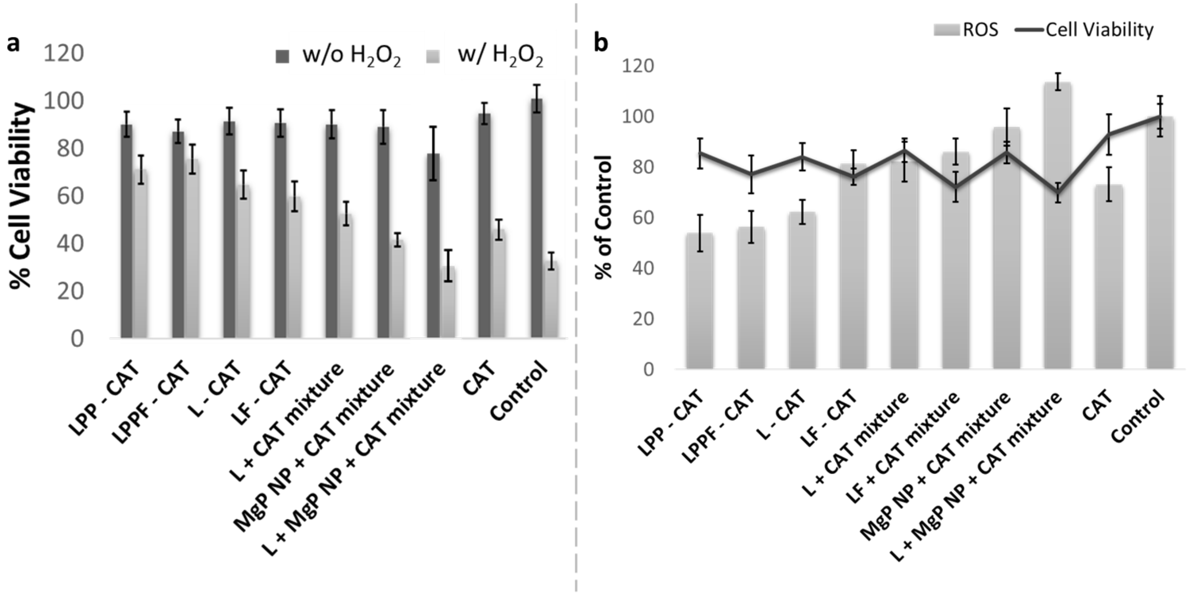

Fig. 1.6. Protection of MCF-7 cells from lethal exogenous hydrogen peroxide (H2O2) (a) and ROS-scavenging in EA.hy926 cells (b) by various formulations of catalase in media with serum (Adapted from ref. [39])

1.4 *In vivo* Evaluation of LPP

Such promising findings of LPP in cell culture prompted us to further develop LPP to evaluate its biodistribution, potential therapeutic benefits and toxicity in animals. Lung was chosen as the target tissue for this dissertation because pulmonary diseases such as chronic obstructive pulmonary disease (COPD), acute lung injury (ALI), acute respiratory distress syndrome (ARDS), asthma, pneumonia and bronchitis are all associated with inflammation and oxidative stress [42-44] while catalase, the prototype cargo protein of LPP, is an endogenous antioxidant enzyme that is important for regulating oxidative stress in inflammation [45-47].

1.4.1 Factors influencing *in vivo* protein delivery. The fate of a nanocarrier system *in vivo* is influenced by several factors including the route of administration and the composition and colloidal properties of the LPP, which usually determine its *in vivo* stability.

1.4.1.1 Route of administration. Selecting the optimal route of administration is crucial for achieving enough nanocarrier/drug distribution at the target tissue for a therapeutic response. Nanocarriers are commonly delivered intravenously and then passively accumulate at sites of enhanced vascular permeability, a characteristic of nanocarriers under several disease conditions including cancer, inflammation and infection [48, 49]. Cationic lipid-based nanocarriers have been reported to mainly accumulate in pulmonary capillaries following IV administration [50, 51]. However, nanocarriers administered systemically are prone to rapid clearance by RES or non-specific distribution into other tissues resulting in a weaker therapeutic effect and more side effects. Alternatively, direct administration into the target tissue, whenever feasible, is advantageous because of quicker onset of action and reduced systemic side effects [52]. For example, direct intrapulmonary delivery using nasal sprays and medicated inhalers is a commonly used approach to relieve congestion and constriction of the airways in respiratory diseases. However, nanocarriers administered by this route need to overcome the innate defense mechanism of the lungs, which include respiratory mucus, mucociliary clearance, exhalation, expulsion by coughing, and uptake by alveolar macrophages [53, 54]. Pulmonary route has also been investigated for its potential in non-invasive systemic protein delivery due to the large absorptive surface area, extremely thin mucosal membrane, and good blood circulation in the lung [55].

1.4.1.2 Colloidal properties

1.4.1.2.1 Size. The size of nanocarriers plays a major role in its tissue distribution, cellular uptake by endocytosis, phagocytic uptake and renal clearance. After administration into the systemic circulation, nanocarriers smaller than 200 nm in diameter are capable of extravasation through the highly permeable capillary blood vessels in inflamed tissues, provided they circulate long enough in the blood circulation. Phagocytosis is sensitive to particle size, and nanocarriers smaller than 0.26 μm in diameter can evade uptake by macrophages [56]. Conversely, nanocarriers that are too small (<6 nm in diameter) are prone to be excreted quickly by the kidneys. Following intrapulmonary administration, particles smaller than 0.5 μm in diameter deposit deep into the alveolar region by diffusion [54]. However, these particles are subjected to exhalation, phagocytosis by macrophages or endocytosis by epithelial cells, which constitute the lungs defense mechanism of maintaining its mucosal surfaces [57].

1.4.1.2.2 Surface charge. The surface charge of nanocarriers also influences their vulnerability to phagocytosis, endocytosis, opsonization and renal elimination. Generally, nanocarriers with a high positive or negative charge are colloidally stable on shelf because the charges prevent aggregation by electrostatic repulsion [58]. Positive charges are beneficial in promoting cellular uptake. However, positively charged nanocarriers are vulnerable to opsonization, recognition and clearance by RES following intravenous administration [59]. On the contrary, positively charged lipophilic aerosolized compounds have been reported to preferentially bind to lung tissue following intrapulmonary administration [60].

1.4.1.2.3 Surface coating. Nanocarriers that are administered intravenously seldom reach the target tissue partly due to clearance by the RES. Opsonins interact with nanocarriers through electrostatic, ionic, van der waals, hydrophobic/hydrophilic forces [61], and highly charged hydrophobic nanocarriers are more susceptible to opsonization. In order to avoid opsonization, the surface of the nanocarriers can be modified with a hydrophilic polymer, such as PEG, to prolong the half-life of nanocarriers in blood circulation [62].

1.5 Hypothesis and Specific Aims

The purpose of this dissertation is to develop LPP formulations that are suitable for *in vivo* applications and to evaluate their protein delivery efficiency in both healthy and diseased animals. Our hypothesis is that lipid-coated magnesium phosphate nanoparticles can facilitate intrapulmonary delivery of proteins. To test our hypothesis, the following specific aims were devised for this dissertation:

1. To prepare, optimize and characterize lipid-coated magnesium phosphate nanoparticles (LPP) for *in vivo* application.
2. To study the morphology of LPP using transmission electron microscopy (TEM).
3. To evaluate the protein delivery efficiency of LPP in healthy mouse lung.
4. To evaluate the potential therapeutic efficacy of LPP in a murine inflammatory lung disease model.

Chapter 2: Preparation and Physicochemical Characterization of Lipid-coated Magnesium Phosphate Nanoparticles for *in vivo* Application

2.1 Introduction

2.1.1 The components of lipid-coated magnesium phosphate nanoparticles. Lipid-coated magnesium phosphate nanoparticles (LPP) consists of three components: concentric cationic lipid bilayers on the surface, a magnesium phosphate nanoparticle (MgP NP) core and the cargo protein, catalase (Fig. 2.1).

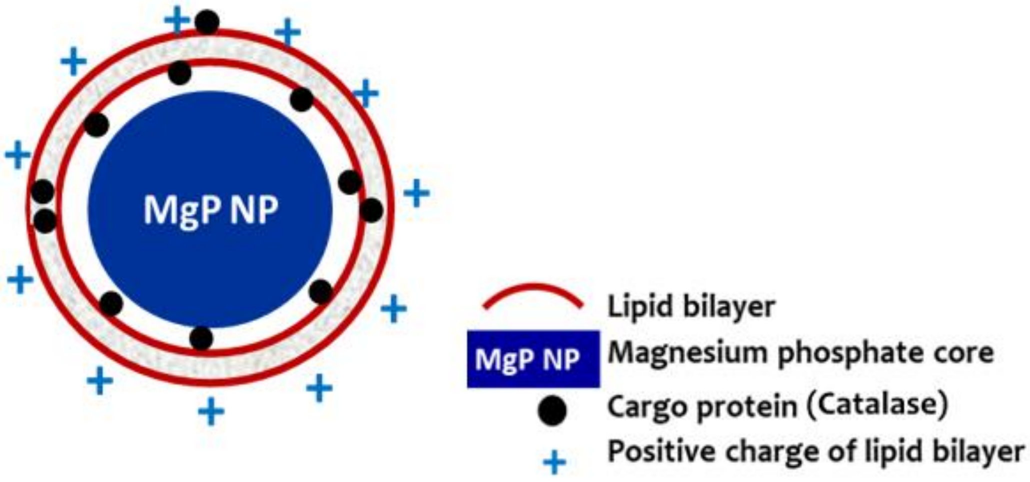

Fig. 2.1. Proposed structure of the LPP construct

2.1.1.1 Cationic lipid DOTAP. Liposomal nanocarriers are spherical vesicles composed of lipid bilayer(s) surrounding an aqueous interior. Liposomes may carry a positive, negative or a neutral surface charge based on the hydrophilic headgroup of the lipid amphiphile used. Cellular uptake of liposomes is mediated by adsorption onto the cell surface and subsequent endocytosis [63]. The positive surface charge imparted by the cationic lipids improve the adsorption of the liposomes onto the negatively charged cell membrane due to electrostatic interactions. Notably, during the endosomal maturation phase, cationic lipids can fuse with the endogenous anionic lipids present in the endosomal membrane to facilitate cytosolic release of the entrapped liposomal cargo [64]. The commercially available cationic lipid, 1,2-dioleoyl-3-trimethylammonium-propane (DOTAP) (Fig. 2.2) is widely used for nucleic acid and protein delivery in *in vitro* and *in vivo* systems [65]. In our study, DOTAP was used for the construction of the cationic liposome and the LPP formulations.

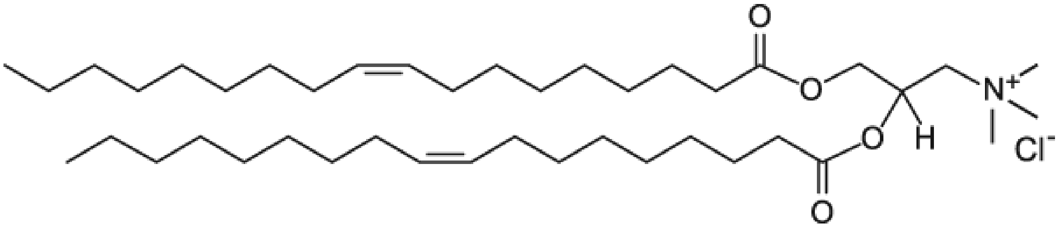

Fig. 2.2. Chemical structure of DOTAP

As previously reported, DOTAP is an important component of LPP that influences the formation of the LPP construct [39]. The cationic lipid facilitates encapsulation and/or adsorption of the negatively charged cargo protein to yield catalase-loaded liposomes. Additionally, the excessive positive charges of catalase-loaded liposomes also facilitate the coating of MgP NP with the liposome.

2.1.1.2 Magnesium phosphate nanoparticle core. Calcium phosphate nanoparticles have been investigated for the intracellular delivery of nucleic acids, proteins and small molecules for decades [66, 67]. The delivery is facilitated by the dissolution of calcium phosphate nanoparticles in the acidic compartment of endosomes, which causes the swelling and bursting of the endosomes to release the entrapped cargo. An example of one such system is the calcium phosphate nanoparticles coated with cationic lipids for systemic delivery of siRNA, reported by Li *et al.* [68].

Magnesium phosphate and calcium phosphate have similar chemical properties as both magnesium and calcium are group IIA metals and the solubility of both compounds increases at acidic pH [69, 70]. However, the free cytosolic calcium concentration in healthy cells is about 100 nM and the influx of excess calcium ions into the cytosol can induce various cytotoxic events such as opening of mitochondrial permeability transition pores, disruption of cytoskeletal organization, and activation of apoptotic cascades [71]. In contrast, the cytosolic magnesium concentration in healthy cells is much higher ranging from 0.1 mM to 3 mM [72] and is less likely to be perturbed by the exogenous magnesium from the MgP NP core of LPP [73]. Additionally, cattiite ($Mg_3(PO_4)_2 \cdot 22H_2O$), the main component of the MgP NP core is generally considered biocompatible, biodegradable and nontoxic [74]. Therefore, as a safer alternative to calcium phosphate, MgP NP was chosen for the LPP core.

2.1.1.3 Catalase payload. Catalase is a heme protein that catalyzes the conversion of hydrogen peroxide to water and oxygen. It is a tetramer (Fig. 2.3), with each monomer containing a heme group that binds oxygen. It is an endogenous protein found in most living cells exposed to oxygen and protects the cells from oxidative stress. In this study, bovine liver catalase was used as the model cargo protein, which has a molecular weight of 250 KDa.

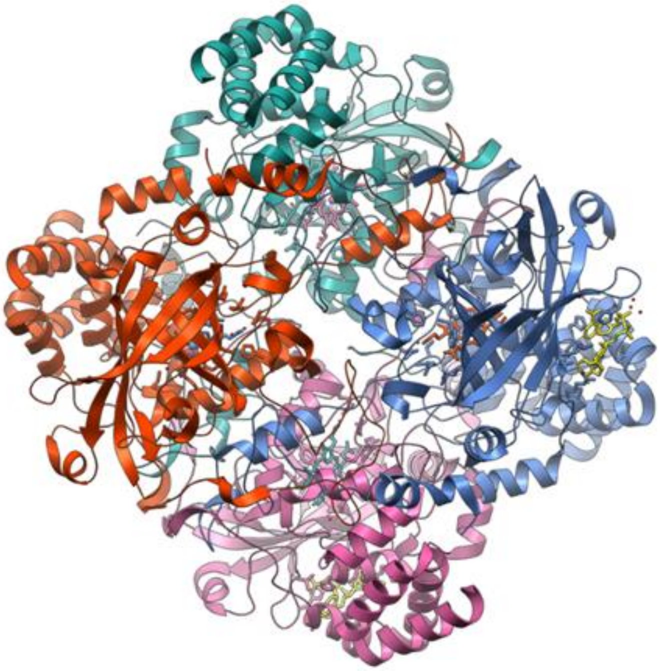

Fig. 2.3. Tetrameric structure of catalase (Adapted from ref. [75])

The net charge of a protein is neutral at its isoelectric point (pI), positive when pH<pI and negative when pH>pI [76]. Catalase carries a pI of 5.4. Therefore, it carries negative charges at pH 7.4 and interacts with the positively charged lipids to facilitate the protein loading during LPP preparation.

2.1.2 Factors influencing formulations for protein delivery *in vivo*. The aim of this chapter is to prepare LPP formulations for *in vivo* applications. In order to do so, the following factors were taken into consideration.

2.1.2.1 Colloidal size, charge and stability. As discussed in the previous chapter, colloidal properties of nanocarriers play an important role in its stability in blood circulation, tissue distribution, cellular uptake, and clearance by renal and hepatic pathways. Nanocarriers with diameters ranging from 10 – 200 nm are ideal for enhancing tissue distribution and prolonging circulation in the blood because, they are small enough to evade phagocytosis by macrophages and large enough to avoid excretion by renal filtration [54, 56].

Aggregation of nanocarriers would significantly alter their pharmacokinetics, biodistribution, cellular uptake and toxicity [77]. Therefore, the colloidal stability of nanocarriers is not only important for its storage, but also for determining its behavior *in vivo*. Excess positive charges imparted by the cationic lipid DOTAP would improve the colloidal stability of LPP on shelf by preventing aggregation due to electrostatic repulsion [58]. Furthermore, the cationic charges of LPP may also influence its tissue distribution according to Yeeprae *et al.* [78], who demonstrated that cationic liposomes comprising of DOTAP and cholesterol rapidly accumulated in the lung within a minute after intravenous injection.

2.1.2.2 Catalase loading: encapsulation vs complexation. In addition to colloidal stability, stability of the catalase cargo is also crucial. In our previous report, catalase-encapsulated liposomes (CE LP) were prepared by thin-film hydration followed by a single extrusion through a 200 nm membrane [39]. Because repetitive extrusion of CE LP would risk substantial loss of protein activity, it was avoided. The drawback of this approach is the relatively large size of the resultant CE LPP at a diameter around 240 nm, making it more prone to clearance by mononuclear phagocytes [79]. Therefore, an alternative method of loading catalase onto the liposomes was attempted in this dissertation research, where the cationic liposomes were first extruded and then mixed with the negatively charged catalase to form catalase-complexed liposomes (CC LP). The complexation method allowed the liposomes to be formed separately in smaller size by multiple extrusions without compromising the activity of the cargo catalase [80]. We speculated that the catalase loaded into CE LP would mostly be encapsulated inside the aqueous core and any unloaded catalase would complex to its cationic surface (Figure 2.4a). Conversely, CC LP would be associated with the cargo catalase mostly by electrostatic adsorption on the liposome surface (Fig. 2.4b).

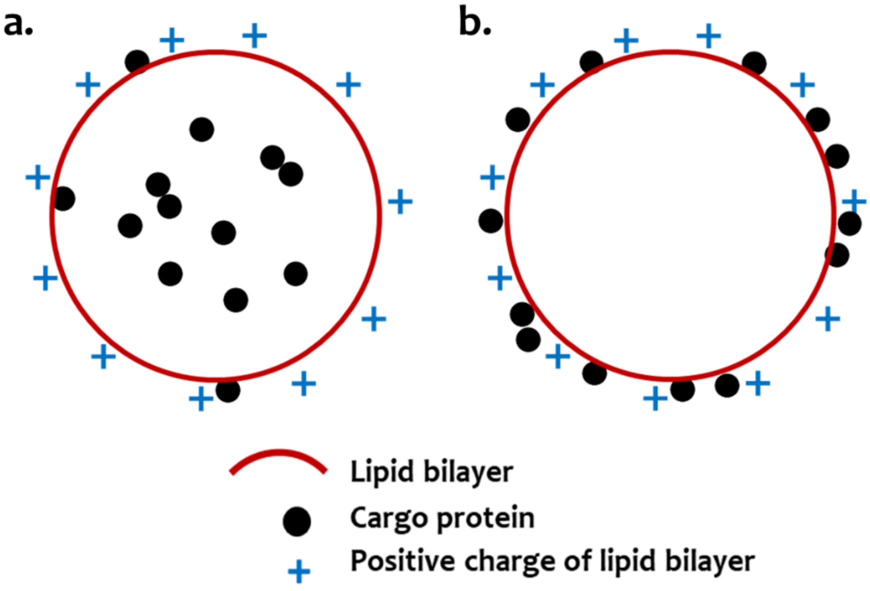

Fig. 2.4. Schematic representation of CE LP (a) and CC LP (b)

2.1.2.3 Lipid molar ratio. The percentage of cholesterol in a liposome influences its size, fluidity and encapsulation efficiency. Lowering the amount of cholesterol helps in reducing the size, while improving encapsulation efficiency [81]. In order to prepare cationic liposomes of reduced size, the lipids of the cationic liposomes, DOTAP/Cholesterol were tested at three molar ratios: 1/1, 6/4 and 7/3, where the 7/3 molar ratio yielded cationic liposomes of the smallest hydrodynamic diameter (Table 2.1)[80]. Additionally, the pre-formed liposomes increased in size after being mixed with catalase, indicating the formation of a catalase-liposome complex. Both the cationic liposomes and the catalase-complexed liposomes at 7/3 molar ratio of DOTAP/Cholesterol maintained the same hydrodynamic diameter for up to 120 hours [80].

Table 2.1. Hydrodynamic diameter (D) and polydispersity index (PDI) of cationic liposomes and liposome-catalase complexes at different lipid ratios (Adapted from ref. [80])

DOTAP/ Cholesterol Molar Ratio	**Before Extrusion**		**After Extrusion**		**After Complexing w/ Protein**	
	D (nm)	**PDI**	**D (nm)**	**PDI**	**D (nm)**	**PDI**
1:1	1860 ± 462.3	0.6 ± 0.2	298.4 ± 62.2	0.5 ± 0.1	298.4 ± 62.2	0.5 ± 0.1
6:4	1376.2 ± 571.8	0.4 ± 0.0	129.5 ± 4.6	0.1 ± 0.0	177.2 ± 42.8	0.2 ± 0.1
7:3	645.6 ± 69.1	0.7 ± 0.1	84.0 ± 9.8	0.1 ± 0.0	108.7 ± 8.2	0.2 ± 0.0

2.1.2.4 Isotonicity. Formulations prepared for *in vivo* administration need to be isotonic with animal cells. Tonicity is a relative term that describes how one solution compares to the other in terms of osmolarity. Administering a hypotonic solution can lead to swelling of cells, whereas, hypertonic solutions can cause shrinking of cells. Both these cases may interfere with normal cellular function and lead to toxicity. Therefore, to have the same osmolarity as animal cells, the isotonicity of formulations is usually adjusted to be equivalent to 0.9% salt (NaCl) or 5% sugar (glucose, dextrose).

The objective of the research reported in this chapter was to prepare and optimize isotonic LPP formulations of catalase to have physicochemical characteristics suitable for *in vivo* application.

2.2 Materials and Methods

2.2.1 Materials. 1,2-dioleoyl-3-trimethylammonium-propane (DOTAP) was purchased from Avanti Polar Lipids (Alabaster, AL). Cholesterol, magnesium chloride, glucose, sodium chloride, sodium phosphate, sodium citrate, HEPES, acetic acid, triton-X100, 1-hexanol, absolute ethanol and silica gel (60–200 mesh) were purchased from Fisher Scientific (Hampton, NH). Cyclohexane, H_2O_2 (35% w/w in H_2O), bovine liver catalase (E3289) was purchased from Sigma-Aldrich (St. Louis, MO). Cyanine 7.5 labeled bovine liver catalase was purchased from Nanocs Inc (New York, NY).

2.2.2 Modularized preparation of LPP. To enable efficient optimization of the properties of LPP formulations, a modular approach was used to construct LPP. The preparation process involved three modules:

1. Preparation of cationic liposomes loaded with catalase
2. Preparation of magnesium phosphate nanoparticles (MgP NP)
3. Preparation of lipid-coated magnesium phosphate nanoparticles loaded with catalase

2.2.2.1 Module 1: Preparation of cationic liposomes loaded with catalase

2.2.2.1.1 Extrusion of catalase-encapsulated liposomes. Catalase-encapsulated liposomes (CE LP) were prepared by thin-film hydration followed by extrusion (Fig. 2.5). A solution of 10 µmol total lipids (DOTAP/cholesterol, 1/1 mol/mol) in chloroform was rotavaporated followed by evaporation under high vacuum for at least 4 hours to remove residual solvent. The lipid film was then hydrated in 0.875 mL 0.7 µM catalase solution in HEPES buffer (5mM, pH 7.4) using mild vortexing. The resultant lipid suspension was extruded thrice through a porous polycarbonate membrane (200 nm pore diameter, Nucleopore, Pleasanton, CA) by a Mini-Extruder (Avanti Polar Lipids, Alabaster, AL) to obtain a suspension of liposomes that were loaded with catalase at lipid/catalase molar ratio of ~1.6×10^4. All the steps were carried out at room temperature.

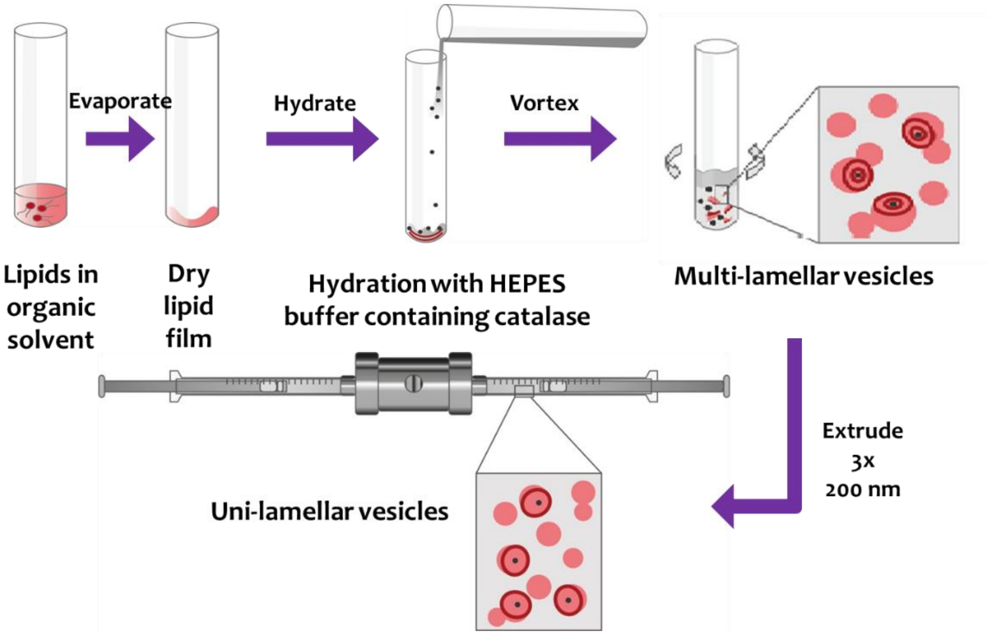

Fig. 2.5. Illustration of liposome preparation by film hydration and extrusion

2.2.2.1.2 Preparation of catalase-complexed liposomes. As an alternative approach to load the cargo protein catalase, cationic liposomes of reduced size were first prepared and then mixed with catalase in solution. Cationic liposomes were prepared by two methods: 1) thin-film hydration followed by extrusion and 2) microfluidic mixing.

To prepare cationic liposomes by extrusion, 10 μmol total lipids (DOTAP/cholesterol, 7/3 mol/mol) were mixed in chloroform, transferred into a glass tube and evaporated as described above. The resultant lipid films were hydrated with 0.875 mL HEPES buffer (5mM, pH 7.4) without catalase, agitated on vortex and then extruded sequentially through polycarbonate membranes either using a handheld Mini-Extruder (Avanti Polar Lipids, Alabaster, AL) or a LIPEX™ extruder (Evonik Industries, BC, Canada) at room temperature.

The NanoAssemblr Benchtop (Precision Nanosystems, Vancouver, BC) was used to prepare cationic liposomes by microfluidic mixing (Fig. 2.6). The microfluidic cartridge of the NanoAssemblr contained two inlets and one outlet connected by internal channels that promote non-turbulent laminar mixing of the organic (lipids in ethanol) and aqueous (HEPES buffer, 5mM, pH 7.4) phases. Disposable syringes were used to pump the two phases into the inlets of the cartridge and the liposome suspension was collected into a 15 mL tube at the outlet. The NanoAssemblr software allows the adjustment of the total flow rate (TFR) and the flow rate ratio (FRR), two important parameters that influence the size distribution of the liposomes. The resultant liposomal suspension was dialyzed overnight in a Slide-A-Lyzer™ dialysis cassette (MWCO 10K) immersed in HEPES buffer (5mM, pH 7.4) to remove ethanol. One liter of dialysate was used for 1 mL of sample. After overnight dialysis, the sample was collected and stored at 4 °C.

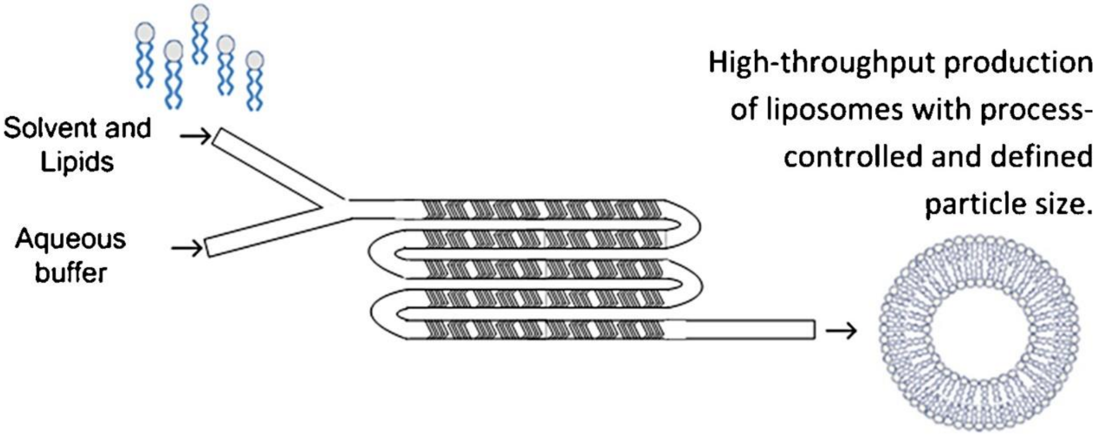

Fig. 2.6. Illustration of liposome preparation by microfluidics. (Adapted from ref. [82])

A 500 µL aliquot of the liposome suspension produced by extrusion or microfluidics was then mixed with a catalase solution at a lipid/catalase molar ratio of ~1.6 × 10^4.

2.2.2.2 Module 2: Preparation of magnesium phosphate nanoparticles. Magnesium phosphate nanoparticles (MgP NP) were prepared by microemulsion precipitation (Fig. 2.7) as previously described [39] with modifications. Briefly, aqueous solutions of $MgCl_2$ (500 mM, 300 µL) and Na_3PO4 (500 mM, 300 µL) were each transferred into a mixture of cyclohexane/Triton-X100/hexanol (75/15/10 v/v/v, 15mL) followed by 30 min stirring at 4 °C to form reverse water-in-oil micro-emulsions. The two resultant microemulsions were then mixed quickly with continuous stirring for another 30 min to generate MgP NP suspended in the water-in-oil emulsion. Sodium citrate (15 mM, 250 µL) was then added dropwise to coat the MgP NP with negative surface charges. The resultant micro-emulsion containing the MgP NP was poured into a suspension of 4 g silica gel in ethanol (100 mL) and was stirred continuously for 10 min to break the water-in-oil emulsion in order to let the MgP NP adsorb onto the silica gel beads. The suspension was then packed into a short column and washed with 200 mL ethanol to remove the organic solvents and the surfactant Triton-X100. The column was then eluted with a decreasing ethanol gradient (15 mL 75% ethanol, 15 mL 50% ethanol, and 30 mL 25% ethanol in water) to separate the MgP NP. Ethanol in the eluant fractions was then removed by rotary evaporation to yield the nanoparticle suspensions in water. The amount of MgP NP in the aqueous suspensions were quantified by a phosphorus assay as described below [83].

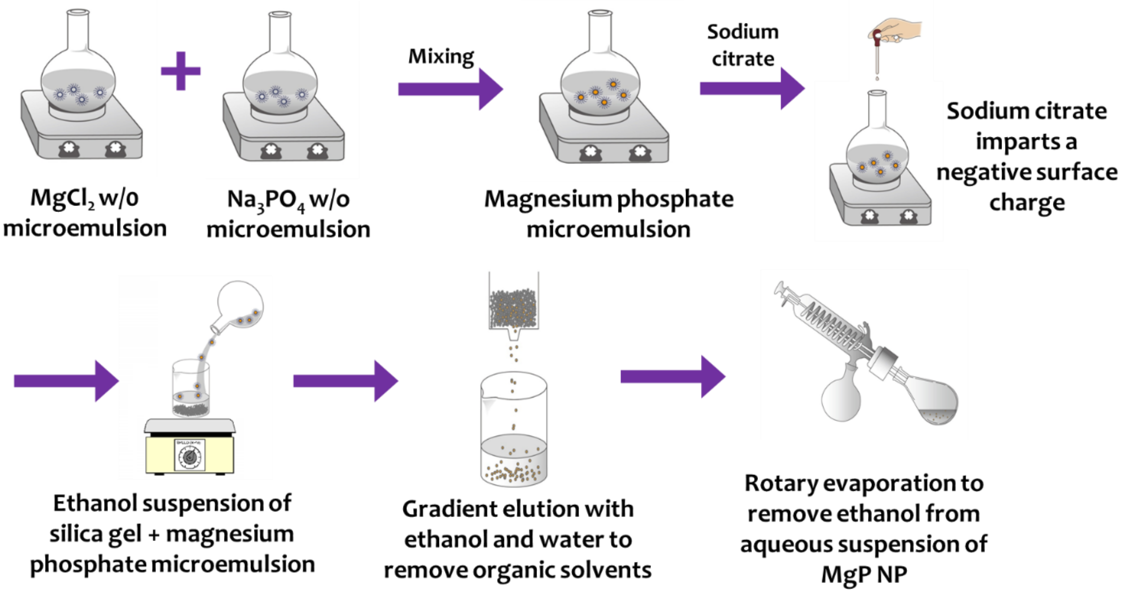

Fig. 2.7. Diagrammatic representation of magnesium phosphate nanoparticles preparation

2.2.2.2.1 Phosphorous assay. A solution of 10 N H_2SO_4 was prepared by slowly adding 28.1 mL of stock H_2SO_4 (35 N) to 100 mL of deionized (DI) water. H_2O_2 (10% w/v) was freshly prepared before each experiment by diluting 0.43 mL of stock H_2O_2 (35% w/w) with 1.5 mL of DI water. Ascorbic acid solution (10%) was prepared by dissolving 750 mg ascorbic acid in 7.5 mL DI water. Molybdate reagent was prepared by dissolving 154 mg of ammonium molybdate tetrahydrate in 1.75 mL of 10 N H_2SO_4 and diluted to 70 mL with DI water.

Aliquots of a phosphorous standard solution (50 ppm, Ricca Chemical, Fisher Scientific, Hampton, NH) were transferred into eight Pyrex tubes with screw caps to make phosphorous solutions of the calibration curve as follows: Blank (0 nmol, 0 µL), S1 (25 nmol, 15.5 µL), S2 (50 nmol, 31 µL), S3 (75 nmol, 46.5 µL), S4 (100 nmol, 61.9 µL), S5 (125 nmol, 77.4 µL), S6 (150 nmol, 92.9 µL) and S7 (200 nmol, 123.9 µL). Each unknown sample was prepared by adding 20 µL of a MgP NP suspension to the bottom of a Pyrex tube. H_2SO_4 (10 N, 0.4 mL) was then added to each Pyrex tube and heated on an aluminum block under the fume hood at 200-210 °C for 60 minutes. The tubes were then removed from the block and allowed to cool at room temperature for 10 minutes. H_2O_2 (10%, 0.1 mL) was added to each tube and the tubes were heated again at 190-210 °C for 10 minutes followed by cooling at room temperature for 10 minutes. Thereafter, molybdate reagent (4.7 mL) and ascorbic acid (10%, 0.5 mL) were added to each tube, and the tubes were agitated on a vortex for 10 seconds. The tubes were then heated at 100 °C for 10 minutes, when a blue color was developed in tubes containing substantial phosphate. The tubes were then cooled on ice to reach room temperature quickly. An aliquot (200 µL) from each tube was transferred into a 96-well plate in triplicates and the absorbance (λ = 800 nm) was determined on an Epoch Microplate Spectrophotometer (BioTek Instruments Inc, Winooski, VT). All the standards and unknowns were corrected for blank absorbance. A standard calibration curve was generated and used to estimate the amount of phosphorus in the unknown MgP NP samples.

2.2.2.3 Module 3: Preparation of lipid-coated magnesium phosphate nanoparticles loaded with catalase. To prepare the final LPP formulations, CE LP (Fig. 2.8a) or CC LP (Fig. 2.8b) (0.6 mL) were mixed with an appropriately diluted MgP NP suspension (0.4 mL) at room temperature followed by mild agitation on a vortex to obtain LPP (CE LPP or CC LPP, respectively) at a total lipid/phosphate molar ratio of 7/3. The LPP formulations were stored at 4 °C for further use. The final CC LPP and CE LPP formulations carried 5.9 mM total lipid, 2.5 mM phosphate and 0.37 μM catalase.

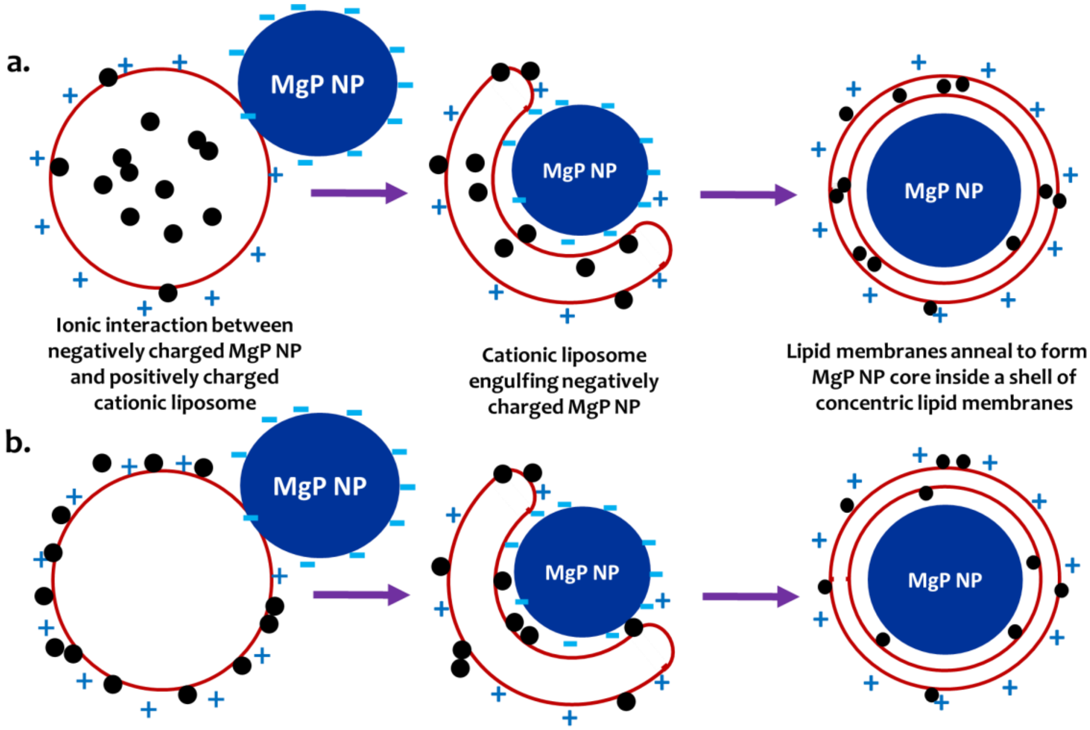

Fig. 2.8. Schematic representation of the formation of CE LPP (a) and CC LPP (b)

2.2.3 Preparation of isotonic LPP formulations

2.2.3.1 Preparation of LPP in an isotonic buffer. Both CE LPP and CC LPP formulations were prepared as per the three modules described above (2.2.2), with one modification. Isotonic HEPES buffer (5mM HEPES, 149 mM NaCl, pH 7.4) was used instead of the low salt HEPES buffer (5mM, pH 7.4) for preparing catalase solutions and hydrating lipid films.

2.2.3.2 Adjustment of isotonicity after preparation. CE LPP and CC LPP were first prepared as described above (2.2.2) using low salt HEPES buffer (5mM, pH 7.4). The LPP formulations were then concentrated using an Amicon® Ultra-4 mL centrifugal filter (MWCO 10K). Briefly, 4 mL of LPP suspension was added into the Amicon filter tube and centrifuged at 4000g, 4 °C on a Beckman GS-6R centrifuge (Beckman Coulter Inc, Brea, CA) for 1-2 hours to concentrate the suspension to 2 mL. The concentrated sample was recovered and separated into two parts of 1 mL each. To one part, 1 mL of 556 mM glucose solution was added and to the other part, 1 mL of 298 mM NaCl dissolved in HEPES buffer (5mM, pH 7.4) was added to obtain final isotonic LPP formulations containing either 278 mM (5%) glucose or 154 mM (0.9%) salt.

2.2.4 Physicochemical characterization of LPP

2.2.4.1 Size measurement. Dynamic Light Scattering measurements were performed on a Zetasizer Nano ZS (Malvern Instruments, Malvern, UK) as previously reported [39, 84]. A diluted aliquot (50 µL) of LPP formulations or their precursors in HEPES buffer (5 mM, pH 7.4) was transferred into a low volume cuvette (ZEN0118, Malvern Instruments) and the hydrodynamic diameter (weighing by the light intensity) was measured in triplicates.

2.2.4.2 ζ-potential measurement. After measuring the size, the sample in the cuvette was diluted to 0.8 mL with HEPES buffer (5mM, pH 7.4) and slowly added to a disposable cuvette (DTS1070, Malvern Instruments) to ensure that the sample covered the anodes of the cell without any air bubbles. The ζ-potential of each sample was measured in triplicates on a Zetasizer Nano ZS (Malvern Instruments, Malvern, UK).

2.2.4.3 Catalase activity assay. The loading and stability of payload catalase in the LPP formulations were measured using a Catalase Assay Kit (Cayman Chemical, Ann Arbor, MI) per the manufacturer's protocol. Catalase formulations were diluted ~75-fold to a final catalase concentration of 5 nM to fit into the linear range of the assay. Percentage of catalase activity in the LPP formulations was calculated by:

$$\text{Catalase activity \%} = \frac{\text{Catalase activity measured in the formulation}}{\text{Catalase activity measured in catalase solution used for loading}} * 100$$

2.5 Results

2.5.1 Effect of extrusion on catalase encapsulated in cationic liposomes.

After hydrating the DOTAP/cholesterol (1/1 mol/mol) lipid film with a catalase solution (lipid/protein = 1.6 x 10^4 mol/mol), the resultant suspension was extruded multiple times (1, 3, 5, 7, 13) through a 200 nm polycarbonate membrane to yield catalase-encapsulated liposomes (CE LP). Repetitive extrusion caused substantial loss of protein activity (Fig. 2.9). This was probably because the process exerted substantial mechanical stress that partially denatured the protein. Even a single extrusion through 200 nm membrane resulted in more than 10% activity loss. 3x extrusion was chosen as it was enough to homogenize the size (233 nm with a PDI of 0.2) of CE LP, while retaining about 60% of the catalase activity.

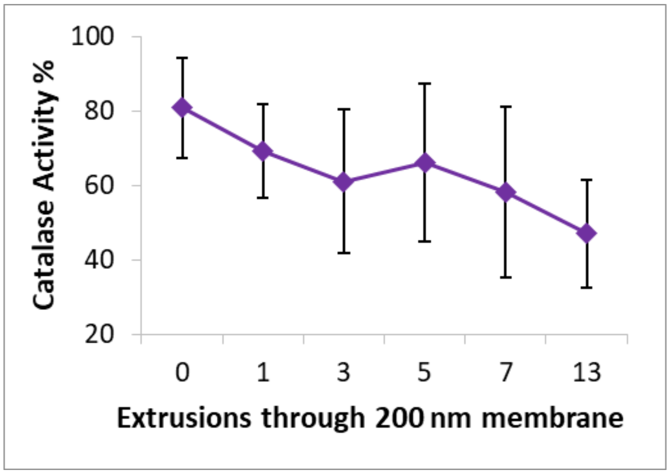

Fig. 2.9. Effect of extrusion on catalase loaded into CE LP. Data presented as mean ± SD (n=3).

2.5.1.1 Effect of lipid molar ratio (5/5 vs 7/3). Previously, we found that a DOTAP/cholesterol molar ratio of 7/3 formed smaller unloaded cationic liposomes, which were then complexed with catalase (Table 2.1)[80]. To test how the 7/3 lipid molar ratio would influence CE LP, the process described in the previous section (2.5.1) was repeated by hydrating and extruding a DOTAP/cholesterol (7/3 mol/mol) lipid film. The 7/3 lipid molar ratio indeed reduced the size of liposomes compared to 5/5 lipid molar ratio (columns in Fig. 2.10). However, the 7/3 lipid molar ratio also caused greater catalase activity loss in that even one single extrusion through 200 nm membrane caused about 70% loss of the catalase activity (lines in Fig. 2.10). Because the liposomes with 7/3 (DOTAP/cholesterol) lipid molar ratio have a higher concentration of the cationic lipid DOTAP, the catalase may have been complexed to the lipid rather than being encapsulated within the aqueous core, making it more susceptible to the mechanical stress from the extrusion. Therefore, a DOTAP/cholesterol molar ratio of 1/1 was used for encapsulating catalase (CE LP) and a DOTAP/cholesterol molar ratio of 7/3 was used for complexing catalase (CC LP) in this dissertation.

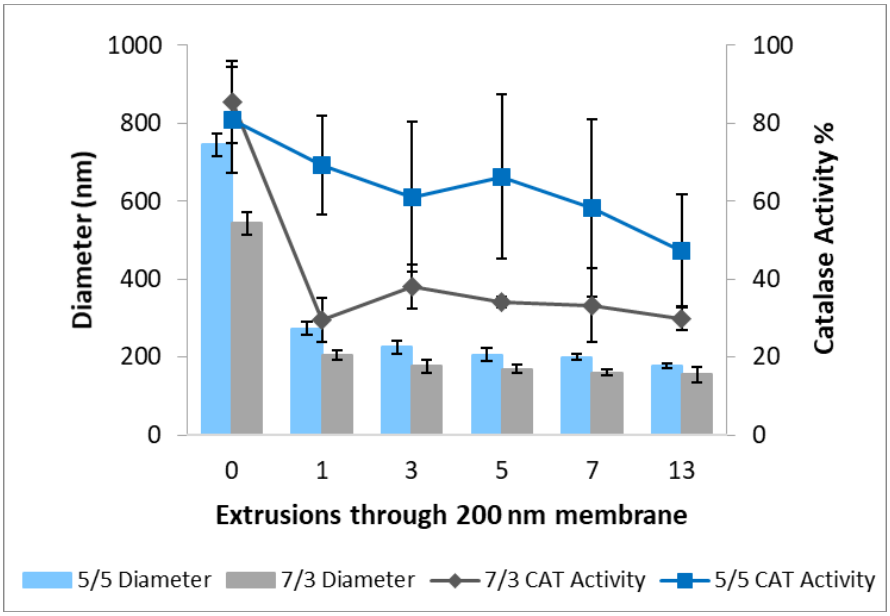

Fig. 2.10. Effect of extrusion on CE LP at different lipid ratios. Data presented as mean ± SD (n=3).

2.5.2 Procedure optimization for cationic liposomes. The complexation loading approach, where unloaded cationic liposomes were first prepared followed by mixing with catalase, allowed us to subject the liposomes to multiple extrusions and to achieve reduced sizes without compromising the activity of the cargo protein catalase. The colloidal properties of the cationic liposomes prepared using a manual hand-held extruder, a LIPEX extruder and a benchtop NanoAssemblr (microfluidics) were compared.

2.5.2.1 Extrusion with Mini-Extruder. The DOTAP/cholesterol (7/3 mol/mol) lipid films were hydrated with HEPES buffer (5mM, pH 7.4) and extruded 13 times each through 400 nm, 200 nm, 100 nm and 50 nm polycarbonate membranes using a hand-held Mini-Extruder (Avanti Polar Lipids, Alabaster, AL). The resultant liposomes carried an average diameter of 80 nm with a PDI of 0.11 (Table 2.2).

Mini-extruder is very useful when extruding small sample volumes <500 µL, however, 1 mL is the maximum volume that can be extruded each time. The resistance increases when extruding through lower pore size membranes, especially 50 nm, making it very difficult to push the syringe plunger. Applying excess pressure to overcome this resistance, often results in membrane damage or sample leakage.

Table 2.2. Hydrodynamic diameter (D) and ζ-Potential of cationic liposomes prepared using a mini-extruder

#	Composition	Membranes Used (nm)	Number of Extrusions	D (nm)	PDI	ζ-Potential (mV)
1	DOTAP/Chol (7/3 mol/mol)	400	13	233.6	0.198	
2	DOTAP/Chol (7/3 mol/mol)	400 + 200	13 + 13	171.2	0.123	
3	DOTAP/Chol (7/3 mol/mol)	400 + 200 + 100	13 + 13 + 13	120.3	0.12	
4	DOTAP/Chol (7/3 mol/mol)	400 + 200 + 100 + 50	13 + 13 + 13 + 13	80.4	0.11	48.6

2.5.2.2 Extrusion with LIPEX extruder. After hydrating the DOTAP/cholesterol (7/3 mol/mol) lipid film with HEPES buffer (5mM, pH 7.4), the lipid suspension was extruded using a LIPEX^{TM} extruder (Evonik Industries, Burnaby, BC), which uses controlled nitrogen gas pressure to push the lipid suspension through the membrane(s). As shown in Table 2.3, several trials were made with different combinations of membranes and increasing number of extrusions. The best and reproducible outcome was obtained by first extruding the liposomes 5x through 200/100 nm membranes (200 nm stacked on 100 nm, 240 psi pressure) followed by 5x extrusion through 80/50 nm membranes (80 nm stacked on 50 nm, 280 psi pressure). The resultant liposomes carried an average diameter of 62 nm with a PDI of 0.135.

In comparison to manual extrusion, the LIPEX extruder can handle 1-10 mL of volume each time and is very easy to use. Furthermore, LIPEX extruder is the current industry standard for liposome preparation and is capable of scale-up to 100-800 mL for GMP production of early-stage clinical products. However, the pumping of the nitrogen gas must not be too fast or unsteady to avoid the formation of a milky paste.

Table 2.3. Hydrodynamic diameter (D) and ζ-Potential of cationic liposomes prepared using a LIPEX extruder

#	Composition	Membranes Used (nm)	Number of Extrusions	D (nm)	PDI	ζ-Potential (mV)
1	DOTAP/Chol (7/3 mol/mol)	200/100/100	1	194.3	0.264	76.6
2	DOTAP/Chol (7/3 mol/mol)	200/100/100	5	144.2	0.204	72.7
3	DOTAP/Chol (7/3 mol/mol)	200/100/100	10	130.4	0.174	65.5
4	DOTAP/Chol (7/3 mol/mol)	200/100/100	15	126.4	0.144	64.1
5	DOTAP/Chol (7/3 mol/mol)	200/100/100	10	97.18	0.119	44.3
6	DOTAP/Chol (7/3 mol/mol)	200/100 + 50	13 + 5	81.15	0.364	
7	DOTAP/Chol (7/3 mol/mol)	200/100 + 50 + 100	13 + 5 + 3	77.1	0.264	
8	DOTAP/Chol (7/3 mol/mol)	200/100 + 50 + 100	13 + 5 + 13	66.99	0.183	
9	DOTAP/Chol (7/3 mol/mol)	200/100	13	108.7	0.122	
10	DOTAP/Chol (7/3 mol/mol)	200/100 + 80	13 + 5	88.47	0.111	39.2
11	DOTAP/Chol (7/3 mol/mol)	200/100	5	117.3	0.164	
12	DOTAP/Chol (7/3 mol/mol)	200/100 + 80/50	5 + 5	77.28	0.161	
13	DOTAP/Chol (7/3 mol/mol)	200/100 + 80/50/100	5 + 5	146.8	0.502	
14	DOTAP/Chol (7/3 mol/mol)	200/100 + 80/50	5 + 5	65.82	0.135	33.3
15	DOTAP/Chol (7/3 mol/mol)	200/100 + 80/50	5 + 5	62.21	0.135	32.1

2.5.2.3 Microfluidic mixing with NanoAssemblr. NanoAssemblr Benchtop (Precision Nanosystems, Vancouver, BC) was used to prepare cationic liposomes by microfluidic mixing. Lipids in ethanol were mixed with HEPES buffer (5mM, pH 7.4) in a controlled manner using a microfluidic cartridge. As shown in Table 2.4, multiple batches of liposomes were prepared by using different total flow rate (TFR) and flow rate ratio (FRR) settings. Finally, a flow ratio of 2.5/1 (HEPES buffer/20mM total lipids in ethanol) at a total flow rate of 12 mL/min was chosen. The resultant liposomes carried an average diameter of 125.8 nm and a low PDI of 0.06, indicating a high degree of homogeneity. The liposomes shrunk to 69.3 nm after overnight dialysis in HEPES buffer (Table 2.5). A similar degree of shrinking was observed in all the samples that were dialyzed and may have been caused by the loss of anhydrous ethanol from the liposomal sample.

The NanoAssemblr Benchtop instrument uses a proprietary microfluidic mixing technology which enables us to precisely control size by optimizing flow rates and flow ratios. It can be easily scaled-up to meet preclinical and clinical (GMP) production requirements. However, in our week-long experience of using the Benchtop instrument (1-week DEMO), we found that our results were not reproducible (see #9, 14, 15, 16 in Table 2.4) even though we used the same settings, probably due to the overuse of the cartridge. The microfluidic cartridge is compatible with a limited set of organic solvents and has a short lifetime. Each cartridge needs to be replaced after 20 sample runs of 2 mL each, which makes this procedure very expensive compared to extrusion.

Table 2.4. Hydrodynamic diameter (D) of cationic liposomes prepared using a NanoAssemblr Benchtop

#	Composition	Total lipid (mM in ethanol)	Nanoassemblr settings				Final liposomes (mM total lipid)	D (nm)	PDI
			Total Volume (mL)	FRR		TFR (mL/ min)			
				HEPES (5mM, pH 7.4)	Ethanol				
DEMO		10 mg/mL	1	1.5 (PBS)	1	12	4mg/mL	101.3	0.07
1	DOTAP/Chol (7/3 mol/mol)	40	4	3	1	18	10	38.7	0.15
2	DOTAP/Chol (7/3 mol/mol)	40	4	3	1	12	10	39.7	0.13
3	DOTAP/Chol (7/3 mol/mol)	40	4	3	1	12	10	42.9	0.11
4	DOTAP/Chol (7/3 mol/mol)	40	1	3	1	6	10	34.9	0.18
5	DOTAP/Chol (7/3 mol/mol)	40	1	3	1	1	10	34.7	0.19
6	DOTAP/Chol (7/3 mol/mol)	40	1	1.5	1	12	16	209.1	0.26
7	DOTAP/Chol (7/3 mol/mol)	20	1	2	1	12	6.7	161.5	0.11
8	DOTAP/Chol (7/3 mol/mol)	20	1	2	1	18	6.7	169.1	0.10
9	DOTAP/Chol (7/3 mol/mol)	20	1	2.5	1	12	5.7	79.8	0.18
10	DOTAP/Chol (7/3 mol/mol)	20	1	2.75	1	12	5.3	61.1	0.34
11	DOTAP/Chol (7/3 mol/mol)	20	1	3	1	12	5	64.5	0.25
12	DOTAP/Chol (7/3 mol/mol)	20	4	3	1	18	5	48.9	0.34
13	DOTAP/Chol (7/3 mol/mol)	20	4	2.75	1	12	5.3	55.4	0.16
14	DOTAP/Chol (7/3 mol/mol)	20	1.25	2.5	1	12	5.7	70.4	0.27
15	DOTAP/Chol (7/3 mol/mol)	20	2.5	2.5	1	12	5.7	87.0	0.26
16	DOTAP/Chol (7/3 mol/mol)	20	10.5	2.5	1	12	5.7	125.8	0.06

Table 2.5. Hydrodynamic diameter (D) and ζ-Potential of cationic liposomes before and after dialysis

#	Before dialysis			After dialysis		
	D (nm)	**PDI**	**ζ-Potential (mV)**	**D (nm)**	**PDI**	**ζ-Potential (mV)**
1	38.7	0.15	20.8	19.6	0.15	30.6
3	42.9	0.11		18.9	0.16	
13	55.4	0.16		38.5	0.38	
15	87.0	0.26		41.9	0.24	
16	125.8	0.06	34.5	69.3	0.07	48.9

2.5.3 Physicochemical characteristics of LPP and its components.

Catalase encapsulated liposomes (CE LP) carried a hydrodynamic diameter of 233 nm, which is slightly larger than the 200 nm pore size of the polycarbonate membrane (Table 2.6). CE LP also carried a polydispersity index (PDI) of 0.2 and a ζ-potential at 53 mV, indicating excess positive charges on its surface. Cationic liposomes (LP) that were extruded to prepare for CC LP carried a reduced hydrodynamic diameter of 82 nm with a PDI of 0.12. The cationic liposomes increased in size after being mixed with catalase, indicating the formation of a catalase-liposome complex. Additionally, the ζ-potential of the catalase complexed liposomes (CC LP) was slightly neutralized by the adsorption/complexation of negatively charged catalase onto the liposome surface. MgP NP prepared as per Module 2 displayed a relatively large cumulative hydrodynamic diameter of 400 ± 67 nm with a ζ-Potential of -10 ± 2 mV, confirming the negative surface charges imparted by sodium citrate coating [41]. The final CE LPP and CC LPP formulations carried ζ-Potentials of 40 ± 2 mV and 31 ± 2 mV, respectively, which were slightly lower than those of CE LP and CC LP (53 ± 5 and 40 ± 4 mV, respectively).

This supported the working hypothesis that the formation of the LPP formulations (module 3) upon mixing the catalase-loaded liposomes (CE LP or CC LP) with MgP NP was driven by electrostatic interactions, where the anionic MgP NP partially neutralized the excess positive charge of the cationic liposomes. The resultant complexed formulation (CC LPP) had a hydrodynamic diameter of 141 ± 15 nm, which is about half of the encapsulated formulation (CE LPP), whose diameter was 284 ± 37 nm.

Intriguingly, both the LPP formulations displayed smaller diameters than one of their two components, MgP NP. This phenomenon could be attributed to the following two factors. First, MgP NP suspension is a heterogenous mixture of both small, tight nanoparticles and their loose aggregates, together displaying a hydrodynamic diameter of around 400 nm. This was later confirmed under a transmission electron microscope, where both small nanoparticles and their large aggregates were observed (Chapter 3, Fig. 3.1). As MgP NP and CE LP/CC LP were mixed with stirring on a vortex in Module 3, the loose aggregates would be dispersed into smaller nanoparticles that would then be coated separately by CE LP/CC LP to yield smaller LPP. Secondly, as the larger aggregates of MgP NP scattered more light than the smaller nanoprecipitates, they dominated the computation of the hydrodynamic diameter of the whole MgP NP population; as the small nanoprecipitates gained size after being coated with CE LP/CC LP, they scattered more light to dominate the DLS measurements, thereby displaying a smaller overall hydrodynamic diameter of the final LPP formulations.

Table 2.6. Hydrodynamic diameter (D), ζ-Potential and catalase activity of encapsulated and complexed LPP formulations and their components

Component	**Lipid composition**	**D (nm)**	**PDI**	**ζ-Potential (mV)**	**Catalase Activity %**
MgP NP	N/A	400 ± 67	0.22 ± 0.03	-10 ± 2	N/A
CE LP	DOTAP/Chol 1/1 mol/mol	233 ± 28	0.20 ± 0.05	53 ± 5	47 ± 15
CE LPP	DOTAP/Chol 1/1 mol/mol	284 ± 37	0.19 ± 0.05	40 ± 2	49 ± 21
LP	DOTAP/Chol 7/3 mol/mol	82 ± 14	0.12 ± 0.02	44 ± 1	N/A
CC LP	DOTAP/Chol 7/3 mol/mol	114 ± 16	0.24 ± 0.07	40 ± 4	118 ± 6
CC LPP	DOTAP/Chol 7/3 mol/mol	141 ± 15	0.27 ± 0.04	31 ± 2	132 ± 10

Data presented as mean ± SD (n=5).

CC LPP prepared using the complexation loading approach, successfully preserved over 100% activity after the preparation process, whereas, CE LPP retained less than 50% activity (Table 2.6).

2.5.4 Tracking of catalase payload through LPP preparation. Cyanine 7.5 labeled catalase was loaded into LPP formulations and the percentage of fluorescence intensity and catalase activity remaining in the LPP formulations (initial free catalase intensity/activity = 100%) were tracked through all the processing steps of LPP preparation. During the preparation of CE LPP (Fig. 2.11a), catalase activity was partially lost during the extrusion and concentration steps. Extrusion involved mechanical forces, and concentration involved centrifugal forces, both of which could have denatured the cargo protein catalase; the catalase protein could also be lost during the formulation process. However, there was no significant decrease in fluorescent intensity (λ_{ex} = 790 nm and λ_{em} = 810 nm) of the fluorescently labeled catalase during the preparation of CE LPP, which showed that loss of activity was mostly due to protein denaturation rather than physical loss of protein from the LPP formulation. In correlation with our previous observations, the preparation of CC LPP preserved the activity of the payload catalase through the entire preparation process (Fig. 2.11b). In both the CE LPP and CC LPP formulations, the input protein was equal to the final output after the concentration step, as marked by the retention of fluorescence signal from the protein. Therefore, the dose calculation for animal experiments in this study was based on the protein initially loaded (encapsulated/complexed) into the liposomes.

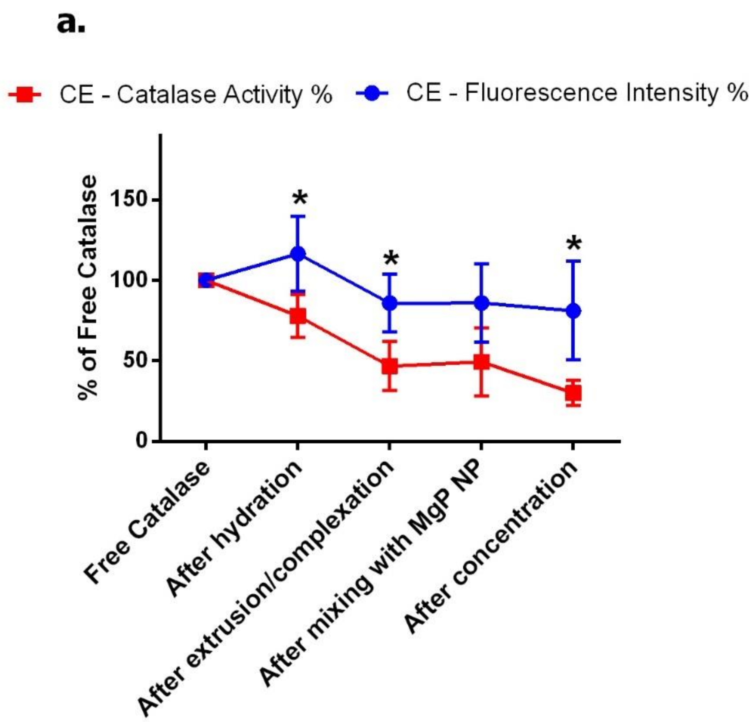

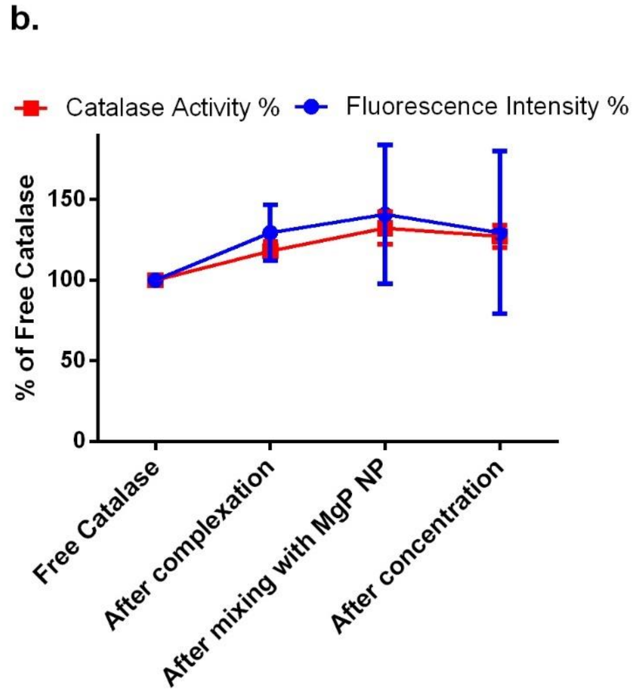

Fig. 2.11. Tracking catalase payload at different preparation stages of CE LPP (a) and CC LPP (b). Data presented as mean ± SD (n=3). * $p<0.05$.

2.5.5 Colloidal stability of LPP formulations. As shown in Table 2.7, the LPP formulations (CC LPP and CE LPP) and their precursors, namely cationic LP, CC LP and CE LP remained colloidally stable over a period of 2 months at 4 °C when each of them maintained similar hydrodynamic diameters, PDI and positive surface charges. A loss of 10-15% catalase activity was observed in all the formulations stored for a week at 4 °C, which increased to 20-25% over a month at 4 °C. After storage for a week or more at 4 °C, MgP NP showed substantially larger hydrodynamic diameter and PDI (Table 2.8), indicating its aggregation. Therefore, a new batch of MgP NP was always prepared, and complexed with the liposomes within a day or two. Similarly, new batches of LPP were always prepared and used for biological evaluations within a week.

Table 2.7. Hydrodynamic diameter (D), ζ-Potential and catalase activity of LPP formulations and their precursors stored at 4 °C

Component	**Storage Condition**	**D (nm)**	**PDI**	**ζ-Potential (mV)**	**CAT Activity %**
Cationic LP	Initial	62	0.14		N/A
	1 week at 4 °C	64	0.12	32	N/A
	Initial	95	0.09	44	N/A
	1 month at 4 °C	97	0.09	36	N/A
	2 months at 4 °C	96	0.08	39	N/A
CC LP	Initial	90	0.27		128
	1 week at 4 °C	84	0.25	38	114
	Initial	120	0.2	41	110
	1 month at 4 °C	120	0.18	39	86
	2 months at 4 °C	117	0.19	33	86
CC LPP	Initial	116	0.25	29	153
	1 week at 4 °C	112	0.32	26	120
	Initial	147	0.22	33	124
	1 month at 4 °C	142	0.25	32	93
	2 months at 4 °C	146	0.29	33	101
CE LP	Initial	200	0.19		35
	1 week at 4 °C	202	0.18	55	30
	Initial	228	0.17	46	75
	1 month at 4 °C	243	0.17	52	53
	2 months at 4 °C	234	0.21	54	58
CE LPP	Initial	229	0.2	39	36
	1 week at 4 °C	215	0.21	46	33
	Initial	274	0.17	39	80
	1 month at 4 °C	276	0.21	41	54
	2 months at 4 °C	262	0.12	43	63

Table 2.8. Hydrodynamic diameter (D), ζ-Potential and phosphate concentration of MgP NP stored at 4 °C

Component	Storage Condition	D (nm)	PDI	ζ-Potential (mV)	Phosphate Conc (mM)
MgP NP	Initial	342	0.23	-9	7.1
	1 day at 4 °C	609	0.43	-6	
	2 day at 4 °C	461	0.3	-5	
	4 day at 4 °C	503	0.3	-6	
	1 week at 4 °C	2076	0.45	-13	7.1
	Initial	394	0.18	-9	5.8
	1 month at 4 °C	1223	0.3	-12	4.6
	2 months at 4 °C	1154	0.45	-17	6.1

2.5.6 Isotonicity of LPP formulations

2.5.6.1 Influence of salt on complexation. As shown in table 2.9, CE LP and CC LP prepared in an isotonic buffer (5mM HEPES, 149 mM NaCl, pH 7.4) had larger hydrodynamic diameters and greater PDIs than those prepared in a low salt buffer (5mM HEPES, pH 7.4). To avoid this, liposomes were first prepared in low salt HEPES buffer followed by isotonicity adjustment at a later stage.

Table 2.9. Hydrodynamic diameter (D) and ζ-Potential of CE LP and CC LP prepared in buffers containing low salt and isotonic salt concentration

Component	Buffer Used	D (nm)	PDI	ζ-Potential (mV)
CE LP	Low salt buffer (5mM HEPES)	226	0.16	52
	Isotonic buffer (5mM HEPES, 149 mM NaCl)	323	0.36	69.5
CC LP	Low salt buffer (5mM HEPES)	119	0.23	41
	Isotonic buffer (5mM HEPES, 149 mM NaCl)	155	0.35	56

2.5.6.2 Isotonicity adjustment post-preparation. In order to adjust the isotonicity of the liposome suspension containing low salt (5mM HEPES), an aliquot of a concentrated salt or glucose solution was added. Addition of concentrated salt solution resulted in the aggregation of the liposomes as seen by the drastic increase in the hydrodynamic diameter (Table 2.10). In contrast, isotonicity adjustment by glucose solution maintained the colloidal properties of the liposomes.

Table 2.10. Hydrodynamic diameter (D) and ζ-Potential of LP and LPP formulations after isotonicity adjustment with concentrated salt and glucose solutions

Component	Condition	D (nm)	PDI	ζ-Potential (mV)
CE LP	Initial	226	0.16	52
	Isotonicity adjusted w/ salt	2845	0.12	
	Isotonicity adjusted w/ glucose	202	0.11	43
CE LPP	Initial	238	0.12	41
	Isotonicity adjusted w/ salt	2389	0.12	
	Isotonicity adjusted w/ glucose	203	0.14	48
CC LP	Initial	127	0.45	36
	Isotonicity adjusted w/ salt	4317	0.22	
	Isotonicity adjusted w/ glucose	114	0.35	36
CC LPP	Initial	137	0.4	30
	Isotonicity adjusted w/ salt	2445	0.55	
	Isotonicity adjusted w/ glucose	149	0.39	29

2.6 Discussion

Electrostatic interactions have driven the assembly of several nanocarriers of biomolecules, such as lipoplexes of cationic liposomes and DNA [85], polyplexes of cationic polymers and DNA, and stabilized plasmid-lipid particles containing cationic PEG lipids [86]. Furthermore, electrostatic interactions have also driven the multistep assembly of more complex nanocarrier systems such as LPD formulation of DNA [87], and LCP formulation of siRNA [88], both of which involve the coating of a condensed nanocore with lipid membranes carrying opposite charges. In this study, the construction of the LPP formulations for protein delivery (CE LPP and CC LPP) also exploited electrostatic interactions between its components. In the case of CE LP, the cargo protein catalase was loaded not only by passive encapsulation, but also by charge-facilitated encapsulation and adsorption onto the positively charged lipid. The loading of catalase in CC LP was mainly driven by electrostatic adsorption. Moreover, the excessive positive charges of the catalase-loaded liposomes (CE LP and CC LP) interacted with the negative surface charges of MgP NP to induce coating of MgP NP with the liposomes to yield the final LPP formulations (CE LPP and CC LPP) (Fig. 2.8). The lipid/protein molar ratio of 1.6×10^4 was intentionally chosen to ensure that the liposomes carried excessive positive charges to facilitate the sequential assembly of LPP driven by electrostatic forces [39]. The excessive positive charges from DOTAP were confirmed by highly positive ζ-potential of both the catalase-loaded liposomes (CE LP and CC LP) and their respective final LPP formulations (Table 2.6).

In module 1, compared to encapsulation (CE LP), the complexation strategy yielded catalase-complexed liposomes (CC LP) of significantly lower size and preserved all the protein activity (Table 2.6) by minimizing the mechanical stress exerted on the protein during extrusion. Although both microfluidic mixing and extrusion with a LIPEX extruder yielded small cationic liposomes of 70 nm in diameter, LIPEX extruder was chosen for preparing cationic liposomes for this study, due to the accessibility of the equipment and the ease of use and scale-up for animal studies.

The overall colloidal stability of the LPP formulations depended on the electrostatic repulsions from the excess positive charges of the cationic lipids [58]. As a result, the liposomal formulations remained physically stable when stored for up to 2 months in a refrigerator. Although MgP NP precipitated after being stored for a week at 4 °C, no MgP NP precipitate was observed in the final LPP formulations, indicating that the coating by the cationic liposomes stabilized MgP NP.

The formation of larger liposomes and liposome-protein complexes in isotonic HEPES containing NaCl suggests the interference of salt in the complexation process. Salts are known to produce charge shielding/electrical double layer due to their ionic properties [89], which may have resulted in the formation of loose liposome-protein complexes or larger liposome-salt-protein complexes. Preparation of liposomes in a low salt buffer followed by subsequent addition of a hypertonic NaCl solution to adjust isotonicity resulted in liposome disruption and precipitation. Because glucose preserved the colloidal properties of the liposomes, it was used for isotonicity adjustment in the LPP formulations of catalase for animal studies.

Overall, isotonic LPP formulations of catalase were successfully prepared and characterized for *in vivo* application. CE LPP carried an average diameter around 284 nm whereas CC LPP had a reduced diameter of 141 nm as a result of the complexation technique. The complexation technique (CC LPP) also helped in preserving the activity of the catalase payload.

Chapter 3: Morphological Studies of Lipid-coated Magnesium Phosphate Nanoparticles Using Transmission Electron Microscopy

3.1 Introduction

3.1.1 Principle of transmission electron microscopy. Transmission electron microscopy (TEM) is a microscopy technique that uses electrons transmitted through a sample to obtain invaluable information on the sample's inner structure [90]. An ultrathin section of the specimen or a suspension of the sample on a grid is subjected to an accelerated beam of electrons. The transmitted electrons form an image, which is then magnified and focused to obtain a 2D image of the sample. Electrons are scattered by metals present in the sample. If the sample contains heavy metals, the sample structures would appear darker and would have greater contrast against the background. However, samples composed of non-metals such as C, H and O do not scatter electrons much and cannot be distinguished from the background on a TEM image. In order to visualize such samples, additional staining techniques are needed [91]. Positive staining of the specimen helps to visualize its inner components, for example, organelles inside a cell. Conversely, negative staining of the specimen's background helps to visualize its size and structure [92].

3.1.2 Negative staining techniques in TEM. Negative staining is a quick and easy qualitative technique for visualizing samples in TEM. Heavy metal stains such as phosphotungstic acid (PTA), uranyl acetate (UA) and uranyl formate (UF) are commonly used for negative staining [91]. Ideally, the negative stain does not interact with the sample structures but stains the background to create a contrast that allows us to visualize the sample. However, negative staining can result in structural artifacts caused by sample-stain interactions such as flattening of spherical or cylindrical structures, or formation of myelin figures and staining artifacts due to uneven distribution of the stain [93]. Nevertheless, negative staining is a very useful technique because it is easy, rapid and cost-effective because it does not require any additional specialized equipment other than what is already available in an EM laboratory.

3.1.3 Applications of TEM in nanotechnology. TEM is used to obtain morphological, topographical, compositional and crystalline information of samples and is applicable to numerous disciplines such as life sciences, nanotechnology, material research, forensic analysis, gemology and metallurgy. In nanotechnology, TEM serves as a very important tool for characterizing the particle size and morphology of nanocarriers [94].

3.1.3.1 Characterization of LPP with TEM. The aim of research reported in this chapter was to use TEM to examine the morphology and the particle size distribution of different components of LPP, namely, magnesium phosphate nanoparticles (MgP NP), catalase-encapsulated liposomes (CE LP), catalase-complexed liposomes (CC LP), catalase-encapsulated lipid-coated phosphate nanoparticles (CE LPP) and catalase-complexed lipid-coated phosphate nanoparticles (CC LPP). In addition, TEM was also used to examine changes in the morphology of LPP in response to acidic pH.

3.2 Materials and Methods

3.2.1 Materials. Two-hundred mesh continuous carbon-coated copper grids were obtained from TED PELLA (Redding, CA). Phosphotungstic acid was purchased from Fisher Scientific (Hampton, NH).

3.2.2 Sample preparation for characterization with TEM. The morphology of LPP and its formulation precursors was studied on a JEOL-JEM 1230 Electron Microscope (JEOL, Japan). Two-hundred mesh carbon-coated copper TEM grids were exposed to glow discharge before use to increase their hydrophilicity. MgP NP sample (5 µL) was dripped onto the grid, air-dried for about 30 minutes and blotted with a filter paper to generate a thin film. Liposomal samples (5 µL) were deposited on the grid, air-dried for a minute and blotted using a filter paper to generate a thin film on the grid. Samples containing cationic lipids were negatively stained with PTA (5 cycles of quick staining with 5 µL 2% PTA and blotting). The grids were then transferred into the electron microscope for imaging at an accelerating voltage of 100 KV, with the help of Dr. Fei Guo at the Electron Imaging Facility, Department of Molecular and Cellular Biology, UC Davis. Digital images were recorded and analyzed with EMMENU4 (TIETZ imaging software).

3.2.2.1 Sample preparation for characterizing LPP after exposure to acidic pH. In order to characterize the morphological changes in response to acidic pH, LPP formulations (both CE LPP and CC LPP) were incubated in pH 5.5 acetate buffer for 30 minutes prior to TEM sample preparation and imaging as described above (3.2.2).

3.3 Results

3.3.1 Morphology of LPP and its components at pH 7.4. The morphology of CE LPP, CC LPP and their formulation precursors were studied by TEM.

3.3.1.1 Morphology of MgP NP. As shown in Fig. 3.1, MgP NP suspension contained both small (about 50–100 nm in diameter) nanoparticles (Fig. 3.1a, b) and larger aggregates above 1000 nm in diameter (Fig. 3.1c). This would explain the larger hydrodynamic diameter of MgP NP than the final LPP formulations seen in Table 2.6. Electrostatic repulsion induced by adding sodium citrate kept some nanoparticles separate. However, a substantial portion of the smaller nanoparticles still stuck together to form larger aggregates (Fig. 3.1d).

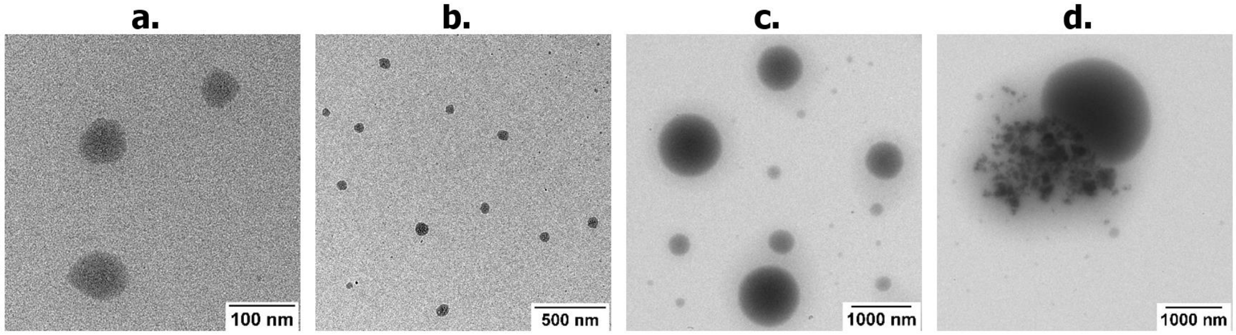

Fig. 3.1. TEM images of MgP NP nanoparticles (a-d)

3.3.1.2 Morphology of CE LP and CC LP. CE LP appeared as bright spherical structures with a dark background due to the negative staining by PTA (Fig. 3.2a, b). Smaller white dots around a few nanometers in diameter were observed inside, on the surface and around the liposomes. These dots most probably represented the catalase molecules that were encapsulated inside the liposomes, adsorbed onto the liposome surface, or free in solution around the vesicles. Unloaded cationic liposomes (Fig. 3.2c) appeared as much smaller structures compared to CE LP (Fig. 3.2a, b). A lot of white dots were observed around the vesicles in CC LP samples (Fig. 3.2d), which were most likely the protein complexed to the cationic liposomes.

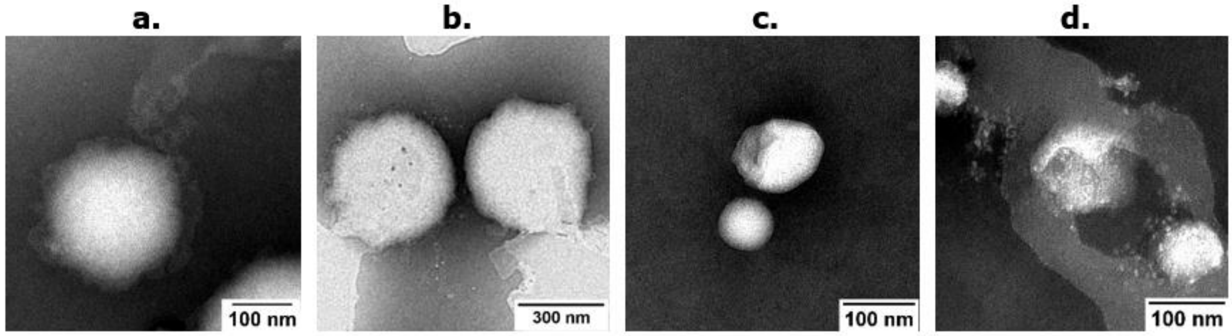

Fig. 3.2. TEM images of CE LP (a, b), cationic LP (c) and CC LP (d)

3.3.1.3 Morphology of CE LPP and CC LPP. A darker center was observed inside the liposomal vesicles in both CE LPP (Fig. 3.3a, b) and CC LPP (Fig. 3.3c, d), which was not seen in CE LP (Fig 3.2a, b) or CC LP (Fig. 3.2d). This suggests that the darker center represents a MgP NP core in both the LPP formulations.

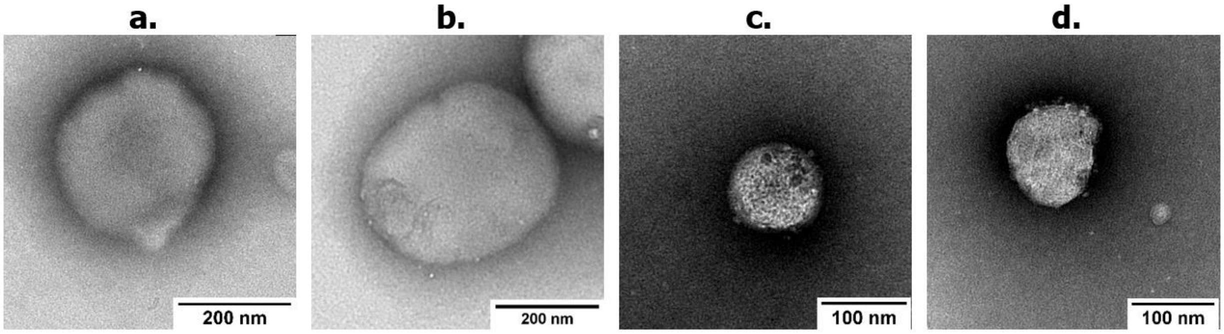

Fig. 3.3. TEM images of CE LPP (a, b) and CC LPP (c, d)

3.3.2 Morphological changes in LPP in response to acidic pH. TEM images of CE LPP and CC LPP formulations showed tight, spherical structures at pH 7.4 (Fig. 3.3a-d) but deformed and scattered structures upon incubation at pH 5.5 for 30 minutes (Fig. 3.4a-d).

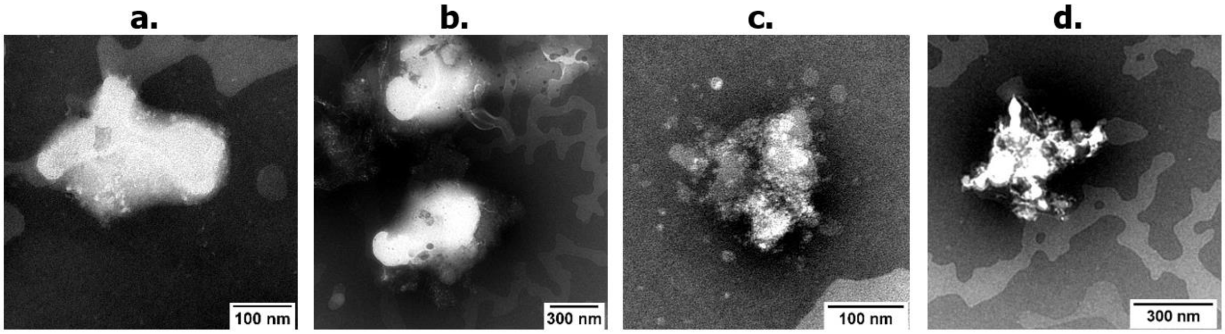

Fig. 3.4. TEM images of CE LPP (a, b) and CC LPP (c, d) in response to acidic pH

3.3.3 Comparison of diameters obtained from TEM with DLS. The diameters of the structures seen in the TEM images were measured using ImageJ software. For the liposomal components of LPP, around 10-15 structures were measured, and their average diameter was calculated. Due to the wide size distribution of MgP NP, 50-60 structures were randomly measured, and their average was calculated. The diameters measured from TEM images were consistent with dynamic light scattering (DLS) measurements. The TEM diameter of MgP NP had a large standard deviation as the structures ranged from small precipitates measuring 20 nm in diameter to large aggregates measuring 1.9 μm.

Table 3.1. Diameters of LPP and its precursors measured using TEM and DLS

Component	**TEM diameter (nm)**	**DLS diameter (nm)**
MgP NP	320 ± 460	400 ± 67
CE LP	270 ± 110	233 ± 28
CE LPP	230 ± 90	284 ± 37
Cationic LP	80 ± 20	82 ± 14
CC LP	100 ± 30	114 ± 16
CC LPP	100 ± 40	141 ± 15

Data represented as mean ± SD, n=5 for DLS measurements.

3.4 Discussion

The TEM images of LPP and the formulation precursors were consistent with the Dynamic Light Scattering measurements and confirmed the location of the protein and the presence of a MgP NP core in the final LPP formulations. Both TEM and DLS showed that the strategy of complexing cationic LP with catalase yielded smaller CC LP when compared with the encapsulation technique (CE LP).

The bursting of LPP formulations in response to acidic pH is evident and can be visualized more clearly in this study compared to our previous report (Chapter 1, Fig. 1.3). The deformation of LPP formulations is consistent with our previous studies [39, 80]. Taken together, these observations strongly support the proposed mechanism of pH-triggered release of catalase, where the MgP NP core dissolves at acidic pH into a solution of high osmotic pressure, which consequently swells, deforms, and in many cases lyses the LPP formulation.

In addition to morphological characterization, TEM could be used in combination with confocal microscopy to monitor the cellular uptake and endosomal escape of LPP inside the cell [95, 96].

Chapter 4: Evaluation of Protein Delivery by LPP in Healthy Mouse Lung

4.1 Introduction

4.1.1 *In vivo* evaluation of LPP in healthy mice. The aim of studies reported in this chapter is to evaluate the efficiency of protein delivery by LPP in healthy lungs and to determine the optimal route of administration to facilitate intrapulmonary delivery of LPP. In order to do so, intranasal (IN) administration and intravenous (IV) administration were both attempted and were compared in healthy animals.

Catalase, the cargo protein in this study, is an endogenous antioxidant enzyme in normal lungs, and contributes to the lung's antioxidant defense system [45]. Lung inflammation is often associated with oxidative stress of pulmonary cells [42-44], which can be alleviated by catalase. Thus, the lung was chosen as the target organ for the catalase formulations in order to explore their potential applications in pulmonary diseases that are associated with inflammation [97, 98].

4.1.2 Route of administration

4.1.2.1 Intravenous dosing. Cationic liposomes have been reported to rapidly accumulate in the lung tissue following intravenous administration [50, 51, 99]. To exploit this phenomenon in our study, catalase formulations were administered intravenously by tail-vein injection in healthy animals. The maximum dose volume that can be administered intravenously (IV bolus, duration <1 minute) in mice is 5 mL/Kg, so ~100 μL was given to each animal [100]. Tail-vein injection demands considerable hands-on skills and needs a lot of practice. There is a high chance of missing the vein and injecting the solution into the surrounding tissue.

4.1.2.2 Intranasal dosing. Intranasal route of administration is commonly used for intrapulmonary delivery of liquids and aerosols [97, 101]. In our study, catalase formulations were dosed intranasally by dripping small droplets of liposomal suspension onto the nostrils of healthy animals. The ideal volume for intranasal dosing targeted to the lung is 25-50 µL whereas volumes <20 µL are used for brain delivery [102, 103]. The intranasal route is easy to administer, non-invasive and directly delivers the dose to the lung, thus tissue avoiding stability and clearance issues related to administration into the systemic blood circulation. However, intranasal dosing provides no control over the percentage of dose successfully delivered into the lungs because the dose may be swallowed by the animal to enter the gastrointestinal tract instead.

Alternatively, the oropharyngeal route of administration has also been studied for direct lung delivery [104]. It is another non-invasive technique where the animal's tongue is pulled out, and the dose volume is pipetted onto the distal part of the oropharynx while simultaneously closing the nostrils. This route was not explored in this dissertation because the gentle occlusion of the tiny nostrils in mice is difficult, yet crucial for the success of this route of administration.

4.2 Materials and Methods

4.2.1 Materials. Pierce protease inhibitor cocktail and T-PER protein extraction reagents were purchased from Fisher Scientific (Hampton, NH). Carboxy-H_2DCFDA was purchased from Molecular Probes (Eugene, OR). Bovine liver catalase (E3289) was purchased from Sigma-Aldrich (St. Louis, MO). Cyanine 7.5 labeled bovine liver catalase was purchased from Nanocs Inc (New York, NY). Isoflurane, ketamine, xylazine, and acepromazine were purchased from Patterson Veterinary (Greeley, CO).

4.2.2 Experimental animals. CD-1 female mice (7 weeks old) were purchased from Charles River Laboratories (Wilmington, MA). All work performed on animals was in accordance with and approved by the University of the Pacific Institutional Animal Care and Use Committee (Protocol# 15R12).

4.2.3 Preparation of LPP for *in vivo* administration. CE LPP and CC LPP formulations were prepared as per the three modules described in Chapter 2 (2.2.2) and carried 5.9 mM total lipid and 0.37 µM catalase each. Liposomal formulation of catalase (L-CAT) was prepared as described previously (Chapter 2, 2.2.2.1.1) and carried 9.8 mM total lipid and 0.61 µM catalase. CC LPP, CE LPP and L-CAT were concentrated using an Amicon® Ultra-4 mL centrifugal filter (MWCO 10K) to obtain the catalase concentration required for intranasal and intravenous dosing. Briefly, 4 mL of formulations were added to the Amicon filter tubes and centrifuged at 4000g, 4 °C on a Beckman GS-6R centrifuge (Beckman Coulter Inc., Brea, CA) for 1-2 hours to concentrate the suspensions to 1 mL. The concentrated samples were recovered from the filter and an aliquot of concentrated glucose solution (2 M) was added to adjust the isotonicity. The recovered formulations were then diluted appropriately with isotonic HEPES buffer (5mM, pH 7.4 with 5% w/v glucose) to attain the following concentrations: 6.4 mM total lipid and 0.4 µM catalase for intravenous administration and 21.3 mM total lipid and 1.3 µM catalase for intranasal administration.

For fluorescent imaging studies, the formulations (f-CC LPP, f-CE LPP and L-f-CAT) were prepared as described above using catalase that were labeled with Cyanine 7.5 fluorescent probe (Nanocs Inc, NY). Care was taken to protect the fluorescently labeled catalase from light during preparation.

4.2.4 Administration of LPP in healthy mice. CD-1 female mice (~8 weeks old at the time of dosing) were randomly divided into ten groups (n=6): CC LPP/intravenous, CE LPP/intravenous, L-CAT/intravenous, free CAT/intravenous, control group/intravenous, CC LPP/intranasal, CE LPP/intranasal, L-CAT/intranasal, free CAT/intranasal and control group/intranasal.

4.2.4.1 Intravenous dosing. Before intravenous dosing, each animal was lightly anesthetized with 1-3% isoflurane vaporized with 1 mL/min O_2. The animal was then moved into a plastic rodent restrainer for tail vein injection of the respective treatment (0.3 mg/Kg catalase in ~100 µL dose volume) using a 1 mL disposable sterilized syringe with a 30 G needle. The tail was cleaned with 70% IPA and immersed in warm water to enhance the visibility of the veins. Untreated animals were used as a control.

4.2.4.2 Intranasal dosing. Animals were anesthetized with 1-3% isoflurane vaporized with 1 mL/min O_2 before dosing. While the animal was waking up from anesthesia, marked by the start of limb movements and deep abdominal breath, the respective treatment (0.3 mg/Kg catalase in ~36 µL dose volume) was administered intranasally. The control group received an equivalent volume of PBS. The mouse was restrained and held at a 45-90° angle and the treatment solution was dripped onto its nostrils using a 20 µL Eppendorf pipette. Care was taken to ensure slow and gradual dosing to avoid drowning, choking or expulsion of the liquid by animal's sneezing. The dose volume was evenly distributed across both nostrils (~18 µL per nostril). After completion of dosing, the animal was awake, returned to its cage and monitored for any signs of distress.

4.2.5 Fluorescence imaging of LPP distribution in healthy mice. In a separate study, catalase that was fluorescently labeled with Cyanine 7.5 (λ_{ex} = 790 nm, λ_{em} = 810 nm) was used to study the distribution of different catalase formulations in mice [105]. Animals were randomly divided into eight groups (n=3 each): f-CC LPP/intranasal, f-CE LPP/intranasal, L-f-CAT/intranasal, free f-CAT/intranasal, f-CC LPP/intravenous, f-CE LPP/intravenous, L-f-CAT/intravenous and free f-CAT/intravenous. All mice were dosed at 0.3 mg/Kg fluorescently labeled catalase and were then subjected to *in vivo* imaging to detect the distribution of the cyanine fluorescence.

Mice were anesthetized with isoflurane (2-3% for induction and 1-2% for maintenance) before being placed in the MousePOD® and imaged with a Li-Cor Odyssey® Fluorescence Imaging System (LI-COR Biosciences, Lincoln, NE) (Instrument settings: Resolution: 337 µm, Focus: 2.0 mm, Channel intensities: 700 nm – L2 and 800nm – 3) at select time points (0.5, 1, 2, 4, 8, 12, 24 and 48 hours) up to 48 hours post administration while remaining sedated. The mice regained consciousness within few minutes after the imaging. Image Studio Lite (LI-COR Biosciences) was used for processing and analyzing the images. All the images were normalized by fixing the intensity scale to the same minimum and maximum value. Signal intensity (SI) was obtained from regions of interest such as head, lungs and abdominal region by drawing box shapes around those regions in each mouse. Mean signal intensity (MSI) was calculated by dividing the SI with the area of the box. Normalized intensity percent was calculated by:

$$\text{Normalized intensity } \% = \frac{\text{MSI}_{\text{region of interest}}}{\text{MSI}_{\text{background}}} * 100$$

Where $\text{MSI}_{\text{region of interest}}$ corresponds to the MSI obtained from a specific region (for example, lung of mice treated with CC LPP at 0.5 hour) and $\text{MSI}_{\text{background}}$ corresponds to the MSI obtained for the same region from an untreated mouse (background intensity) [106].

4.2.6 Tissue collection and analysis. Four hours post-dosing, the animals dosed with bovine liver catalase (4.2.4) were anesthetized by intraperitoneal injection of an anesthetic cocktail (65 mg/kg ketamine, 12 mg/kg xylazine and 2 mg/kg acepromazine). The lung tissue was flushed with ice-cold PBS and transferred into tubes containing T-PER lysis buffer with protease inhibitors. Zirconium beads were added to the tubes for homogenization on a Mini Bead-Beater 1 (BioSpec Products, Bartlesville, OK) followed by centrifugation at 14000 g for 15 minutes at 4 °C on a Micromax RF microcentrifuge (Thermo Fisher Scientific, Waltham, MA). The resultant supernatants were analyzed immediately.

4.2.6.1 Measurement of catalase activity. The activity of the catalase delivered to the lungs was measured using both the H_2O_2 decomposition assay and the

Catalase Assay Kit (Cayman Chemical, Ann Arbor, MI). For H_2O_2 decomposition assay, H_2O_2 (25 mM, 1.2 mL) was transferred into a 1.5 mL quartz cuvette placed in a Beckman DU 640 Spectrophotometer (Beckman Coulter Inc, Brea, CA). At time zero, the reaction was initiated by transferring 0.2 mL tissue supernatant (diluted 20-fold with lysis buffer) into the cuvette. The cuvette housing unit was quickly closed and the UV absorbance of H_2O_2 at 240 nm was immediately recorded every 2 seconds for 1 minute. Lysis buffer (0.2 mL) was used as blank. The tissue samples were diluted by 20-fold so that the H_2O_2 decomposition in the first 60 seconds exhibited linear pseudo-zero order kinetics without generating substantial oxygen bubbles that would interfere with the UV absorbance.

Catalase activity was also measured using the catalase assay kit per the manufacturer's instructions. Tissue supernatants were diluted 100-fold with lysis buffer to fit into the linear range of the assay. The absorbance of the samples was measured at 540 nm using an Epoch Microplate Spectrophotometer (BioTek Instruments Inc, Winooski, VT).

4.2.6.1.1 Establishing a correlation between H2O2 decomposition assay and catalase activity kit. Catalase activity was initially analyzed in the tissue supernatants using the H_2O_2 decomposition assay. The catalase assay kit (Cayman Chemical, Ann Arbor, MI) was used later in the dissertation research because it offered higher sensitivity. Developing a correlation between both the assays was important to allow comparisons between all the data sets. Catalase standards (0.01 nM – 25 nM) were prepared and their activity was analyzed using both the assays. The output of both the assays were correlated and linear regression was performed with EXCEL to obtain an equation that would allow us to convert the H_2O_2 decomposition rates (AU/sec) into catalase activity (U/mL) for each sample.

4.2.6.2 Measurement of ROS levels. The ROS levels in the lung tissue supernatants were measured using the fluorescent probe Carboxy H_2DCFDA [107]. Briefly, 10 µL of 50 µM Carboxy H_2DCFDA was added to 100 µL of tissue supernatant that had been diluted 10-fold with lysis buffer in a 96-well plate, which was then incubated for an hour at 37 °C. The fluorescence (λ_{ex} = 485 nm, λ_{em} = 528 nm) was measured on a BioTek Synergy HT microplate reader (BioTek Instruments Inc, Winooski, VT).

4.2.6.3 Measurement of total protein. The total protein in the lung tissue supernatants was measured using the Pierce BCA protein assay (Thermo Fisher Scientific, Waltham, MA) per the manufacturer's instructions. Tissue supernatants were diluted 10-fold to fit into the linear range of the assay. The absorbance of the samples was measured at 540 nm using a TriStar LB 941 Multimode Microplate Reader (Berthold Technologies, Bad Wildbad, Germany).

4.2.7 Statistical analysis. Values that had both biological (multiple mice) and analytical (multiple measurements) replicates are expressed as mean ± SEM. One-way ANOVA paired with Tukey's posthoc analysis was performed using GraphPad Prism (GraphPad Software). Statistical significance was acknowledged at $p < 0.05$.

4.3 Results

4.3.1 Biodistribution of LPP in healthy mice. In this study, both intranasal and intravenous administration were attempted to deliver the catalase formulations into the lung. The distribution of fluorescently labeled catalase was monitored up to 48 hours following intranasal and intravenous administration of Cy7.5-labeled catalase formulations in CD-1 female mice.

4.3.1.1 LPP distribution after intranasal delivery. The fluorescent images (Fig. 4.1) obtained after intranasal dosing showed substantially higher lung distribution of f-CC LPP compared to f-CE LPP, L-f-CAT and free f-CAT groups (Fig. 4.2b). Free f-CAT distributed mainly into the lung during the first few hours but showed redistribution into the metabolic region between 4-8 hours post dosing (Fig. 4.1). The redistribution was significantly higher than other groups (Fig. 4.2c). In comparison, the Cy7.5-labeled catalase formulated in f-CC LPP was retained in the lung for up to 8 hours without much signal in the metabolic region, indicating the advantage of the complexed LPP formulation in delivering catalase into the lung. However, the fluorescence signal of f-CE LPP in the lung following IN administration was significantly lower, indicating much poorer lung distribution than f-CC LPP. f-CC LPP's higher intrapulmonary distribution could be attributed to its small particle size (~140 nm) and positive surface charges (+30 mV), whereas the much large size of f-CE LPP, which is about double that of f-CC LPP, may have hindered its inhalation and distribution into the lung [54]. The L-f-CAT formulation loaded with Cy7.5-labeled catalase had the lowest lung distribution. The fluorescence signal of Cy7.5-labeled catalase observed in the head region was probably because the formulations were mostly limited in the animal's nasal cavity and were then spread around the head and paws due to the animal's grooming habits. Interestingly, the fluorescence of the larger f-CE LPP and L-f-CAT in the head region was still lower than that of f-CC LPP, suggesting that the animal's grooming may have caused partial loss of f-CE LPP and L-f-CAT (Fig. 4.2a).

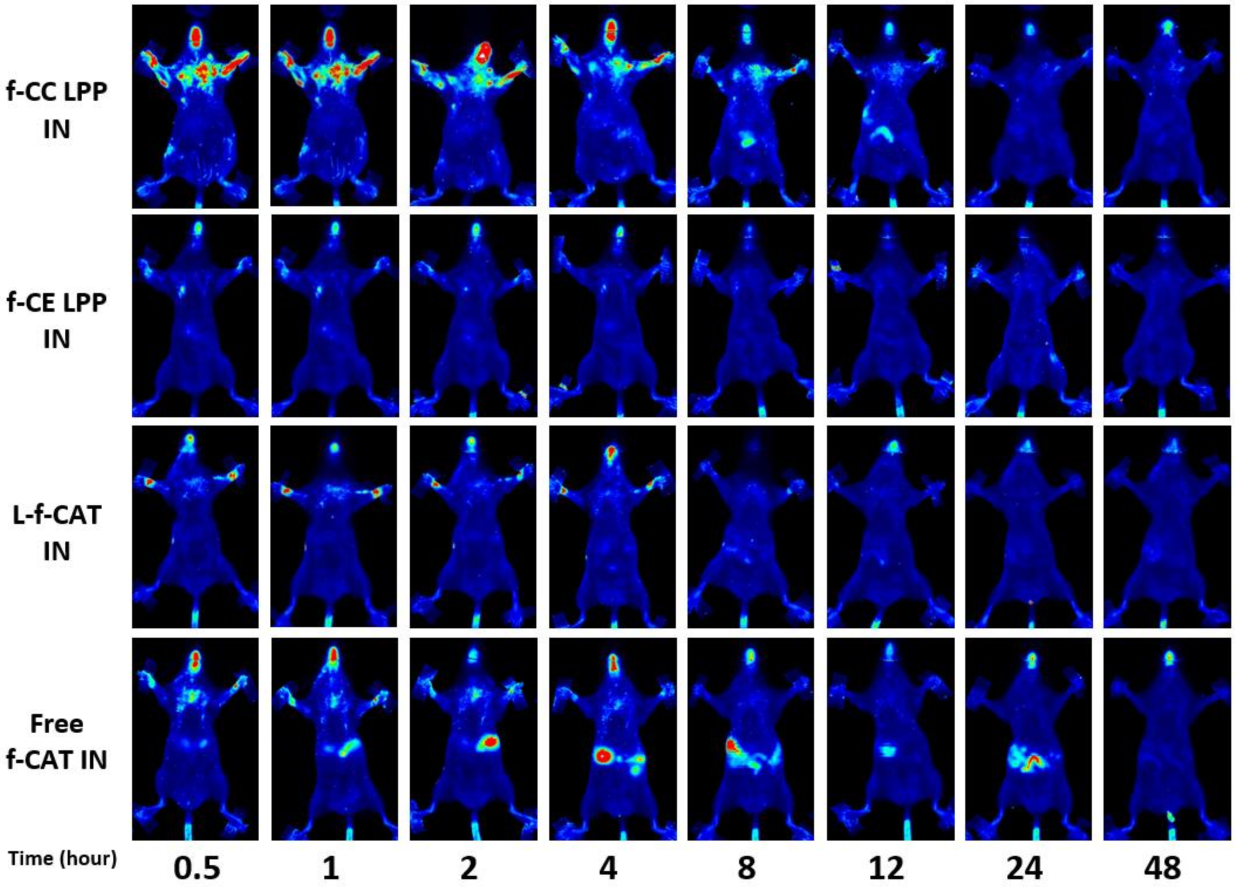

Fig. 4.1. Biodistribution of different Cy7.5-labeled catalase formulations after intranasal (IN) administration in CD-1 mice

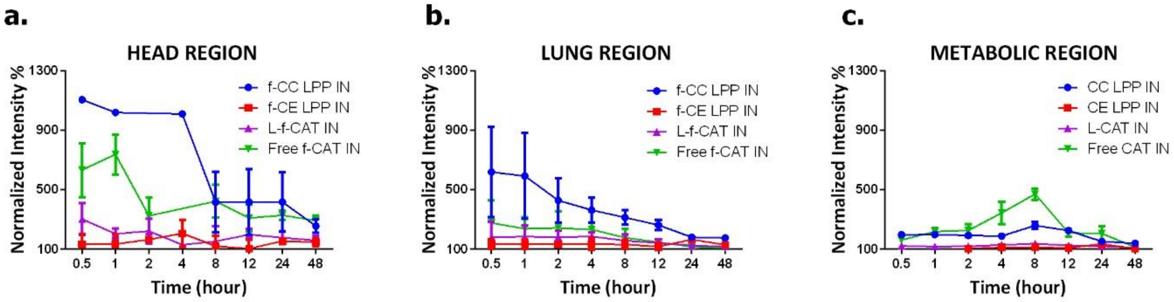

Fig. 4.2. Normalized fluorescence intensity of Cy7.5-labeled catalase in the head (a), lung (b) and metabolic (c) regions of CD-1 mice. Data presented as mean ± SD (n=3).

4.3.1.2 LPP distribution after intravenous delivery. Imaging of fluorescently labeled catalase showed that the same formulations as discussed in the last section distribution into the liver instead of the lungs after intravenous administration. Intravenous injection through the tail vein was successful only in some (1 out of 3 replicates in each group) of the mice and the successful images are shown in Fig. 4.3. The other animals in each group were partially successful because the fluorescence imaging showed that most of the Cy7.5-labeled catalase was stuck in the tail while some signal corresponding to the injected portion was observed in the liver region (data not shown).

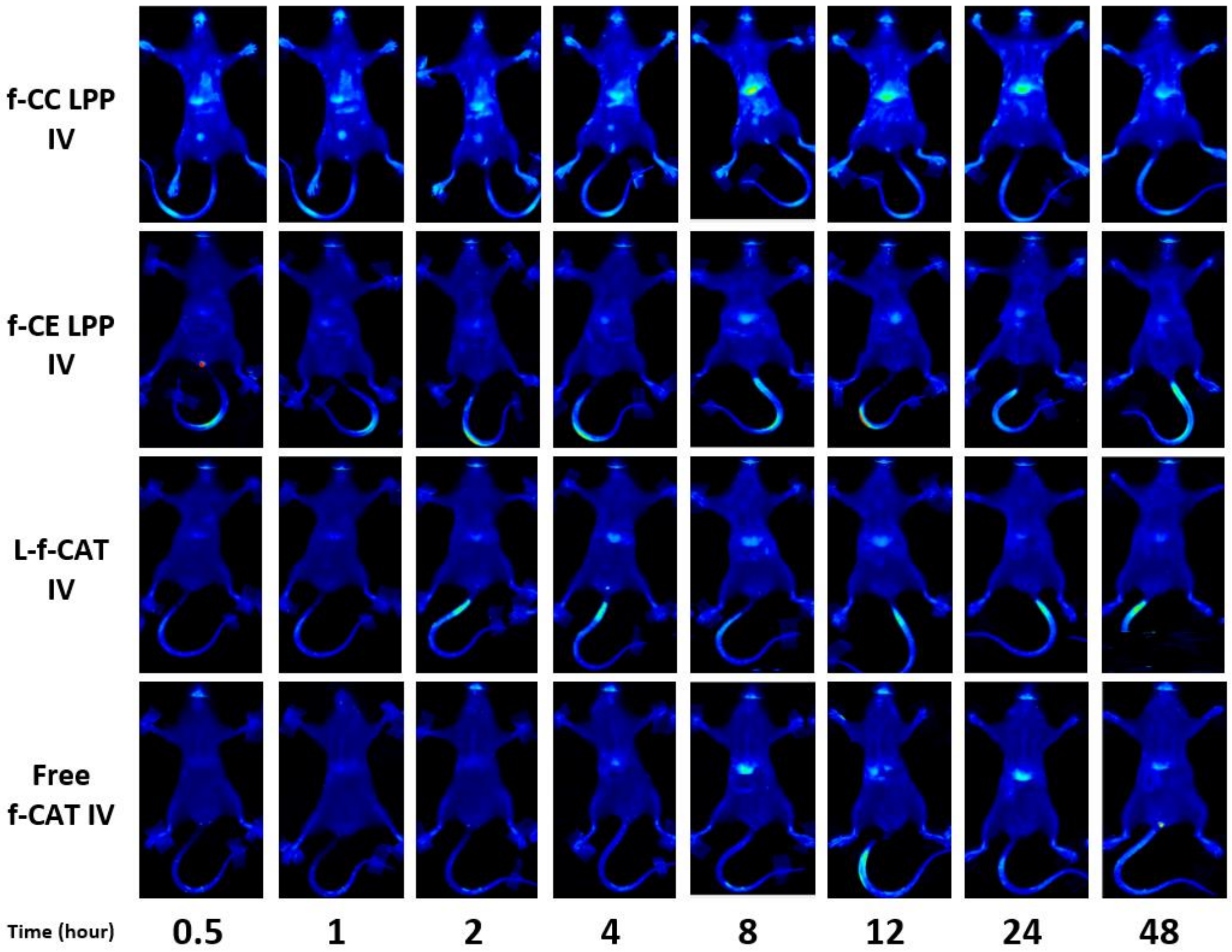

Fig. 4.3. Biodistribution of different Cy7.5-labeled catalase formulations after intravenous (IV) administration in CD-1 mice

4.3.2 Activity of LPP in healthy mouse lung. The functionality of the intrapulmonarily delivered catalase in the LPP formulations was assessed using two markers: 1) the increase of catalase activity in the lungs after the administration, and 2) the decrease of ROS level as a measure of whether the delivered cargo catalase can protect the lung tissue from oxidative stress.

4.3.2.1 LPP activity after intranasal delivery. Following intranasal administration, the complexed catalase formulation (CC LPP), which was smaller and which better preserved catalase activity than CE LPP, showed both better distribution and higher catalase activity in the lung compared to the encapsulated formulation (CE LPP). Both the LPP formulations yielded higher pulmonary catalase activity than the free catalase solution and were able to restore the catalase activity to that of the PBS-treated control group 4 hours after IN dosing (Fig. 4.4a). Both the CC LPP and CE LPP groups were able to significantly reduce the ROS levels in the lung tissue compared to the free catalase and the L-CAT group (Fig. 4.4c). The L-CAT group lacked the MgP NP core, suggesting the importance of the MgP NP core in facilitating protein delivery into the lung. In addition, administration of L-CAT increased the lung ROS levels compared to the PBS-treated control group, probably due to cationic lipid toxicity [108].

Overall, the ROS levels corresponding to different catalase groups correlated inversely with the respective catalase activities in the lung tissue. CC LPP produced higher catalase activity that corresponded to lower ROS levels compared to the CE LPP, L-CAT and free catalase groups. Compared to PBS-treated control, both free catalase solution and L-CAT elevated the ROS levels and lowered the catalase activity in the lung tissue 4 hours after intranasal administration. The lower catalase activity levels could result from the depletion of the endogenous catalase in combating the increased ROS after L-CAT and free catalase solution administration.

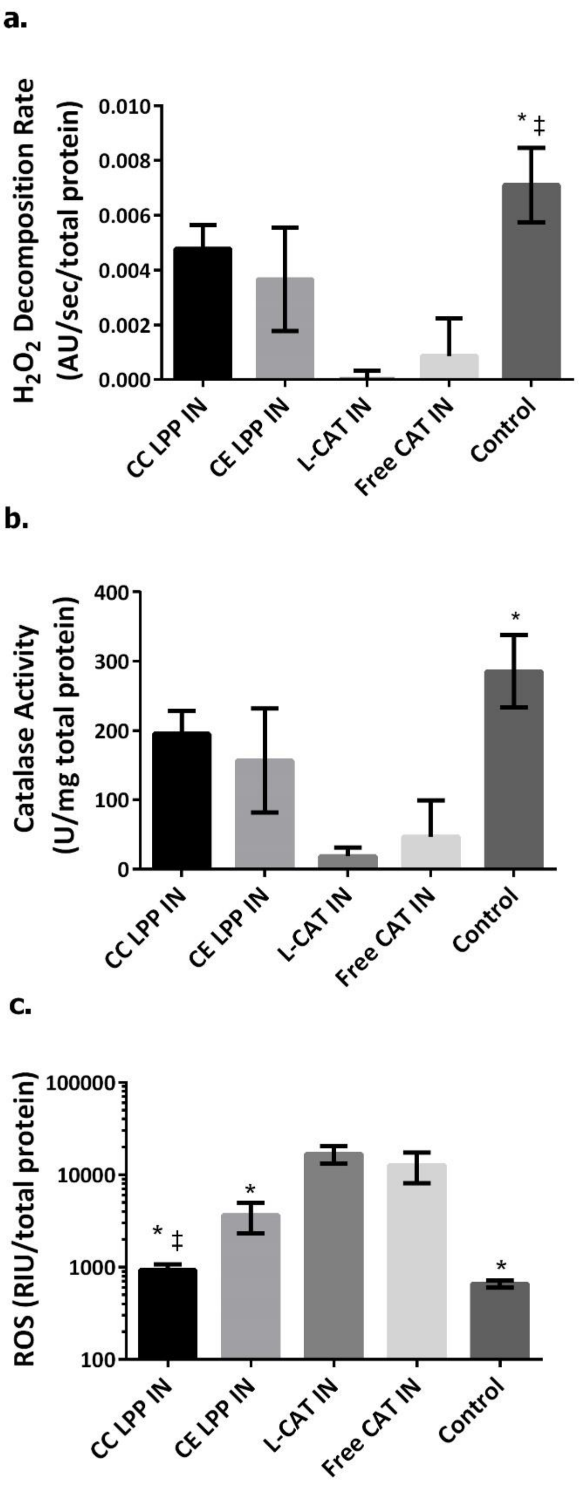

Fig. 4.4. H_2O_2 decomposition rate (a), calculated catalase activity (b) and ROS levels (c) in mouse lung supernatants after intranasal (IN) dosing of different catalase formulations. Data presented as mean ± SEM (n=6). $*p \leq 0.05$ versus L-CAT; $‡ \leq 0.05$ versus free CAT

4.3.2.2 LPP activity after intravenous delivery. Intravenous dosing of CC LPP, CE LPP, L-CAT and free catalase groups caused no substantial changes in the catalase activities (Fig. 4.5a) nor in the ROS levels (Fig. 4.5c) in the lung compared to untreated baseline levels. Fluorescence imaging of the biodistribution of Cy7.5-labeled catalase indicated that the formulations do not distribute substantially into the lung following intravenous dosing. Based on these results, intranasal administration but not intravenous administration was selected for further studies on the intrapulmonary delivery of LPP.

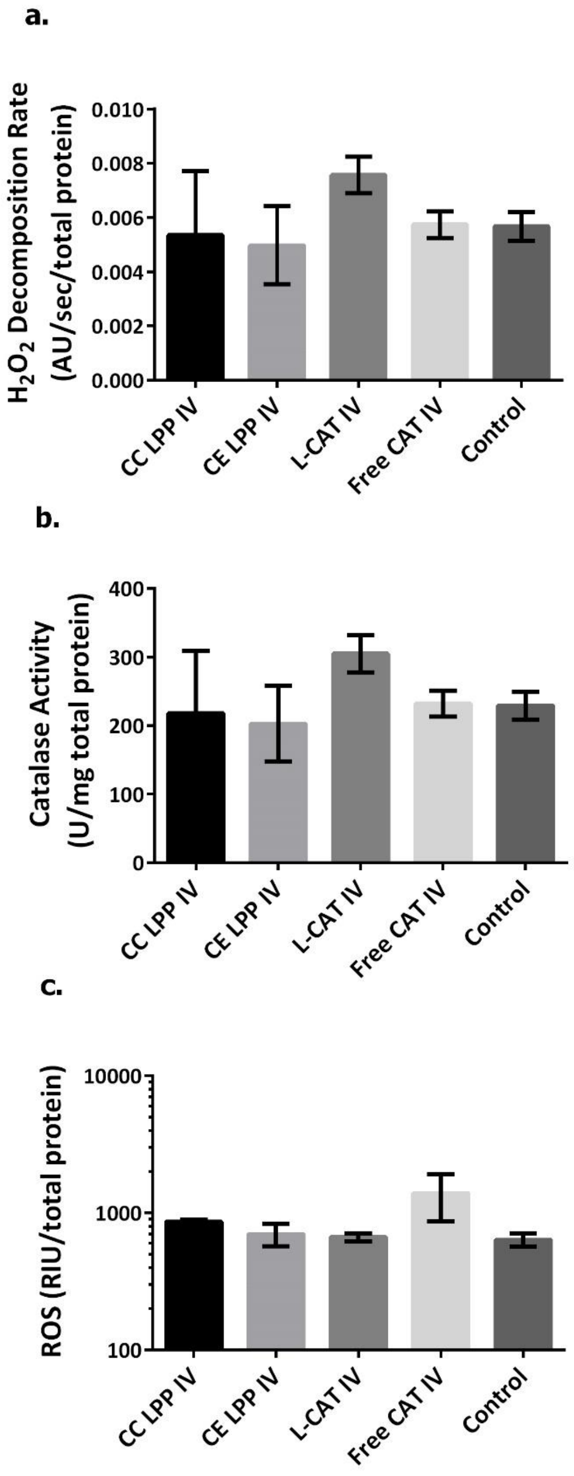

Fig. 4.5. H_2O_2 decomposition rate (a), calculated catalase activity (b) and ROS levels (c) in mouse lung supernatants after intravenous (IV) dosing of different catalase formulations. Data presented as mean ± SEM (n=6).

4.3.2.3 Statistical correlation between H2O2 decomposition assay and catalase activity kit. In order to correlate the catalase activities acquired by two different absorbance assays, two catalase standard curves were prepared: one showing the relationship between H_2O_2 decomposition rate (AU/sec) and catalase concentration (Fig. 4.6a), and the other showing the relationship between the enzyme activity of catalase (U/mL) and catalase concentration (Fig. 4.6b). The output activity obtained from both the assays had a correlation coefficient (r) of 0.9 (Fig 4.7), indicating strong positive correlation between them. The linear equation $(y = 19406x + 6.3379)$ obtained from regression analysis was used to convert catalase activity measurements from AU/sec to U/mL. To validate this equation, three lung tissue supernatant samples were analyzed for catalase activity using both the assays to compare the calculated value (AU/sec obtained from H_2O_2 decomposition converted to U/mL) with the measured value (U/mL obtained from the catalase assay kit). The calculated values matched the measured values (Fig 4.8), thus validating the correlation and conversion between both the activity assays. In addition, the calculated catalase activity values (U/mL) (Fig. 4.4b and 4.5b) showed similar trends as the catalase activities measured using H_2O_2 decomposition (Fig. 4.4a and 4.5a) following intranasal and intravenous dosing of different catalase formulations.

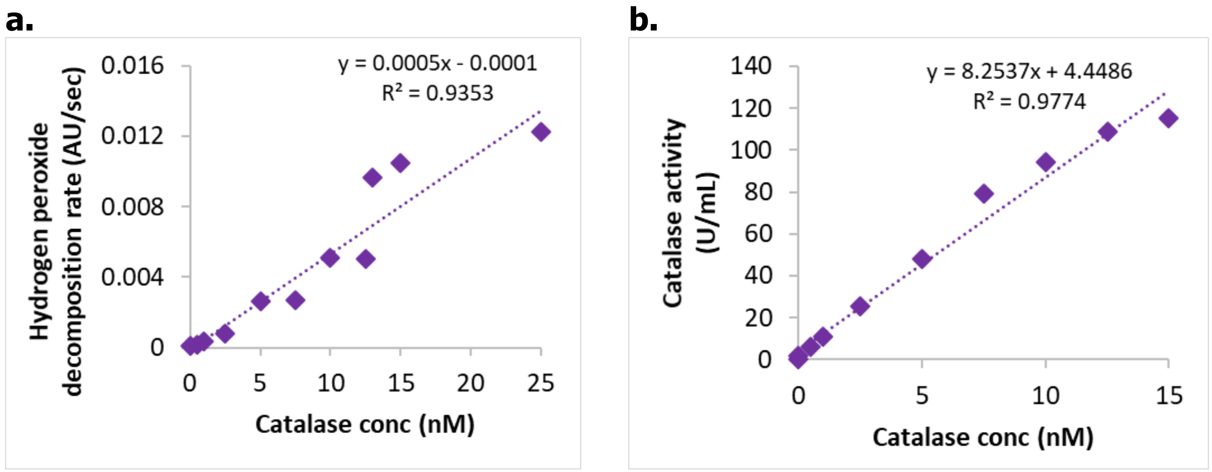

Fig. 4.6. Dependence of H_2O_2 decomposition rate (a) and catalase activity (b) on catalase concentration

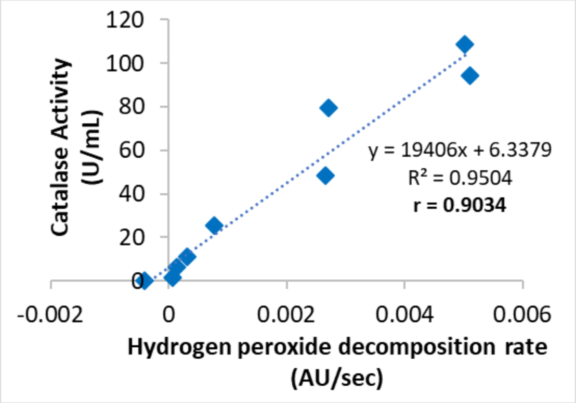

Fig. 4.7. Correlation between H_2O_2 decomposition rate and catalase activity

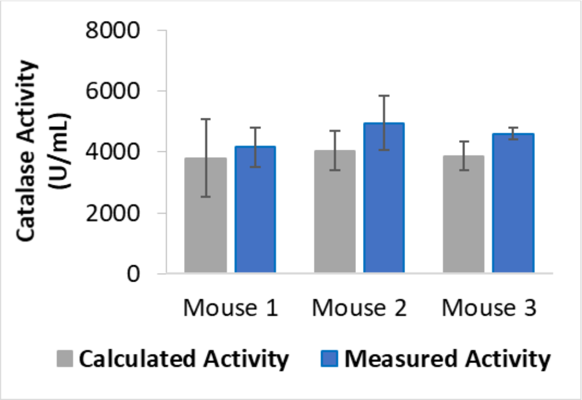

Fig. 4.8. Comparison between measured and calculated catalase activities. Data presented as mean ± SD (n=4).

4.4 Discussion

In this chapter, CC LPP and CE LPP formulations were evaluated for their protein delivery efficiency into healthy lung tissue in mice. Lung was chosen as the target organ in order to explore LPP's potential applications in clinically relevant diseases that are associated with lung inflammation. Catalase has been reported to mitigate the pathology of inflammatory diseases by protecting the cells from oxidative stress [45]. The intravenous route of administration was chosen to target the endothelial cells in the lung capillaries whereas intranasal route was chosen to target the bronchiolar and alveolar epithelial cells in the lung.

Intravenous administration of cationic lipoplexes for gene delivery result in accumulation of majority of the administered dose in pulmonary capillaries in the lung [50, 51]. In contrast, intravenously injected cationic LPP formulations in our study did not accumulate substantially into the lung but distributed quickly into the liver. This could be due to lower serum stability of the LPP constructs than cationic lipoplexes of DNA or siRNA, and/or rapid clearance by the reticuloendothelial system (RES) [109, 110]. Forster resonance energy transfer (FRET) can be employed in the future to monitor the extent of dissociation of LPP formulations in serum [111]. In order to reduce LPP's clearance and prolong its circulation time in the blood, hydrophilic polyethylene glycol (PEG) polymers can be used to coat LPP's surface to shield its positively charged, hydrophobic surface from opsonization [62, 112]. The LPP surface could also be modified with a ligand to target endothelial receptors such as platelet-endothelial cell adhesion molecule (PECAM) because the pulmonary endothelium is the preferential accumulation site for endothelial-targeted carriers [113, 114].

The partial success of tail-vein injection was one of the limitations of this study. As an alternative to tail-vein injection, penile-vein injection in male mice could be tested to improve the success rate of intravenous administration. The penile vein is clearly visible, easy to inject and is surrounded by tissue rich in capillaries which can enhance systemic absorption of injections that miss the vein [115].

Success of intranasal administration is governed by parameters such as depth of anesthesia, animal position and dose volume [102]. In order to avoid inhomogenous dosing, these parameters were carefully controlled. A dose volume of ~36 µL was chosen based on prior studies where 25-50 µL was found to be the ideal volume for lung delivery [103]. Of the fluorescently labeled formulations successfully delivered via intranasal route, f-CC LPP showed higher distribution and retention in the lung. The intranasal administration of f-CE LPP might have been partially successful because the mice treated with these formulations showed noticeably lower signal in the lungs, head and paws compared to other treatment groups. The smaller particle size and the positive charges of f-CC LPP may have boosted their dispersion, cellular binding and cellular uptake in the lung tissue [60].

Airways are lined by mucus, which is a hydrogel complex composed of secreted polypeptides, proteins, carbohydrates, lipids, antibodies and cellular debris tethered together by dense network of mucin fibers. The mucus layer protects the underlying tissue from exposure to external environment and its barrier properties are rooted in its dense network of hydrophobic, negatively charged, glycosylated mucin fibers [116]. The lipophilic, positively charged CC LPP system may have been trapped in the mucus membranes of the nasal passages, which could explain the high intensity in the head region. Surface coating with hydrophilic, low molecular weight PEG can be explored to shield the positive surface charges of LPP in order to reduce interactions between the LPP nanocarrier and mucus [117].

Another limitation of this study was both the H_2O_2 decomposition assay and the catalase assay kit measured the combined activities of endogenous murine catalase and exogenous bovine catalase. An unanticipated observation was that intranasal delivery of exogenous catalase lowered the catalase activity in the lung compared to the control group that received an equal volume of PBS. In order to understand the underlying cause for this decrease in catalase activity, two different enzyme-linked immunosorbent assay (ELISA) kits can be employed to distinguish and specifically detect the levels of endogenous murine catalase and exogenous bovine catalase. Additionally, ELISA can be useful to detect the total catalase concentration in a sample accounting for both functional and denatured protein, whereas, catalase activity measurement is limited to the detection of the functional protein.

Although it may be argued that the LPP formulations only alleviated the ROS damage from the intrapulmonary administration itself, intrapulmonary delivery of the catalase protein by LPP was evident, which prompted further evaluation of both the LPP formulations (CE LPP and CC LPP) in a mouse model of lung inflammation to test their potential therapeutic benefits.

Chapter 5: Evaluation of the Potential Therapeutic Efficacy of LPP in a Murine Inflammatory Lung Disease Model

5.1 Introduction

The aim of this chapter is to test the potential therapeutic efficacy of LPP in a clinically relevant inflammatory lung disease model in mice.

5.1.1 Clinically relevant inflammatory lung diseases. Inflammation is involved in numerous clinically important lung diseases, including chronic obstructive pulmonary disease, asthma, acute lung injury, bronchitis, pneumonia, influenza and tuberculosis.

Chronic obstructive pulmonary disease (COPD) is mainly caused by exposure to cigarette smoke and inhaled pollutants. It is characterized by chronic airway inflammation and airflow obstruction, which lead to a progressive and irreversible decline in lung function [118]. In COPD, the activated structural and inflammatory cells (epithelial and alveolar macrophages) release chemotactic mediators to recruit T cells, neutrophils, monocytes and lymphocytes into the lung, triggering chronic inflammation that leads to structural changes and obstruction of the airway.

Asthma, a heterogeneous airway disorder, is also associated with chronic inflammation of the airways, declining lung function and tissue remodeling [98]. Clinical symptoms of asthma include breathlessness, wheezing and varying degrees of airflow obstruction. In asthma, the conducting airways become hyper-responsive and highly sensitive to a given stimulus and react by bronchoconstriction, which is usually treated by bronchodilators.

Acute lung injury (ALI) or acute respiratory distress syndrome (ARDS) is an acute inflammatory disorder characterized by disruption of endothelial and epithelial barriers, loss of alveolar-capillary membrane integrity, excessive recruitment of neutrophils and elevated levels of pro-inflammatory, cytotoxic mediators in the lung (Fig. 5.1) [44].

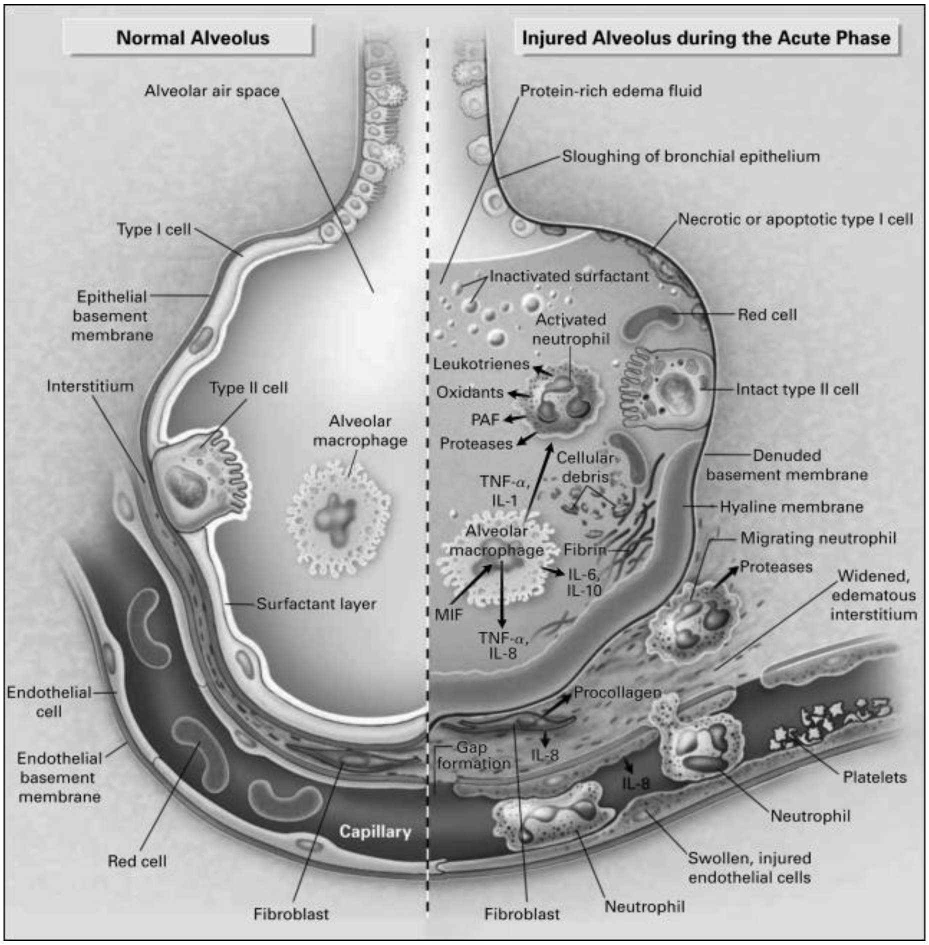

Fig. 5.1. Diagrammatic representation of the normal alveolus (left) and the injured alveolus in the acute phase of ALI/ARDS (right) (Adapted from ref.[44])

ALI/ARDS is an unmet medical need and a major cause of morbidity and mortality in critically ill patients. Recent advances have led to reduction in the duration of mechanical ventilation and improvement of survival time with a lung-protective ventilation strategy [119].

5.1.2 Pre-clinical models of inflammatory lung diseases.

Lipopolysaccharide (LPS) is an endotoxin derived from the outer membrane of gram-negative bacteria, which contains three regions (Fig. 5.2): an O-antigen with repeating oligosaccharide units, core sugars, and phospholipid A containing a di-glucosamine head group linked to acyl chains [120].

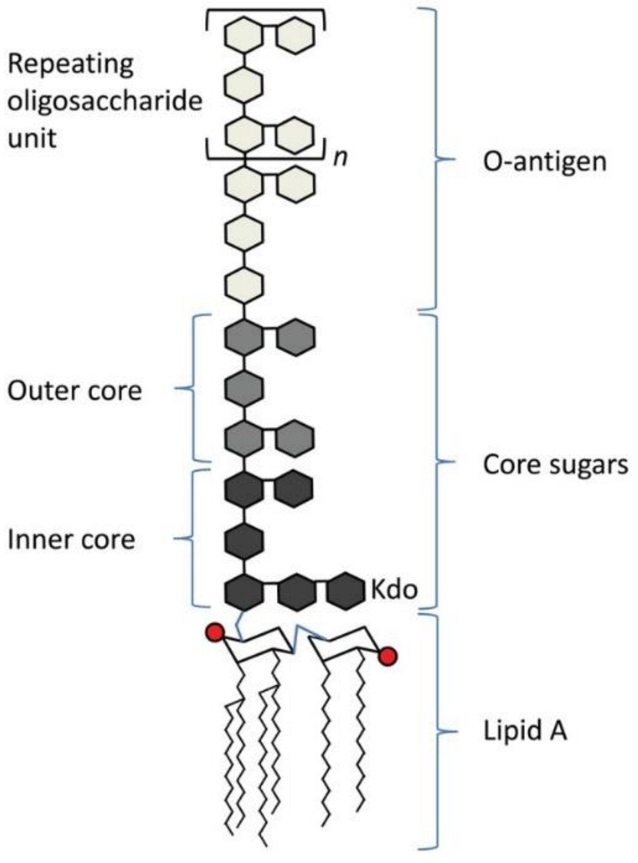

Fig. 5.2. Basic structure of lipopolysaccharide (Adapted from ref. [120])

LPS is recognized by the toll like receptor-4 (TLR4) present on alveolar macrophages and epithelial cells during pulmonary infection, which triggers a cascade of intracellular signaling pathways that activate nuclear transcription factors such as nuclear factor kappa-enhancer of activated B cells (NF-κB) [101]. NF-κB induces the production of pro-inflammatory cytokines such as interleukin-6 (IL-6), interleukin-1β (IL-1β), interferon-gamma (IFNγ) and tumor necrosis factor-alpha (TNF-α), which then upregulate chemokines to recruit neutrophils [121]. In the lung, activated neutrophils are a major source of reactive oxygen species that oxidize lipid and protein constituents of cells and damage the pulmonary endothelium [46, 122]. Acute inflammation induced by LPS further causes rapid deletion of endogenous antioxidants including catalase, superoxide dismutase and glutathione peroxidase.

LPS has been reported a potent agent to induce acute lung injury in mice following intranasal, intratracheal or intraperitoneal administration [123-125]. LPS has also been used for developing COPD models in mice, rats and guinea pigs [126]. Additionally, LPS induced an inflammatory reaction in human lungs in a clinical trial evaluating the effect of aspirin on reducing inflammation in human model of ALI [127]. In this trial, bronchoalveolar (BAL) levels of IL-8 was the primary outcome measured 6 hours after LPS inhalation. Secondary outcome measures included alveolar inflammatory markers such as neutrophils, cytokines and neutrophil proteases in BAL fluid (BALF) [127].

The intratracheal (IT) route of administration is well-established and technique of choice for lung delivery as it involves direct instillation of the dose volume into the trachea. In our study, LPS isolated from *Escherichia coli* (sterile serotype 0111.B4) was administered intratracheally to induce ALI in mice.

5.1.3 Role of catalase in alleviating inflammation. Catalase, an endogenous tetrameric heme protein, is one of the major intracellular antioxidant enzymes responsible for detoxifying reactive oxygen species (ROS) produced under physiological conditions. In the lung, catalase is expressed in macrophages, bronchiolar and alveolar epithelial cells and is a crucial part of its endogenous antioxidant defense system. Decreased endogenous levels of catalase have been reported in inflamed lungs associated with lung cancer, asthma and pneumonia [24, 45]. Additionally, Odajima *et al.* [45] reported that acatalasemic mice are more sensitive to bleomycin-induced inflammation and show prolonged upregulation of proinflammatory cytokines compared to wild-type mice. These reports suggest the role of catalase in regulating oxidative stress in inflammation. Therefore, LPP formulations loaded with catalase were delivered into inflamed mice lung to test if such formulations can replenish the depleted endogenous catalase and/or provide any therapeutic benefit to ALI.

5.1.4 Biomarkers selected for evaluation. For studies reported in this chapter, interleukin-6 (IL-6) and tumor necrosis factor-alpha (TNF-ɑ) were the biomarkers chosen for assessing inflammation in the lung. IL-6, a pro-inflammatory cytokine that is promptly produced in response to tissue injury, is a major contributor to the host’s defense mechanism by stimulating acute phase responses, hematopoiesis and immune reactions [128]. TNF-ɑ, a cytokine produced by macrophages and monocytes during acute inflammation, is responsible for triggering a variety of cell-signaling events that result in necrosis/apoptosis [129].

The degree of oxidative stress in the lung tissue was evaluated by measuring catalase activity, ROS levels and malondialdehyde (MDA) levels. Catalase activity measurement accounts for the endogenous catalase in the lung as well as the intrapulmonarily delivered catalase. Reactive oxygen species (ROS) consist of both radical and non-radical oxygen species such as hydrogen peroxide (H_2O_2), nitric oxide (NO), superoxide anion (O_2^-) and hydroxyl radical (•OH). ROS are produced endogenously during mitochondrial oxidative metabolism and in response to xenobiotics, cytokines and bacterial invasion. ROS generation beyond the cell's antioxidant capability results in oxidative stress [130]. MDA is a product of peroxidation of polyunsaturated lipids, and is used as a biomarker indicative of oxidative damage [131].

5.2 Materials and Methods

5.2.1 Materials. Pierce protease inhibitor cocktail and T-PER protein extraction reagents were purchased from Fisher Scientific (Hampton, NH). Carboxy-H_2DCFDA was purchased from Molecular Probes (Eugene, OR). Bovine liver catalase (E3289) was purchased from Sigma-Aldrich (St. Louis, MO). Cyanine7.5-labeled bovine liver catalase was purchased from Nanocs Inc (New York, NY). Lipopolysaccharide (L2630) was purchased from Sigma-Aldrich (St. Louis, MO). Isoflurane, ketamine, xylazine, and acepromazine were purchased from Patterson Veterinary (Greeley, CO).

5.2.2 Experimental animals. CD-1 female and male mice, 7 weeks old were purchased from Charles River Laboratories (Wilmington, MA). All work performed on animals was in accordance with and approved by the University of the Pacific Institutional Animal Care and Use Committee (Protocol# 18R12).

5.2.3 Development of lipopolysaccharide induced acute lung injury in mice. Acute lung injury (ALI) was induced in CD-1 mice, 8 weeks old at the time of experiment, by administering lipopolysaccharide (LPS) intratracheally [132]. To understand the role of LPS induction time in the disease model, CD-1 female mice (8 weeks old) were administered a suspension of LPS in PBS (1.5 mg/Kg LPS, n=3) or an equivalent volume of PBS (~50 µL, n=3) intratracheally and the lung tissues were collected and analyzed 4, 6 and 12 hours after LPS injury. Additionally, lung tissues from untreated mice (n=3) were collected and analyzed for comparison. In order to test if a higher amount of LPS would further upregulate the inflammatory and oxidative stress biomarkers, CD-1 female mice were administered a suspension of LPS in PBS (3 mg/Kg LPS, n=3) and the lung tissue was collected and analyzed 6 hours after LPS administration. Additionally, to understand the role of sex hormones in inflammation, CD-1 male mice (8 weeks old) were administered a suspension of LPS in PBS (3 mg/Kg LPS, n=3 and 1.5 mg/Kg LPS, n=3) or an equivalent volume of PBS (~50 µL, n=3) intratracheally and the lung tissues were collected and analyzed 6 hours later.

For intratracheal administration of LPS, the animals were first anesthetized with an intraperitoneal injection of anesthetic cocktail (65 mg/kg ketamine, 12 mg/kg xylazine and 2 mg/kg acepromazine). Once the animal was sedated, veterinary ointment was applied to its eyes and buprenorphine (0.05 mg/Kg) was administered subcutaneously. The neck was shaved and swabbed with betadine and alcohol. The mouse was placed supine on a platform sloped at 45-90° angle [133]. Sharp scissors were used to make a small surgical incision approximately 12 mm below the lower incisors. A one-inch long 20-gauge Jelco® IV catheter was used without the needle for intratracheal intubation. The skin near the neck was pulled caudally by forceps to visualize the ventral wall of the trachea through the incision. The tongue was gently retracted, and the white catheter was inserted into the trachea through the mouth. Once the insertion of catheter into the tracheal was visually confirmed, it was gently advanced further. An aqueous suspension of LPS in PBS was injected into the catheter using a gel-loading pipette tip. The lungs were quickly inflated by injecting 0.6 mL of air with a 1 mL syringe through the catheter to help disperse the liquid deep into the lungs, immediately followed by removal of the catheter. The incision was sealed with surgical glue and all tools used for LPS administration were removed. To avoid the interference of any fluorescence signal from the surgical glue in the neck region, the incision was sealed with a suture in the animals used for the fluorescence imaging study (5.2.5). The animals were kept warm by a lamp while under anesthesia and were continuously monitored.

5.2.4 Evaluation of LPP's antioxidant effects in mice of ALI. To evaluate the efficiency of the LPP delivery system in inflamed lungs, CD-1 male mice were randomly divided into ten groups (n=8): LPS + CC LPP/intranasal, LPS + CE LPP/intranasal, LPS + Free CAT/intranasal, LPS + Vehicle(LPS control)/intranasal, PBS + Vehicle(control)/intranasal, LPS + CC LPP/intratracheal, LPS + CE LPP/intratracheal, LPS + Free CAT/intratracheal, LPS + Vehicle(LPS control)/intratracheal and PBS +

Vehicle(control)/intratracheal. Lung inflammation was induced in the animals under anesthesia by administering 3 mg/Kg LPS by intratracheal intubation as described above. The healthy control group received an equal volume (~30 µL) of PBS. The animals that received treatments via intranasal route were anesthetized with a lower dose of anesthetic cocktail to ensure they were almost awake at the time of intranasal administration (30 minutes post-LPS administration). The mice were treated with the respective formulations containing 0.3 mg/Kg catalase 30 minutes post-LPS administration and then allowed to recover from anesthesia. The control group received an equal volume (~30 µL for IN, ~50 µL for IT) of the formulation vehicle (5mM HEPES, 5% w/v glucose, pH 7.4).

CC LPP and CE LPP were prepared as described in Chapter 4 (4.2.3) and contained 19.2 mM total lipid and 1.2 µM catalase (in 5mM HEPES buffer with 5% w/v glucose) for IN administration and 12.8 mM total lipid and 0.8 µM catalase (in 5mM HEPES buffer with 5% w/v glucose) for IT administration. Free catalase solutions of equivalent concentrations (1.2 µM for IN and 0.8 µM for IT) were prepared in HEPES buffer (5mM HEPES, 5% w/v glucose).

5.2.5 Fluorescence imaging of LPP distribution in mice of ALI. In a separate study, cyanine 7.5-labeled catalase (Nanocs Inc., NY) was used to fluorescently image the distribution of the encapsulated and the complexed LPP formulations (CE LPP and CC LPP, respectively) in an inflammatory acute lung injury (ALI) model. CD-1 male mice were randomly divided into six groups (n=3 each): LPS + CC LPP/intranasal, LPS + CE LPP/intranasal, LPS + free CAT/intranasal, LPS + CC

LPP/intratracheal, LPS + CE LPP/intratracheal and LPS + free CAT/intratracheal. The animals were anesthetized followed by intratracheal administration of 3 mg/Kg LPS to induce lung inflammation. The animals were kept under anesthesia and received group-specific treatments containing 0.3 mg/Kg fluorescently labeled catalase 30 minutes after LPS administration. The animals were imaged on a LI-COR Pearl Trilogy small animal imaging system (LI-COR Biosciences, Lincoln, NE) (Instrument settings: Resolution :170 μm, Focus: 0 mm, Channels: 700 nm, 800 nm and white) to detect the fluorescence of the Cy-7.5 dye (λ_{ex} = 790 nm, λ_{em} = 810 nm). Images were captured at select time points up to 24 hours post catalase treatment. The animals were then perfused with PBS and their lungs, liver, kidneys and brain tissue were collected for *ex vivo* imaging. Image Studio Lite (LI-COR Biosciences) was used to process and analyze the images. All the images were normalized by fixing the intensity scale to the same minimum and maximum value. Signal intensity (SI) was obtained from regions of interest such as head, lungs and abdominal region by drawing box shapes in each mouse. The box drawn in the lung region was further divided into three equal boxes representing upper airway/lung region, mid-lung region and deep lung region. Mean signal intensity (MSI) was calculated by dividing the SI with the area of the box. Normalized intensity percent was calculated by:

$$\text{Normalized intensity \%} = \frac{\text{MSI}_{\text{region of interest}}}{\text{MSI}_{\text{background}}} * 100$$

Where $\text{MSI}_{\text{region of interest}}$ corresponds to the MSI obtained from a specific region (for example, deep lung of mice treated with CC LPP at 0.5 hour) and $\text{MSI}_{\text{background}}$

corresponds to the MSI obtained for the same region from an untreated mouse (background intensity). The normalized intensity percent for *ex vivo* tissue images was calculated in a similar manner [106].

5.2.6 Tissue collection and analysis. Six hours after LPS administration followed by different catalase treatments (5.2.4), the animals were anesthetized with an intraperitoneal injection of anesthetic cocktail (65 mg/kg ketamine, 12 mg/kg xylazine and 2 mg/kg acepromazine), and their tracheas exposed and intubated with a 20 G IV catheter. PBS (1 mL, with protease inhibitor) was then injected through the catheter followed by gentle suction to collect the bronchoalveolar lavage fluid (BALF) [134]. The BALF samples were centrifuged at 800 g for 10 minutes at 4 °C on a Micromax RF microcentrifuge (Thermo Fisher Scientific, Waltham, MA). The lungs were flushed with ice-cold PBS, removed and transferred into tubes containing T-PER lysis buffer with protease inhibitors. Zirconium beads were then added into the tubes and the lung tissue samples were homogenized on a Mini Bead-Beater 1 (BioSpec Products, Bartlesville, OK) followed by centrifugation at 14000 g for 15 minutes at 4 °C on a Micromax RF microcentrifuge (Thermo Fisher Scientific, Waltham, MA). The resultant bronchoalveolar lavage fluid and lung tissue supernatant samples were stored on ice for immediate use or transferred to -80 °C for future analysis.

5.2.6.1 Measurement of cytokines. Pro-inflammatory cytokines IL-6 and TNF-α in the lung tissue supernatants and BALF were measured using respective DuoSet® ELISA kits (R&D Systems, Minneapolis, MN) per manufacturer’s protocol. ELISA assay was validated by spike-and-recovery, and the appropriate fold of sample dilutions was identified to ensure that the readings fall into the linear range of the assay. Briefly, the tissue supernatant and BALF samples were assayed at multiple dilutions (neat sample, 10-fold, 100-fold, 1000-fold, 10000-fold), with and without a spike of known amount of standard. Based on the results of the sample validation, tissue supernatants were diluted 1000-fold and BALF was diluted 100-fold to fit into the linear range of the ELISA. The absorbance of the samples was measured at 450 nm (corrected with absorbance at 540 nm) using an Epoch Microplate Spectrophotometer (BioTek Instruments Inc, Winooski, VT).

5.2.6.2 Measurement of catalase activity. Catalase activity in the lung tissue supernatants and BALF was measured immediately on the day of experiment using a catalase assay kit (Cayman Chemical, Ann Arbor, MI) per the manufacturer's instructions. Tissue supernatants were diluted 100-fold and BALF was diluted 10-fold to fit into the linear range of the assay. The absorbance of the samples was measured at 540 nm using an Epoch Microplate Spectrophotometer (BioTek Instruments Inc, Winooski, VT).

5.2.6.3 Measurement of ROS levels. The ROS levels in the lung tissue supernatants and BALF were measured immediately on the day of experiment using the fluorescent probe Carboxy H_2DCFDA [107]. Briefly, 10 µL of 50 µM Carboxy H_2DCFDA was added to 100 µL of tissue supernatant (diluted 10-fold in lysis buffer) or 100 µL of BALF in a 96-well plate, which was then incubated for an hour at 37 °C. The fluorescence (λ_{ex} = 485 nm, λ_{em} = 528 nm) was measured on a BioTek Synergy HT microplate reader (BioTek Instruments Inc, Winooski, VT).

5.2.6.4 Measurement of malonaldehyde. Lipid peroxidation in the lung tissue supernatants was determined by measuring the malonaldehyde content using the TBARS-TCA method assay kit (Cayman Chemical, Ann Arbor, MI) per the manufacturer's instructions. The absorbance of the samples was measured at 540 nm using an Epoch Microplate Spectrophotometer (BioTek Instruments Inc, Winooski, VT).

5.2.6.5 Measurement of total protein. The total protein in the lung tissue supernatants and BALF were measured using the Pierce BCA protein assay (Thermo Fisher Scientific, Waltham, MA) per the manufacturer's instructions. Tissue supernatants were diluted 10-fold and BALF was used as is to fit into the linear range of the assay. The absorbance of the samples was measured at 540 nm using an Epoch Microplate Spectrophotometer (BioTek Instruments Inc, Winooski, VT).

5.2.7 Statistical analysis. Values that had both biological (multiple mice) and analytical (multiple measurements) replicates are expressed as mean ± SEM. One-way ANOVA paired with Tukey's posthoc analysis was performed using GraphPad Prism (GraphPad Software). Statistical significance was acknowledged at $p < 0.05$.

5.3 Results

5.3.1 Lipopolysaccharide-induced acute lung injury in mice. To establish a robust inflammatory lung disease model in CD-1 mice, the influence of a number of parameters such as duration of LPS induction, amount of LPS administered and sex of the animal was studied. Cytokines IL-6 and TNF-α levels in lung tissue were evaluated as biomarkers of inflammation. Catalase activity, ROS levels and lipid peroxidation were evaluated as markers of oxidative stress.

5.3.1.1 Timing of tissue collection.

IL-6 (Fig. 5.3a) and TNF-α (Fig. 5.3b) levels in the lung tissue were significantly elevated at 4 hours and 6 hours post LPS injury, confirming the onset of inflammation in the lung. The cytokine levels nearly returned to baseline 12 hours after LPS injury. Catalase activity (Fig. 5.3c) decreased in the LPS group at the 4-hour and 6-hour endpoint, possibly because of the depletion of endogenous catalase in combating oxidative stress. At 4 hours, malondialdehyde levels (Fig 5.3d) were elevated in both the LPS and PBS groups. However, these levels returned to baseline at the 6-hour and 12-hour endpoint. No changes were observed in the baseline ROS levels (Fig. 5.3e) at any time point, following administration of LPS or PBS. The data suggests that LPS evidently induced lung inflammation in the early time points and then may have recovered in the later time points. Six-hour tissue collection endpoint was chosen for future studies [127].

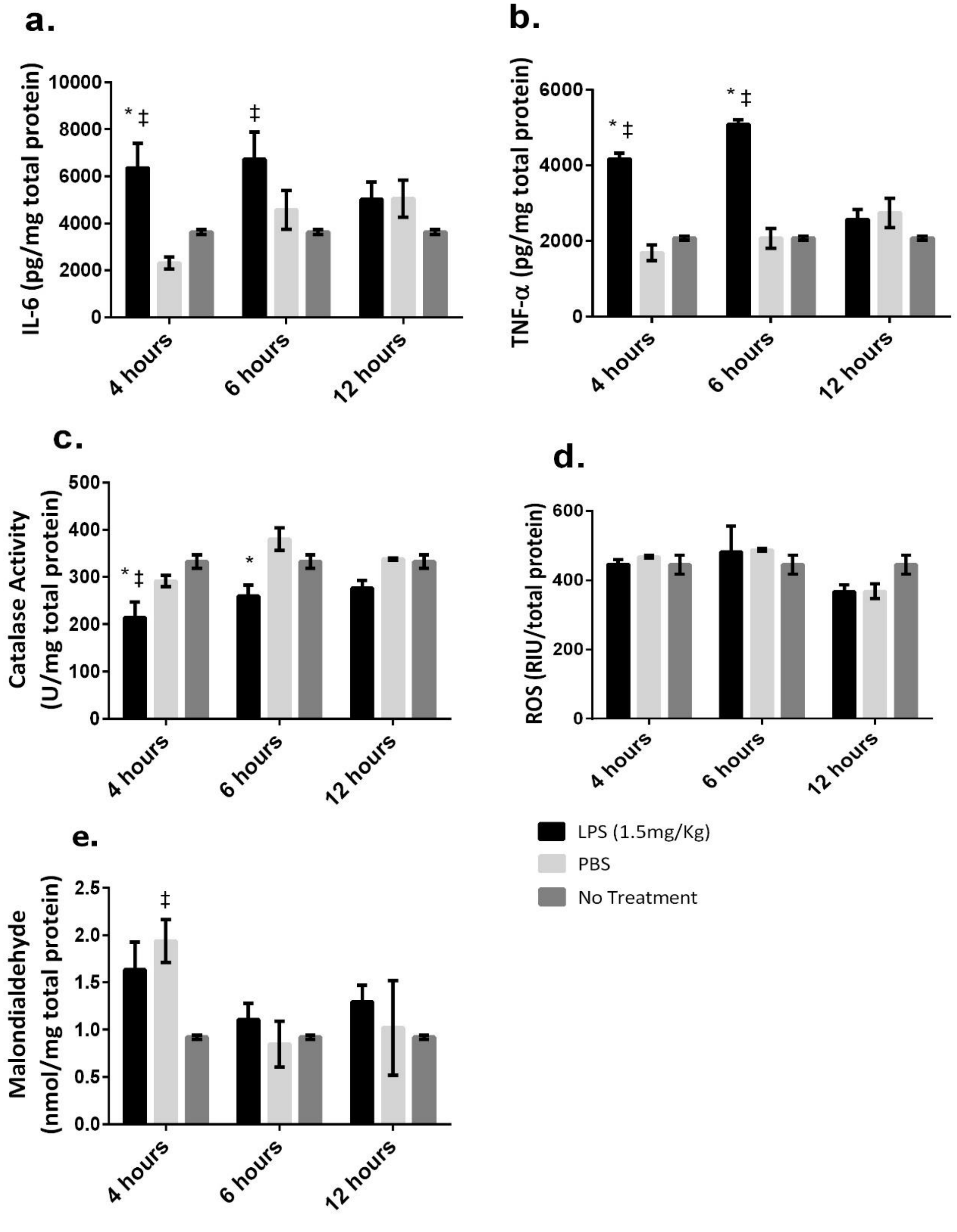

Fig. 5.3. Levels of interleukin-6 (a), tumor necrosis factor-alpha (b), catalase activity (c), reactive oxygen species (d) and malondialdehyde (e) in lung supernatants of CD-1 mice at different tissue collection time points. Data is presented as mean ± SEM (n=3). *$p<0.05$ versus PBS; ‡$p<0.05$ versus no treatment.

5.3.1.2 Effect of LPS dose. Double dose (3 mg/Kg) of LPS showed no significant upregulation of the inflammatory cytokines IL-6 (Fig. 5.4a) and TNF-α (Fig. 5.4b) in the lung tissue compared to the lower LPS dose (1.5 mg/Kg). No changes were observed in any of the oxidative stress biomarkers at this dose (Fig. 5.4c-e).

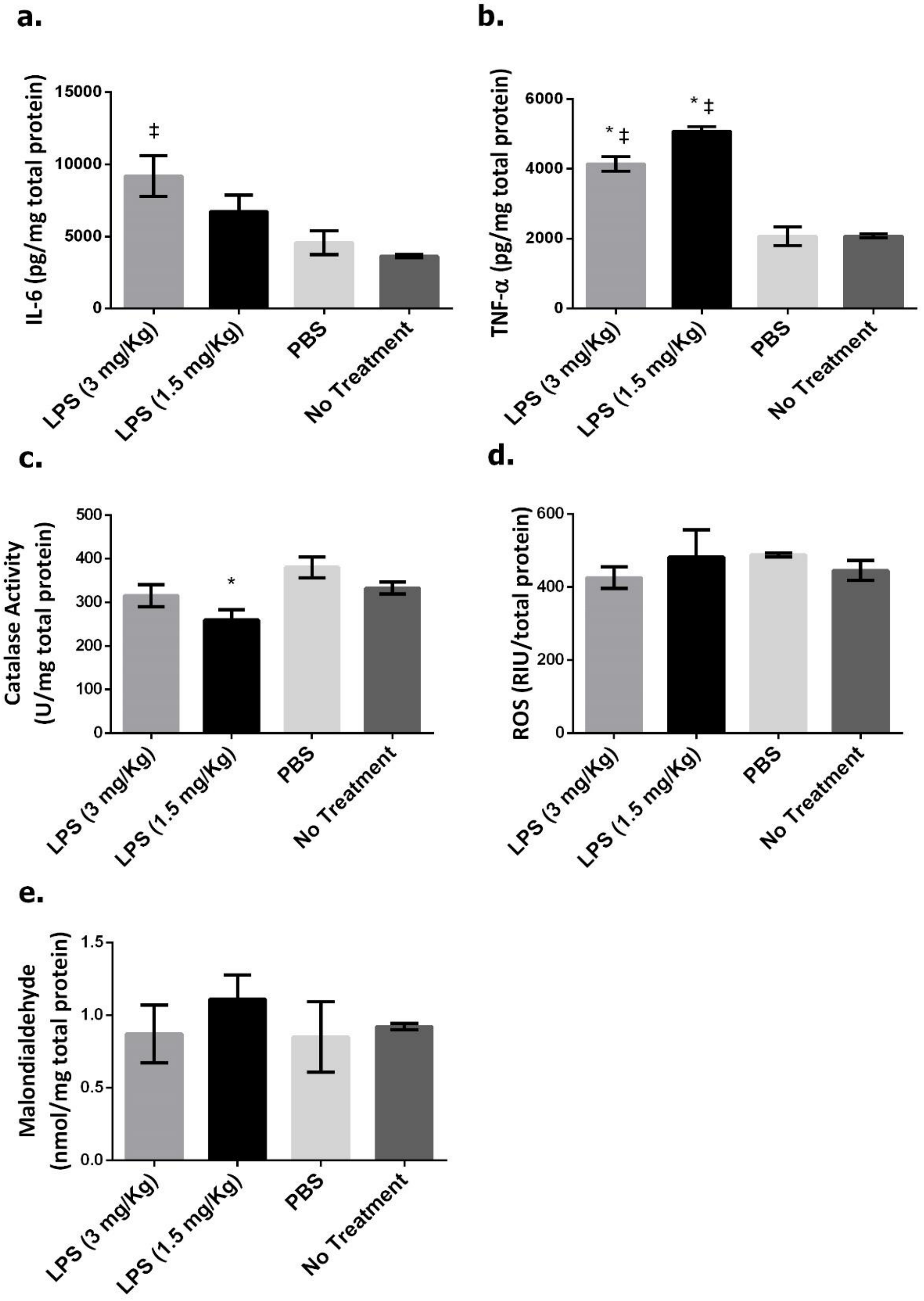

Fig. 5.4. Levels of interleukin-6 (a), tumor necrosis factor-alpha (b), catalase activity (c), reactive oxygen species (d) and malondialdehyde (e) in lung supernatants of CD-1 mice at different LPS doses. Data presented as mean ± SEM (n=3). *$p<0.05$ versus PBS; ‡$p<0.05$ versus no treatment.

5.3.1.3 Effect of sex. Sex hormones have been reported to play a major role in mice responsiveness to LPS-induced inflammation [135, 136]. Specifically, estrogen suppresses lung inflammatory responses in female mice. Therefore, male mice have enhanced functional and inflammatory responses to LPS compared to females. Male mice administered with LPS (3 mg/Kg) had 4.5-fold higher production of IL-6 than the PBS control, whereas female mice only showed 2-fold increase in the production of the same biomarker (Fig. 5.5a). Similarly, male mice showed 3-fold increase in TNF-α levels in the LPS (3 mg/Kg) group compared to the PBS control, whereas female mice only showed a 2-fold increase (Fig. 5.5b). The ROS levels and MDA levels in males were lower than females (Fig 5.5d, e). No differences were observed in the ROS levels (Fig. 5.5d) and MDA levels (Fig. 5.5e) between the LPS and PBS groups in males, which was similar to the observations made in female mice. Based on these findings, male mice were used for developing an ALI model to test the potential therapeutic efficacy of LPP formulations containing catalase.

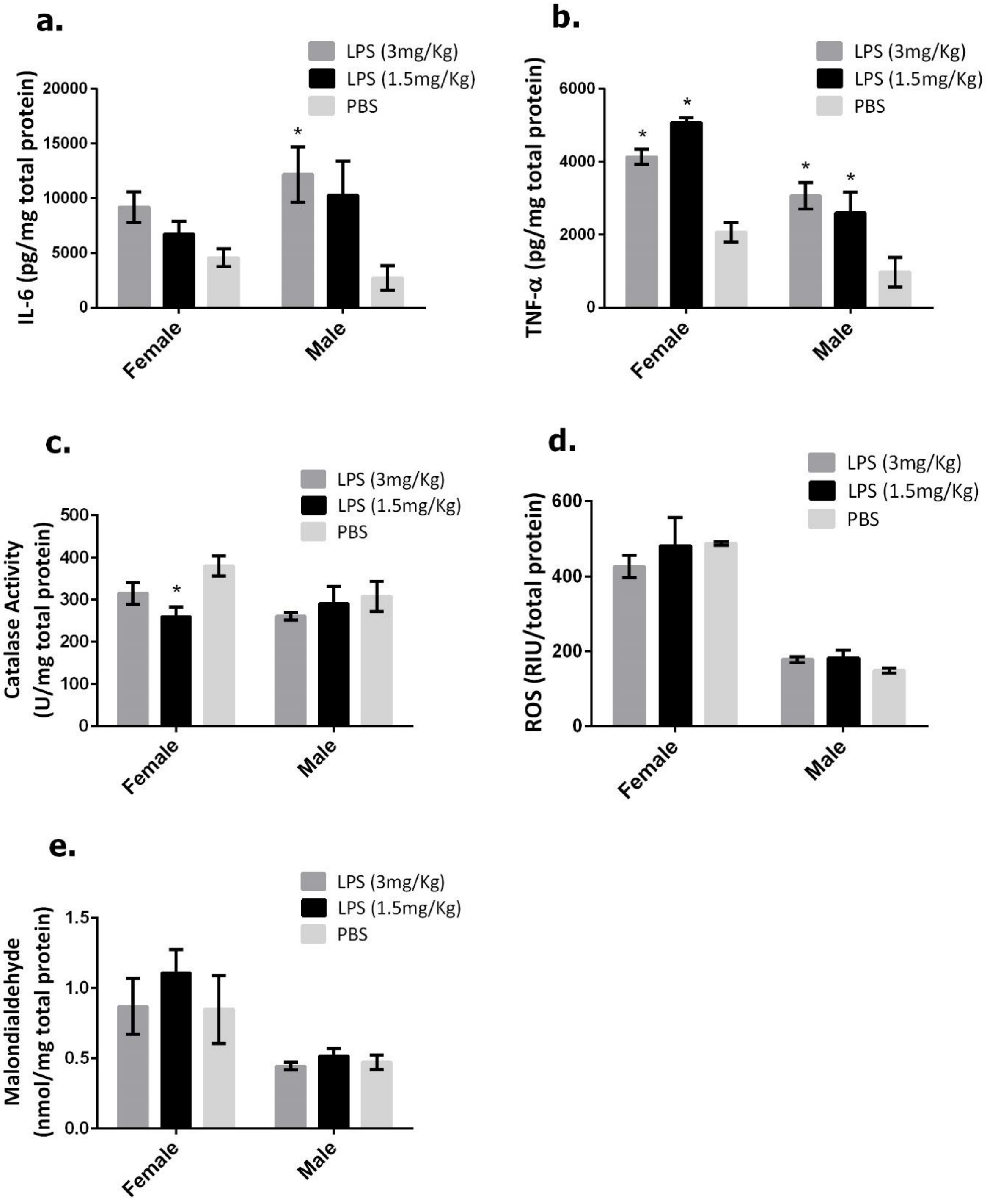

Fig. 5.5. Levels of interleukin-6 (a), tumor necrosis factor-alpha (b), catalase activity (c), reactive oxygen species (d) and malondialdehyde (e) in lung supernatants of female and male CD-1 mice. Data presented as mean ± SEM (n=3). *$p<0.05$ versus PBS.

5.3.1.4 Validation of ELISA. A number of strategies such as spike-and-recovery and linearity of dilution were employed to determine and validate the optimal fold of sample dilution for the enzyme-linked immunosorbent assay (ELISA) experiments. Immunoassays are usually prone to the high dose hook effect, which refers to measured levels of antigen displaying a significantly lower absorbance than the actual levels present in a sample [137], leading to false negatives or inaccurately low results. This usually occurs at higher concentrations of the analyte, where the excess antigen saturates the capture/detection antibodies. It may also occur from unknown interferences by other components present in biological samples, which makes dilution very important.

The hook effect was observed when neat lung tissue supernatant was analyzed for IL-6 using an ELISA kit (R&D Systems, Minneapolis, MN). The absorbance in the neat sample was very low compared to the 10-fold diluted sample (Fig. 5.6b). A linear relationship between measured absorbance and sample dilution was observed for the 10-fold, 100-fold, 1000-fold and 10000-fold dilutions. The diluted samples were spiked with a known standard and compared to a control group that received the same spike to determine the recovery. Spike recovery percent was calculated using either of the two equations:

$$\text{Spike recovery \%} = \frac{(\text{Absorbance}_{\text{sample with spike}} - \text{Absorbance}_{\text{sample without spike}})}{\text{Absorbance}_{\text{control with spike}}} * 100$$

$$\text{Spike recovery \%} = \frac{(\text{Conc}_{\text{sample with spike}} - \text{Conc}_{\text{sample without spike}})}{\text{Conc}_{\text{control with spike}}} * 100$$

where, Absorbance refers to the measured absorbance values ($\lambda_{450\text{-}540\ \text{nm}}$, corrected by subtracting blank absorbance) and Conc refers to the analyte (IL-6) concentrations interpolated from the standard curve (Fig. 5.6a).

A dilution fold of 1000 was chosen for subsequent studies because a) it had the highest spike recovery of greater than 90% and b) its absorbance (w/o spike) fit the linear range of the standard curve towards the lower concentration, allowing room for accurately interpolating increased analyte levels from the standard curve (Table 5.1). The optimal dilution fold for BALF samples (100-fold) was also determined in a similar manner.

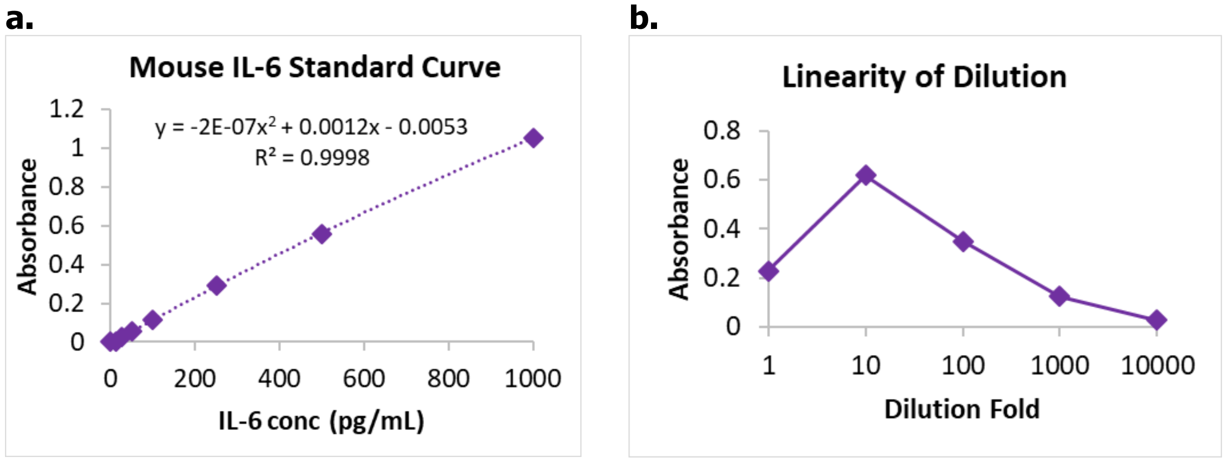

Fig. 5.6. Dependence of absorbance on the concentrations of mouse interleukin-6 standard (a) and lung supernatants (b)

Table 5.1. Recovery of IL-6 spike in lung supernatants at different dilutions

Sample #	**Dilution Fold**	**Absorbance w/o spike (AU)**	**Absorbance w/ spike (AU)**	**Spike recovery %**
1	1	0.228	0.434	28
2	10	0.619	1.116	68
3	100	0.35	0.911	76
4	**1000**	**0.125**	**0.807**	**93**
5	10000	0.027	0.678	89
Control	N/A	0	0.733	100

5.3.2 Biodistribution of LPP in mice of ALI. Intratracheal intubation of LPS (3mg/Kg) induced acute lung inflammation in CD-1 male mice as marked by the increase of pro-inflammatory cytokines TNF-α and IL-6 (Fig. 5.5a, b). The biodistribution of LPP formulations loaded with 0.3 mg/Kg Cy7.5-labeled catalase (f-CC LPP and f-CE LPP) after intranasal and intratracheal administration were compared to identify the better route for protein delivery in inflamed lungs. Following intranasal dosing, most of the signal appeared near the nose and throat of the mouse (Fig. 5.7) and the normalized intensity percent in the head region was about 10 times greater than the lung region in these mice (Fig 5.8a, b). However, the normalized intensity percent in the brain imaged *ex vivo* (Fig. 5.11b) remained at baseline (100%) following intranasal administration, which indicated that the high intensity in the head region was not because of distribution of Cy7.5-labeled catalase into the brain.

Administration of the catalase formulations (f-CC LPP, f-CE LPP and free f-CAT) into the lung by intratracheal intubation helped overcome the limited distribution of the formulations by intranasal dosing in mice with acute lung injury. Following intratracheal administration, the Cy7.5-labeled catalase was delivered deep into the lung (Fig. 5.9). The normalized intensity percent in the lung region, specifically the deep lung was greater in the mice treated with free f-CAT compared to f-CC LPP and f-CE LPP groups (Fig. 5.10b, f). The normalized intensity percent in the lungs imaged *ex vivo* corroborated both our findings: a) free f-CAT had higher lung distribution than the f-CC LPP and f-CE LPP groups following intratracheal administration and b) Cy7.5-labeled catalase formulations did not distribute into the lung following intranasal administration (Fig. 5.11a). Mice treated intratracheally with free f-CAT, had higher signal in the liver and kidneys compared to other groups, possibly due to its elimination by hepatic or renal pathways (Fig, 5.11c, d). Based on these findings from the biodistribution study, intratracheal route was considered more suitable for lung delivery in mice with ALI.

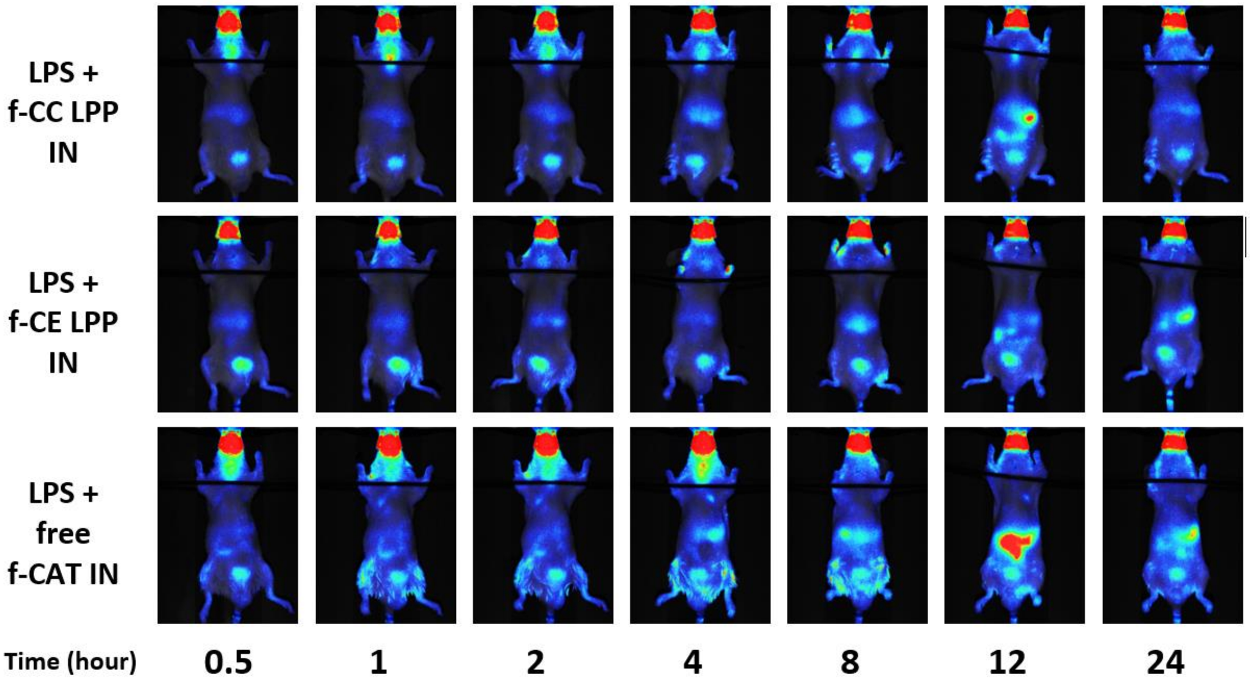

Fig. 5.7. Biodistribution of different Cy7.5-labeled catalase formulations after intranasal (IN) administration in CD-1 mice with ALI

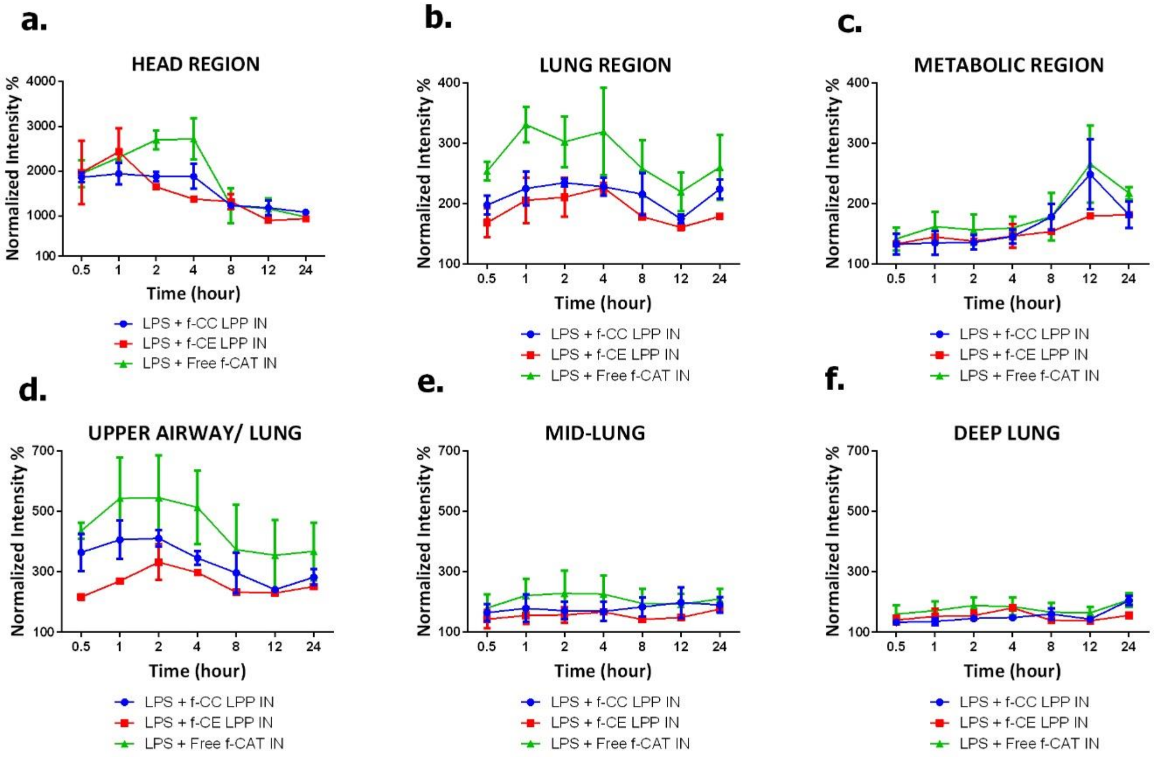

Fig. 5.8. Normalized fluorescence intensity of Cy7.5-labeled catalase in the head (a), lung (b) and metabolic (c) regions of CD-1 mice with ALI after intranasal administration. Intensity in the lung was divided into upper lung (d), mid-lung (e) and deep lung (f). Data presented as mean ± SD (n=3).

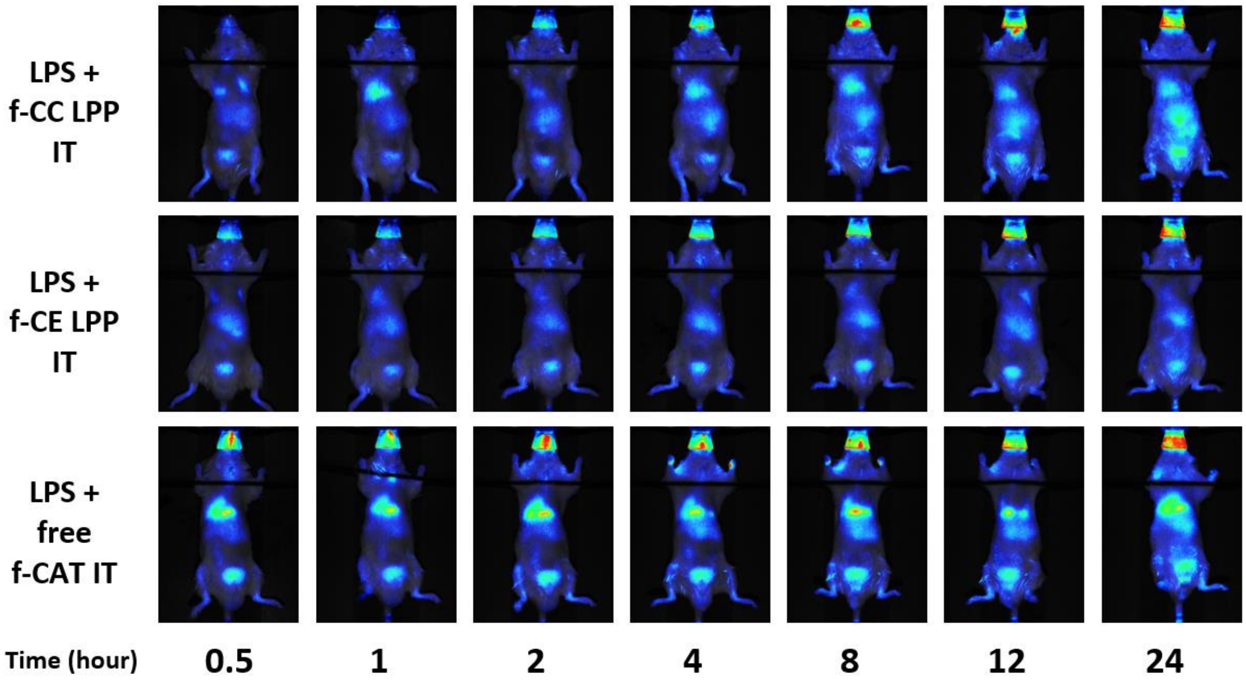

Fig. 5.9. Biodistribution of different Cy7.5-labeled catalase formulations after intratracheal (IT) administration in CD-1 mice with ALI

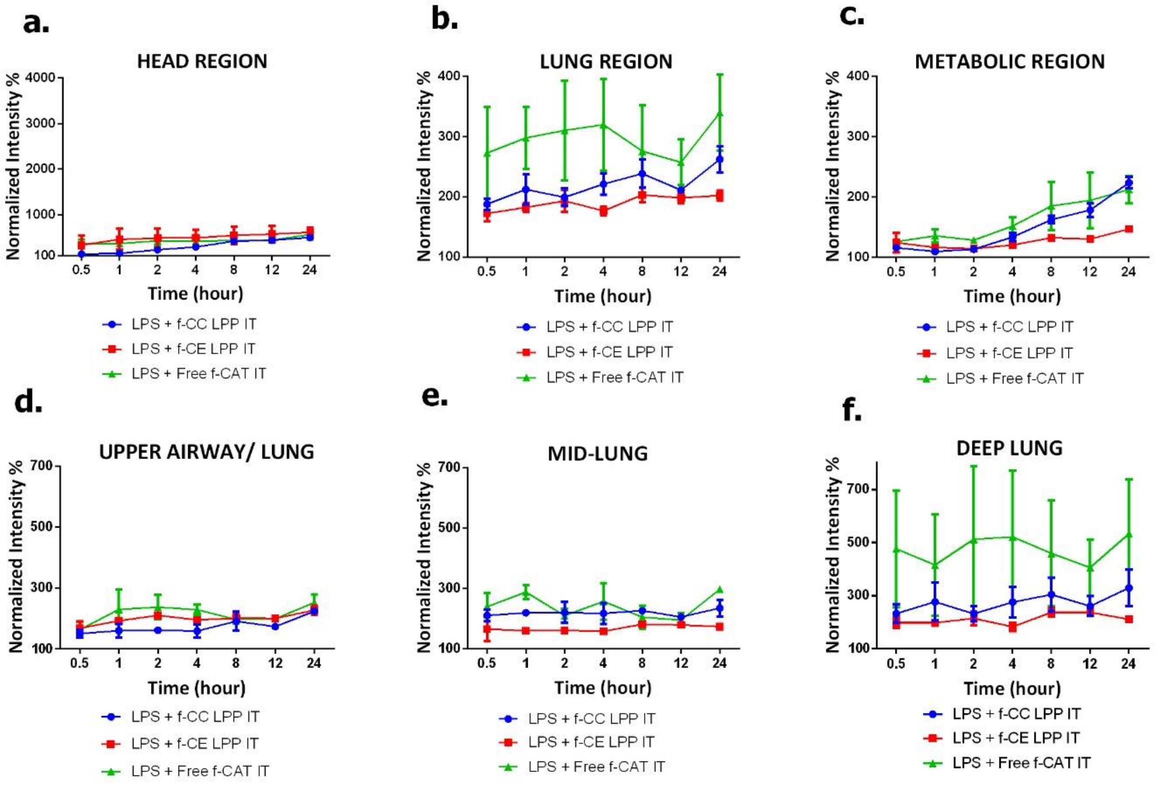

Fig. 5.10. Normalized fluorescence intensity of Cy7.5-labeled catalase in the head (a), lung (b) and metabolic (c) regions of CD-1 mice with ALI after intratracheal administration. Intensity in the lung was divided into upper lung (d), mid-lung (e) and deep lung (f). Data presented as mean ± SD (n=3).

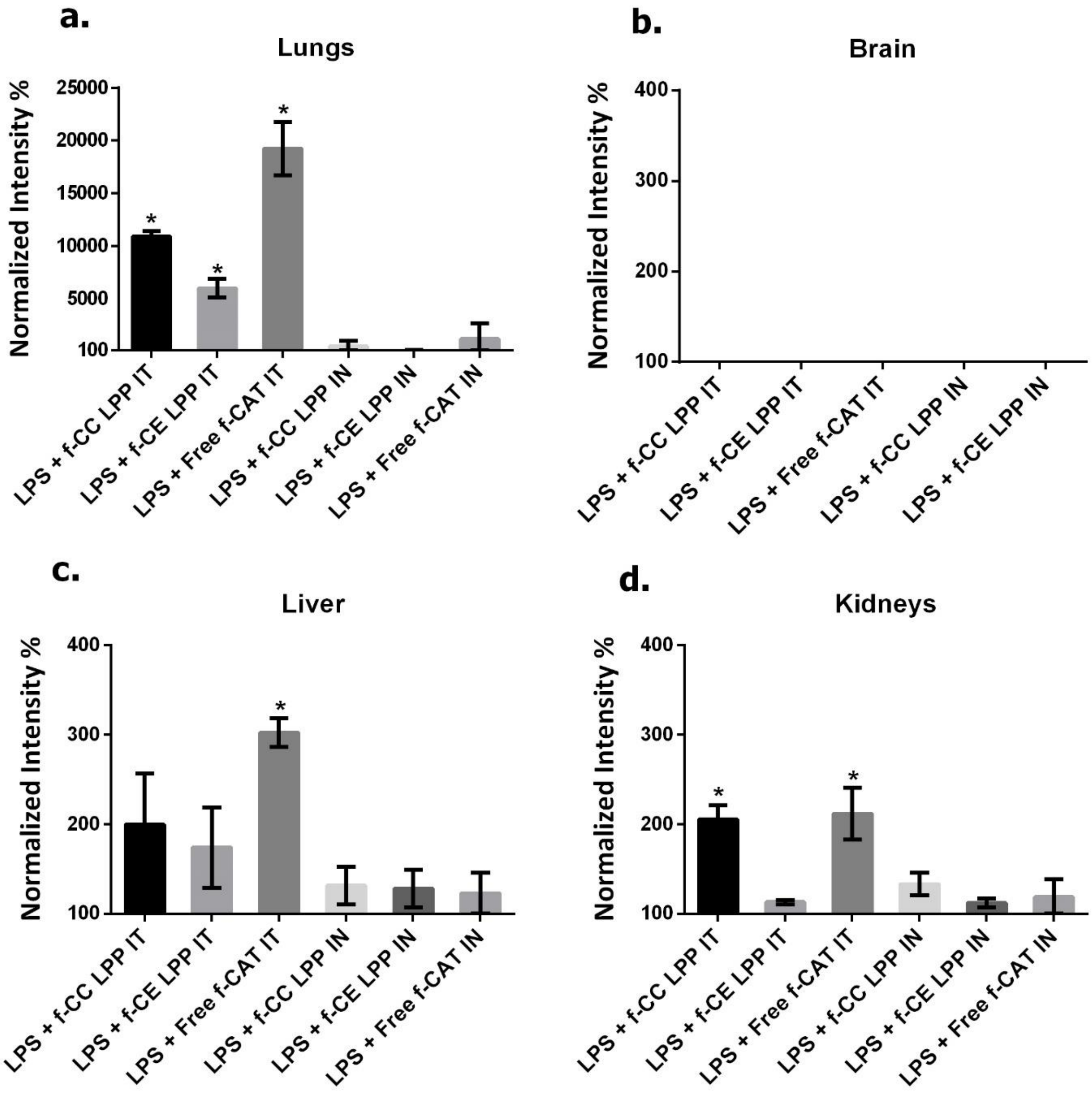

Fig. 5.11. Fluorescence intensity of Cy7.5-labeled catalase in the lungs (a), brain (b), liver (c) and kidneys (d) imaged *ex vivo* normalized to the fluorescence intensity from respective untreated organs. Data presented as mean ± SD (n=3). *$p<0.05$.

5.3.3 Efficacy of LPP in inflamed mouse lungs. Cytokines play a crucial role during inflammation. TNF-α is one of the most important pro-inflammatory cytokines which was upregulated in both the tissue supernatant (TS) and bronchoalveolar lavage fluid (BALF) in the LPS control group when compared to the healthy control group. None of the markers showed any substantial changes following intranasal dosing of treatments (Fig. 5.12), which correlated with our findings from the biodistribution images which indicated that treatments administered intranasally 30 minutes post LPS injury did not distribute into the lung. Following intratracheal administration, CC LPP and CE LPP significantly reduced TNF-α production in the lungs as compared to LPS-challenged animals (Fig. 5.13a, b). CC LPP lowered the TNF- α levels to a greater extent than CE LPP group in the lung supernatant, which could be a result of the following: 1) CC LPP carried a lower diameter than CE LPP which could improve its penetration and distribution into the lung tissue, 2) CC LPP preserved the activity of the cargo protein better than CE LPP and thus delivered more functional protein into the lungs. This is supported by the increased catalase levels in the bronchoalveolar fluid following treatment with CC LPP compared to CE LPP (Fig. 5.13d). Although, free catalase was also delivered into the airways of the lung and showed similar catalase activity level as CC LPP (Fig. 5.13d), the increased catalase activity did not translate into reduction of TNF- α as seen in the CC LPP group (Fig. 5.13b). This emphasizes the importance of LPP in delivering catalase into the cells to augment the natural antioxidant pool in the lungs, which can promote its ability to scavenge excessive ROS and restore its redox balance in disease conditions.

Another important observation was the spike in IL-6 levels in both the tissue supernatant and bronchoalveolar lavage fluid following intratracheal administration of both the LPP formulations (Fig. 5.13e, f), which could indicate toxicity. In addition, the elevated bronchoalveolar total protein concentration in both the LPP groups, is a sign of neutrophil infiltration, a hallmark of pulmonary edema [101]. In corroboration, animals treated intratracheally with LPP formulations showed reduced movement compared to other groups. This behavior was not observed when healthy mice were treated with LPP formulations.

Intranasal and intratracheal dosing of different catalase treatments caused no substantial changes in the tissue ROS levels in mice with ALI. The fluorescence signal that corresponds to the ROS levels in the bronchoalveolar fluid was very low and did not show any significant trends between the different treatment groups.

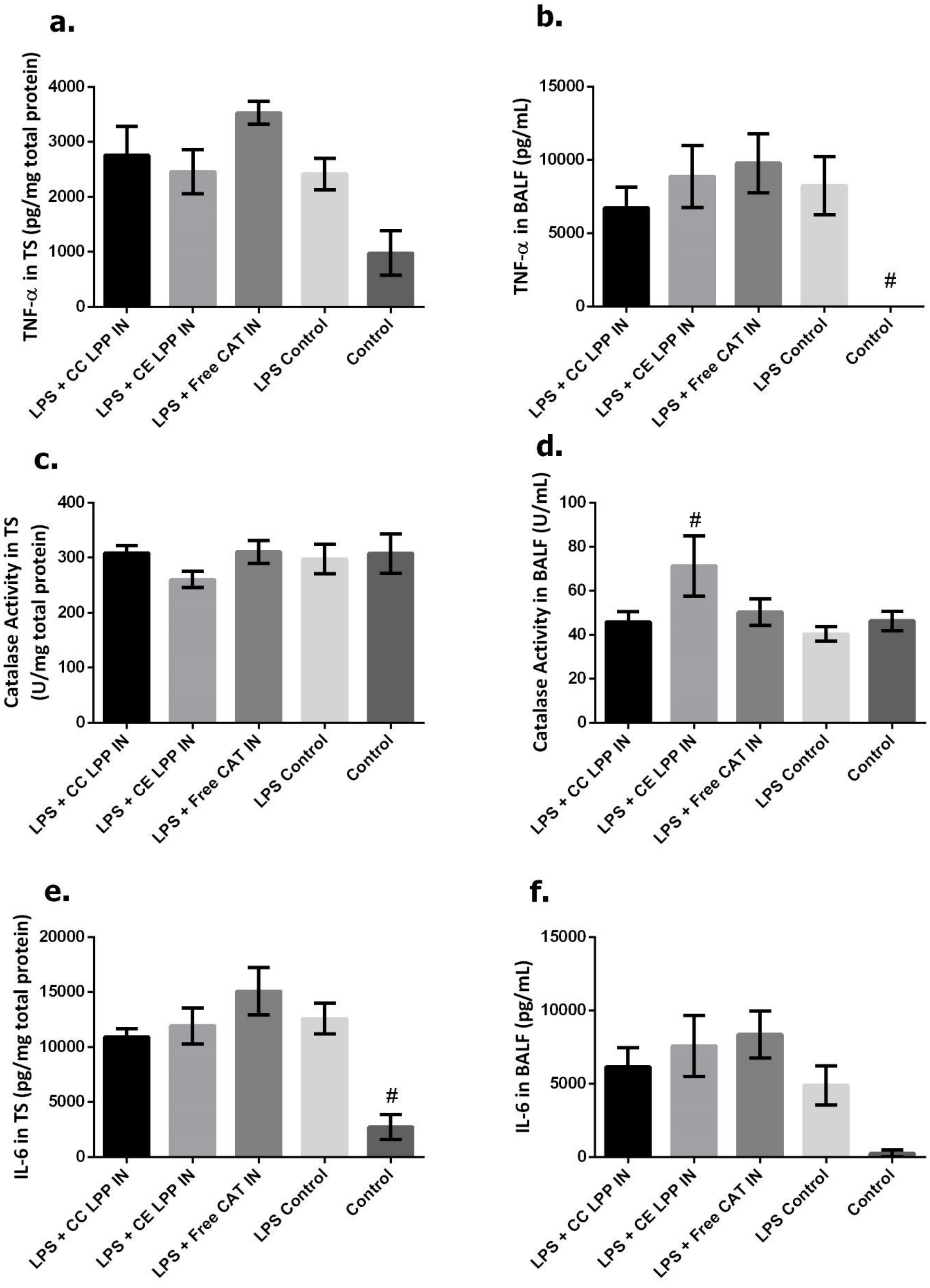
a.
TNF-α in TS (pg/mg total protein)
4000
3000
2000
1000
0
LPS + CC LPP IN
LPS + CE LPP IN
LPS + Free CAT IN
LPS Control
Control
b.
TNF-α in BALF (pg/mL)
15000
10000
5000
0
#
LPS + CC LPP IN
LPS + CE LPP IN
LPS + Free CAT IN
LPS Control
Control
c.
Catalase Activity in TS (U/mg total protein)
400
300
200
100
0
LPS + CC LPP IN
LPS + CE LPP IN
LPS + Free CAT IN
LPS Control
Control
d.
Catalase Activity in BALF (U/mL)
100
80
60
40
20
0
#
LPS + CC LPP IN
LPS + CE LPP IN
LPS + Free CAT IN
LPS Control
Control
e.
IL-6 in TS (pg/mg total protein)
20000
15000
10000
5000
0
#
LPS + CC LPP IN
LPS + CE LPP IN
LPS + Free CAT IN
LPS Control
Control
f.
IL-6 in BALF (pg/mL)
15000
10000
5000
0
LPS + CC LPP IN
LPS + CE LPP IN
LPS + Free CAT IN
LPS Control
Control

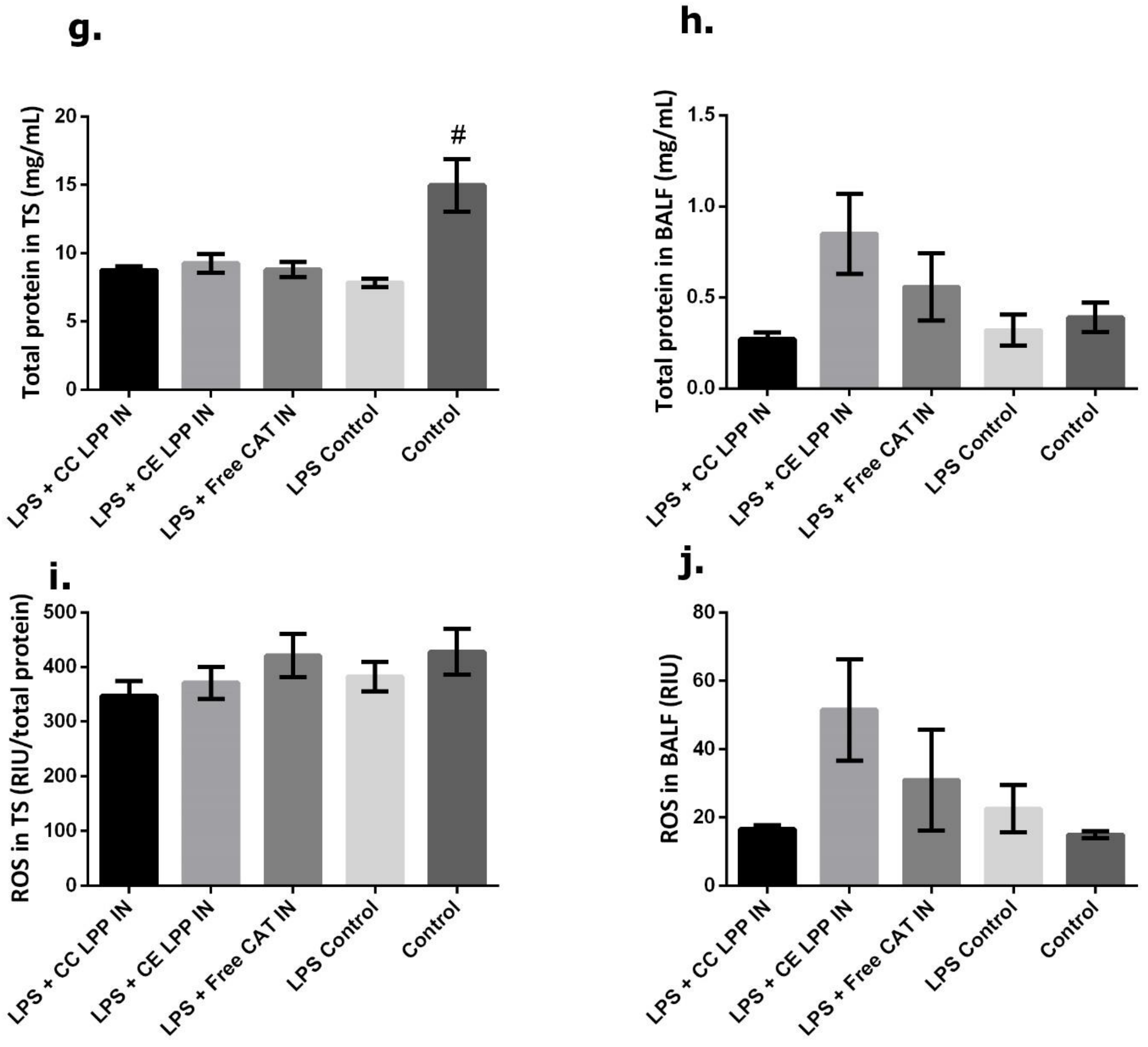

Fig. 5.12. Levels of tumor necrosis factor-alpha (a, b), catalase activity (c, d), interleukin-6 (e, f), total protein (g, h) and reactive oxygen species (i, j) (in lung tissue supernatants (TS) and bronchoalveolar lavage fluid (BALF), respectively) after intranasal (IN) dosing. Data presented as mean ± SEM (n=8). #p<0.05 versus LPS control.

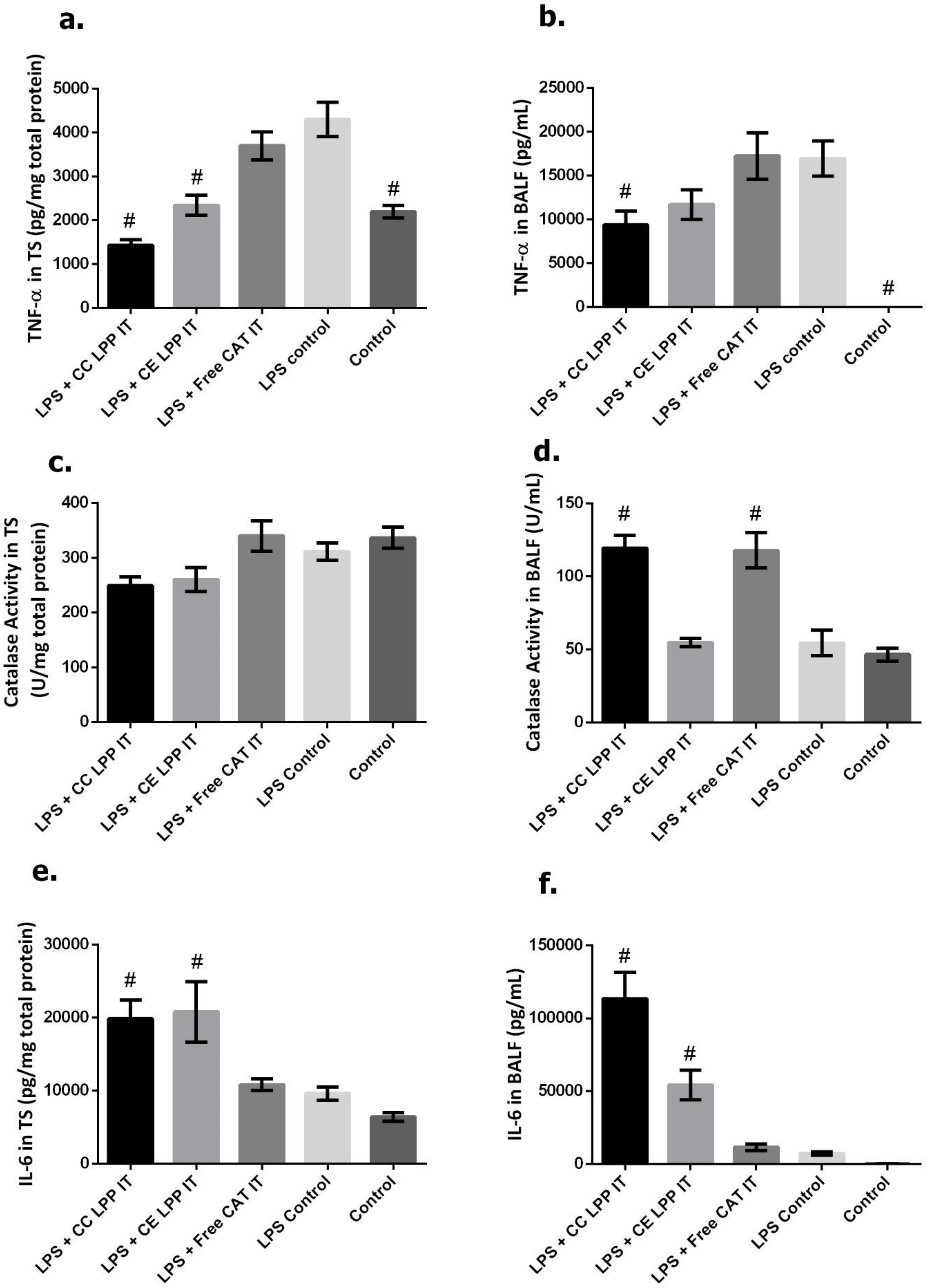
a.
TNF-α in TS (pg/mg total protein)
5000
4000
3000
2000
1000
0
#
#
#
LPS + CC LPP IT
LPS + CE LPP IT
LPS + Free CAT IT
LPS control
Control
b.
TNF-α in BALF (pg/mL)
25000
20000
15000
10000
5000
0
#
#
LPS + CC LPP IT
LPS + CE LPP IT
LPS + Free CAT IT
LPS control
Control
c.
Catalase Activity in TS (U/mg total protein)
400
300
200
100
0
LPS + CC LPP IT
LPS + CE LPP IT
LPS + Free CAT IT
LPS Control
Control
d.
Catalase Activity in BALF (U/mL)
150
100
50
0
#
#
LPS + CC LPP IT
LPS + CE LPP IT
LPS + Free CAT IT
LPS Control
Control
e.
IL-6 in TS (pg/mg total protein)
30000
20000
10000
0
#
#
LPS + CC LPP IT
LPS + CE LPP IT
LPS + Free CAT IT
LPS Control
Control
f.
IL-6 in BALF (pg/mL)
150000
100000
50000
0
#
#
LPS + CC LPP IT
LPS + CE LPP IT
LPS + Free CAT IT
LPS Control
Control

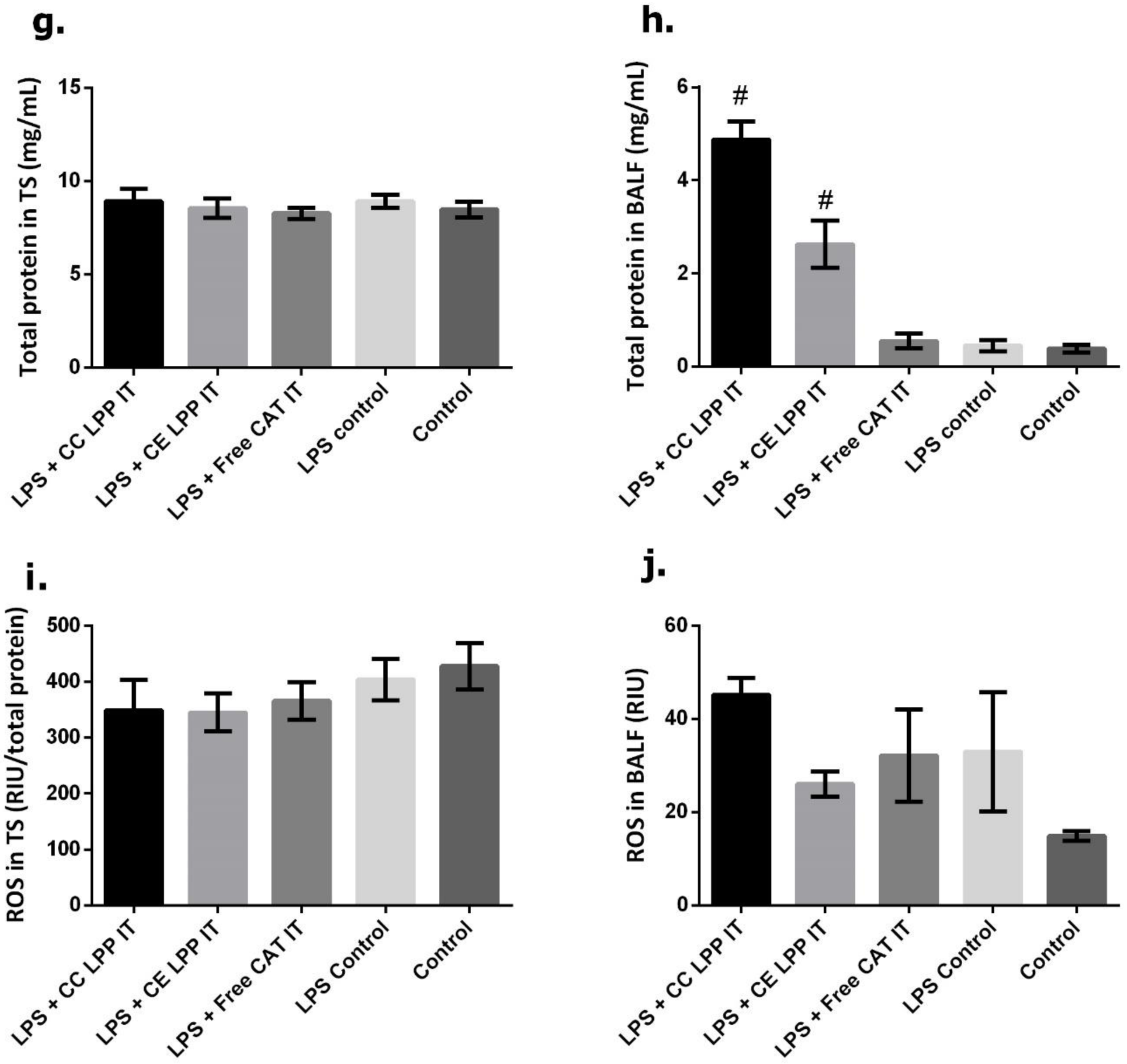

Fig. 5.13. Levels of tumor necrosis factor-alpha (a, b), catalase activity (c, d), interleukin-6 (e, f), total protein (g, h) and reactive oxygen species (i, j) (in lung tissue supernatants (TS) and bronchoalveolar lavage fluid (BALF), respectively) after intratracheal (IT) dosing. Data presented as mean ± SEM (n=8). #$p<0.05$ versus LPS control.

5.4 Discussion

Acute lung injury (ALI) is an acute inflammatory disorder which leads to significant morbidity and mortality in the critically ill patient population [44]. ALI is characterized by loss of alveolar-capillary membrane integrity, excessive neutrophil migration and release of pro-inflammatory cytokines. Lipopolysaccharide (LPS), a potent endotoxin derived from the outer membrane of gram-negative bacteria, has been used to induce ALI following intranasal, intratracheal or intraperitoneal administration [123-125]. LPS stimulates an inflammatory response of the lung by triggering pro-inflammatory cytokines such as interleukin-6 (IL-6), interleukin-1β and tumor necrosis factor-alpha (TNF-α). Many nanocarriers and proteins have been reported to successfully alleviate pulmonary inflammation that were induced by LPS in mice without serious toxicity [113, 125, 138]. However, in many such studies, the anti-inflammatory treatment took place a few minutes or hours prior to LPS challenge, which would count as a prophylactic measure. To better mimic a treatment of an established inflammation in our study, LPS was instilled first to induce inflammation, followed by the treatment by LPP formulations of the catalase protein. This could explain the toxicity and behavioral changes in mice of the ALI model after the LPP treatment, which was not observed in healthy mice. The inflamed lungs of such animals were more sensitive to the toxicity associated with the cationic lipid because the immune and inflammatory cells had already been recruited into the lung in response to LPS.

PEGylated catalase and recombinant human catalase have been reported to elicit therapeutic responses following intranasal administration in H1N1 influenza-induced pneumonia in mice [24, 97]. However, in our study, intranasal dosing of catalase formulations didn’t show any therapeutic benefit in the ALI mice model as the cargo protein did not successfully distribute into the inflamed lungs. This is in contrast to findings of the last chapter, where, the LPP formulations of catalase successfully distributed into the healthy lungs after intranasal administration. The animals' breathing plays a major role in the success of intranasal administration of liquid into the lung. Similar to prior findings, the ideal time for intranasal dosing in our experience is when the animal is taking long, deep breaths while waking up from anesthesia [102, 103]. Such deep breaths aid the inhalation of the liquid droplets into the lungs. The animals with inflamed lungs had shallow and labored breathing, which may have limited their ability to inhale the catalase formulations into the lung. Additionally, airway inflammation is associated with mucus hypersecretion and impaired mucociliary clearance, which may have caused the formulations to be trapped in the nasal mucosa [139]. Taken together, the insufficient pulmonary distribution of catalase formulations in ALI mice after intranasal dosing is most probably due to the denser mucosal barrier and shallower breathing of the animals with ALI than their healthy counterparts.

Cationic liposomes have been reported to be associated with dose-dependent toxicity and pulmonary inflammation in mice following intratracheal administration [108, 140]. Treatment with cationic nanocarriers are known to provoke pro-inflammatory cytokines such as IL-6, TNF-α and interferon-γ (IFN-γ) [141]. Commercially available cationic lipid DOTAP is a racemic mixture of two enantiomers. (R)-DOTAP has been investigated as an adjuvant in cancer treatment [142-144]. One such study found that (R)-DOTAP that was complexed with a peptide E7, was able to enhance tumor regression in a dose-dependent manner comparable to the group treated with the E7 complex with the racemic DOTAP. In comparison, treatment with (S)-DOTAP-E7 only delayed tumor progression. Although the underlying mechanism for this difference is unknown, (R)-DOTAP amplified the immune response by recruiting significantly higher tumor infiltrating lymphocytes and cytokine IFN-γ *in vivo* compared to the (S)-DOTAP group [142]. As these reports suggest the role of (R)-enantiomer of DOTAP in enhancing immunogenicity, one possible approach to overcome the toxicity of the current study could be to explore any potential advantage of the less immunogenic (S)-DOTAP in our LPP formulations.

One intriguing observation is that intratracheal dosing of LPP formulations changed the level of two proinflammatory cytokines, IL-6 and TNF-ɑ in opposite directions. LPP delivered catalase into the pulmonary cells to augment the natural antioxidant pool in the lungs, which could have resulted in the restoration of its redox balance and reduction of TNF-ɑ in the lungs. The upregulation of IL-6 may be attributed to toxicity associated with cationic lipids, as discussed above. However, IL-6 has also been investigated for its anti-inflammatory properties in tissue injury [145], which raises a question whether IL-6 levels were elevated to combat the inflammation in the lung. In order to clarify the underlying cause of IL-6 upregulation, another proinflammatory cytokine interleukin-1β and an anti-inflammatory cytokine interleukin-10 can be included in the future studies [121]. If we can monitor the levels of the proinflammatory and anti-inflammatory cytokines in response to LPP administration in inflamed lungs, we may be able to better understand the therapeutic benefit versus the toxicity of LPP.

One of the limitations of the current study in inflamed mice lungs was our inability to measure oxidative stress in the lungs. ROS and MDA levels did not increase in the LPS-induced ALI model, in contrast to several reports [101, 146]. Absence of any change in the tissue ROS levels after treatments with different LPP formulations was an unexpected result, which is inconsistent with our prior observations in healthy animals. Both the studies were performed on the same instrument (BioTek Synergy HT microplate reader) using the same settings (λ_{ex} = 485/20, λ_{em} = 528/20, optics = bottom, gain = 35, read speed = normal) and the viability of the probe was tested by adding 100 µM H_2O_2 to the tissue supernatants as a positive control, which yielded higher ROS levels. However, the ROS measurement with Carboxy H_2DCFDA is a semi-quantitative assay without a standard curve, which challenges the validity of comparing between the ROS data set from the healthy mice and the ROS data set from mice with inflamed lungs. In addition, the ROS probe may be an insensitive way of measuring oxidative stress in inflamed lungs [147]. Therefore, additional biomarkers such as myeloperoxidase (MPO, peroxidase enzyme expressed in neutrophils), superoxide dismutase (SOD, intracellular antioxidant enzyme), glutathione (GSH, endogenous antioxidant), nitric oxide (NO, reactive oxygen species) and total antioxidant status (TAS, an indirect measure of oxidative stress) can be included in future studies to measure oxidative stress [146].

Overall, intratracheal administration of lipopolysaccharide (LPS) induced lung inflammation in CD-1 mice. Intranasal administration to mice with ALI caused most of the formulation to be stuck in the nose and throat. In contrast, intratracheal administration delivered the fluorescently labeled catalase deep into the lung. Intratracheal dosing of LPP formulations significantly reduced TNF-α production in the inflamed lungs compared to free catalase solution, which highlighted the importance of LPP in delivering catalase into pulmonary cells to alleviate the oxidative stress associated with inflammation. However, intratracheal administration of LPP formulations elevated IL-6 in inflamed lungs, which may indicate toxicity associated with cationic lipids.

Chapter 6: Summary

Proteins are large biomolecules of great therapeutic potential. Intracellular delivery of proteins can augment the deficient activities of dysfunctional or poorly expressed innate proteins and therefore represents a promising strategy to treat the associated diseases. Moreover, proteins can be delivered into cells to counter several pathological developments such as inflammation, oxidative stress, neurodegeneration, and cancer cell growth. One major barrier of intracellular protein delivery is the translocation of the protein across the cellular membranes. Endocytosis provides an important pathway for protein nanocarriers to enter the cells across the plasma membrane. However, the cargo protein must then promptly escape from the endosomes to exert its cellular function, and to avoid degradation in the lysosome.

Previously, we reported a cationic lipid-coated magnesium phosphate nanoparticule (LPP) system for intracellular protein delivery. LPP consists of a shell of concentric cationic lipid bilayers, a core of magnesium phosphate nanoparticle (MgP NP) and the cargo protein, catalase, which is an antioxidant enzyme. The cationic surface of the LPP would first bind to the negatively charged cell surface to trigger endocytosis. Inside the endosome, the MgP NP would dissolve at the acidic pH to form a high-salt solution, which has a high osmotic pressure to cause water influx from cytosol. Consequently, the endosome would swell and destabilize to release the cargo protein into the cytosol. The intracellular delivery of catalase by LPP protected MCF-7 cells from lethal levels of exogenous H_2O_2 and lowered the ROS level in EA.hy926 cells. Such promising findings of LPP in cell cultures prompted us to further develop LPP and to evaluate its protein delivery in animals. Therefore, the objective of this dissertation was to develop LPP formulations suitable for *in vivo* applications and to evaluate their protein delivery efficiency in both healthy and diseased animals

The construction of LPP consists of three modules: 1) preparation of catalase-loaded liposomes including catalase-encapsulated liposomes (CE LP) and catalase-complexed liposomes (CC LP), 2) preparation of magnesium phosphate nanoparticles (MgP NP), and 3) coating of MgP NP with catalase-loaded liposomes. CE LP were prepared by thin-film hydration followed by extrusion through a 200 nm membrane. However, LPP prepared from CE LP suffered substantial loss of protein activity due to extrusion and carried a large diameter around 280 nm. As an alternative approach to prepare LPP, cationic liposomes were first extruded and then mixed with the negatively charged catalase to form CC LP.

Cationic liposomes were prepared by a hand-held extruder, a pressured LIPEX extruder and a microfluidic mixing instrument and their colloidal properties were compared. LIPEX extruder was chosen for preparing cationic liposomes in the following studies because it conveniently yielded small cationic liposomes (~70 nm in diameter) in sufficient scale for animal studies. Compared to encapsulation (CE LP), the complexation strategy yielded catalase-complexed liposomes (CC LP) of significantly lower size (around 140 nm) and preserved all the protein activity by minimizing the mechanical stress exerted on the protein during extrusion. Glucose was used for isotonicity adjustment in the LPP formulations of catalase for animal studies because it preserved the colloidal properties of the liposomes.

Transmission electron microscopy (TEM) was used to examine the morphology and the particle size distribution of different components of LPP. The TEM images of LPP and the formulation precursors were consistent with the dynamic light scattering measurements and confirmed the location of the protein and the presence of a MgP NP core in the final LPP formulations. Furthermore, TEM was also used to examine changes in the morphology of LPP in response to acidic pH. The TEM images of LPP formulations that had been exposed to acidic pH showed deformed and scattered structures, in contrast to their tight spherical structures at pH 7.4. The deformation of LPP in acidic pH supports the proposed mechanism of pH-triggered release of catalase, where the MgP NP core dissolves at acidic pH into a solution of high osmotic pressure, which consequently swells, deforms, and in many cases lyses the LPP formulation.

LPP was administered by three different routes to CD-1 mice, where the lung was chosen as the target organ because many diseases such as chronic obstructive pulmonary disease (COPD), acute lung injury (ALI), acute respiratory distress syndrome (ARDS), asthma, pneumonia and bronchitis involve oxidative stress of pulmonary cells, which can be alleviated by catalase, an important antioxidant enzyme. Before evaluation in a lung disease model, LPP was administered either intravenously or intranasally to healthy animals to evaluate its protein delivery efficiency and to determine the appropriate route for intrapulmonary delivery of LPP formulations. Catalase that was fluorescently labeled with Cyanine 7.5 were loaded into LPP formulations (CC LPP and CE LPP) to study their biodistribution in mice. The fluorescently labeled catalase distributed substantially into the lung after intranasal administration of CC LPP, whereas intravenous administration of CC LPP caused catalase distribution mainly into the liver.

The functionality of the intrapulmonarily delivered catalase was assessed using two markers: 1) the increase of catalase activity in the lungs after the administration, and 2) the decrease of reactive oxygen species (ROS) level as a measure of whether the delivered cargo catalase can protect the lung tissue from oxidative stress. Following intranasal administration, the complexed catalase formulation (CC LPP), which was smaller and which better preserved catalase activity than CE LPP, showed higher catalase activity and lower ROS levels in the lung compared to the catalase-encapsulated formulation (CE LPP). Both the LPP formulations yielded higher pulmonary catalase activity and lower ROS levels than the liposomal catalase (L-CAT without the MgP NP core) and the free catalase solution after intranasal dosing. These findings indicate the importance of the LPP construct with the MgP NP core in delivering protein into the pulmonary cells. Intravenous dosing of LPP formulations of catalase caused no substantial changes in the catalase activities nor in the ROS levels in the lung compared to untreated baseline levels. Based on these results, intranasal administration but not intravenous administration was selected for further studies on the intrapulmonary delivery of LPP.

Acute lung injury (ALI) was induced in CD-1 mice by intratracheal administration of 3 mg/Kg lipopolysaccharide (LPS), a bacterial endotoxin. The LPP formulations with Cy7.5-labeled catalase were administered either intratracheally or intranasally 30 minutes after LPS-imposed injury, followed by fluorescence imaging to identify the better route for protein delivery into inflamed lungs. In contrast to healthy mice, intranasal administration to mice with ALI caused most of the formulation to be stuck in the nose and throat of the animal. Intratracheal dosing delivered the fluorescently labeled catalase deep into the lung and was more suitable for intrapulmonary delivery in mice with ALI.

Intratracheal intubation of LPS induced acute lung inflammation in CD-1 mice as marked by the increase of pro-inflammatory cytokines TNF-α and IL-6. Both the markers showed no substantial changes following intranasal dosing of LPP formulations containing catalase, which is consistent with our finding that intranasally administered LPP formulations failed to distribute into the inflamed lungs. Intratracheal administration of the LPP formulations significantly reduced TNF-α production in the lungs of LPS-challenged animals when compared to free catalase solution. This emphasizes the importance of LPP in delivering catalase into the pulmonary cells to augment the natural antioxidant activities in the lungs, which serves to scavenge excessive ROS and to restore the redox balance in disease conditions. However, intratracheal dosing of LPP formulations elevated IL-6 in inflamed lungs, which may indicate toxicity associated with cationic lipids.

Rapid clearance from the systemic circulation after intravenous administration and toxicity in inflamed lungs after intratracheal administration were the two major limitations for intrapulmonary protein delivery using LPP. Future work could include monitoring LPP’s stability in serum using forster resonance energy transfer (FRET) and attempting to prolong LPP’s circulation in blood by coating its surface with polyethylene glycol (PEG). LPP's surface can also be coated with ligands that bind to platelet-endothelial cell adhesion molecule (PECAM), in order to target the pulmonary endothelium after intravenous administration. To address LPP's toxicity in inflamed lungs, future studies could explore the potential advantage of the less immunogenic enantiomer of the cationic lipid, (S)-DOTAP in the LPP formulations.

In conclusion, a novel protein nanocarrier LPP loaded with catalase (CC LPP and CE LPP) was prepared and optimized for *in vivo* application. Characterizations by dynamic light scattering and transmission electron microscopy confirmed that the strategy of complexing cationic LP with catalase yielded smaller CC LPP than the encapsulation technique (CE LPP). Although both the LPP formulations of catalase demonstrated promising antioxidant effects in CD-1 mice with healthy and inflamed lungs, CC LPP showed better distribution into the lung tissue because of its smaller size.

REFERENCES

1. Leader, B., Q.J. Baca, and D.E. Golan, *Protein therapeutics: a summary and pharmacological classification.* Nat Rev Drug Discov, 2008. **7**(1): p. 21-39.
2. Nayerossadat, N., T. Maedeh, and P.A. Ali, *Viral and nonviral delivery systems for gene delivery.* Adv Biomed Res, 2012. **1**.
3. Lee, Y.W., et al., *Protein Delivery into the Cell Cytosol using Non-Viral Nanocarriers.* Theranostics, 2019. **9**(11): p. 3280-92.
4. Wadia, J.S. and S.F. Dowdy, *Transmembrane delivery of protein and peptide drugs by TAT-mediated transduction in the treatment of cancer.* Adv Drug Deliv Rev, 2005. **57**(4): p. 579-96.
5. Patterson, H., et al., *Protein kinase inhibitors in the treatment of inflammatory and autoimmune diseases.* Clin Exp Immunol, 2014. **176**(1): p. 1-10.
6. Hu, Y.B., et al., *The endosomal-lysosomal system: from acidification and cargo sorting to neurodegeneration.* Transl Neurodegener, 2015. **4**.
7. Leroux, J.C., *pH-responsive carriers for enhancing the cytoplasmic delivery of macromolecular drugs.* Advanced Drug Delivery Reviews, 2004. **56**(7): p. 925-926.
8. Bareford, L.M. and P.W. Swaan, *Endocytic mechanisms for targeted drug delivery.* Adv Drug Deliv Rev, 2007. **59**(8): p. 748-58.
9. Erazo-Oliveras, A., et al., *Improving the Endosomal Escape of Cell-Penetrating Peptides and Their Cargos: Strategies and Challenges*, in *Pharmaceuticals (Basel)*. 2012. p. 1177-209.
10. Fu, A., et al., *Promises and Pitfalls of Intracellular Delivery of Proteins.* 2014.
11. Bamrungsap, S., et al., *Nanotechnology in therapeutics: a focus on nanoparticles as a drug delivery system.* Nanomedicine (Lond), 2012. **7**(8): p. 1253-71.
12. Du, J., et al., *Synthetic nanocarriers for intracellular protein delivery.* Curr Drug Metab, 2012. **13**(1): p. 82-92.
13. Bale, S.S., et al., *Nanoparticle-mediated cytoplasmic delivery of proteins to target cellular machinery.* ACS Nano, 2010. **4**(3): p. 1493-500.
14. Wang, Y., et al., *Mesoporous silica nanoparticles in drug delivery and biomedical applications.* Nanomedicine, 2015. **11**(2): p. 313-27.
15. Lin, Y.H., et al., *Approach To Deliver Two Antioxidant Enzymes with Mesoporous Silica Nanoparticles into Cells.* ACS Appl Mater Interfaces, 2016. **8**(28): p. 17944-54.
16. Yang, J., et al., *Membrane Fusion Mediated Intracellular Delivery of Lipid Bilayer Coated Mesoporous Silica Nanoparticles.* Adv Healthc Mater, 2017. **6**(20).
17. Niu, Y., et al., *Understanding the contribution of surface roughness and hydrophobic modification of silica nanoparticles to enhanced therapeutic protein delivery.* 2015.

18. Ghosh, P., et al., *Intracellular delivery of a membrane-impermeable enzyme in active form using functionalized gold nanoparticles.* J Am Chem Soc, 2010. **132**(8): p. 2642-5.
19. Mout, R., et al., *Programmed Self-Assembly of Hierarchical Nanostructures through Protein-Nanoparticle Coengineering.* ACS Nano, 2017. **11**(4): p. 3456-3462.
20. Lee, K., et al., *Nanoparticle delivery of Cas9 ribonucleoprotein and donor DNA in vivo induces homology-directed DNA repair.* Nature Biomedical Engineering, 2017. **1**(11): p. 889.
21. Wen, N., et al., *Glucose-responsive zwitterionic dialdehyde starch-based micelles with potential anti-phagocytic behavior for insulin delivery.* The Chemical Engineering Journal, 2017. **335**.
22. Gao, G.H., et al., *The use of pH-sensitive positively charged polymeric micelles for protein delivery.* Biomaterials, 2012. **33**(35): p. 9157-64.
23. González-Toro, D.C., et al., *Concurrent Binding and Delivery of Proteins and Lipophilic Small Molecules Using Polymeric Nanogels.* 2012.
24. Shi, X., et al., *PEGylated human catalase elicits potent therapeutic effects on H1N1 influenza-induced pneumonia in mice.* Appl Microbiol Biotechnol, 2013. **97**(23): p. 10025-33.
25. Barman, S.R., et al., *Dendrimer as a multifunctional capping agent for metal nanoparticles for use in bioimaging, drug delivery and sensor applications.* 2018.
26. Lv, J., et al., *Fluoropolymers for intracellular and in vivo protein delivery.* Biomaterials, 2018. **182**: p. 167-175.
27. Zhang, Z., et al., *The fluorination effect of fluoroamphiphiles in cytosolic protein delivery.* Nature Communications, 2018. **9**(1): p. 1377.
28. Chang, H., et al., *Rational Design of a Polymer with Robust Efficacy for Intracellular Protein and Peptide Delivery.* Nano Lett, 2017. **17**(3): p. 1678-1684.
29. Sarker, S.R., R. Hokama, and S. Takeoka, *Intracellular Delivery of Universal Proteins Using a Lysine Headgroup Containing Cationic Liposomes: Deciphering the Uptake Mechanism.* 2013.
30. Kim, S.K., M.B. Foote, and L. Huang, *The targeted intracellular delivery of cytochrome C protein to tumors using lipid-apolipoprotein nanoparticles.* Biomaterials, 2012. **33**(15): p. 3959-66.
31. Robson, A.L., et al., *Advantages and Limitations of Current Imaging Techniques for Characterizing Liposome Morphology.* Front Pharmacol, 2018. **9**.
32. Yamaguchi, K., M. Inoue, and N. Goshima, *Efficient Protein Transduction Method Using Cationic Peptides and Lipids.* J Biomed Biotechnol, 2011. **2011**.
33. Chatin, B., et al., *Liposome-based Formulation for Intracellular Delivery of Functional Proteins.* Molecular Therapy - Nucleic Acids, 2015. **4**.
34. Roessl, U., et al., *Characterization of a Laboratory-Scale Container for Freezing Protein Solutions with Detailed Evaluation of a Freezing Process Simulation.* Journal of Pharmaceutical Sciences, 2014. **103**(2): p. 417-426.

35. Yoon, G., J.W. Park, and I.-S. Yoon, *Solid lipid nanoparticles (SLNs) and nanostructured lipid carriers (NLCs): recent advances in drug delivery.* Journal of Pharmaceutical Investigation, 2013. **43**(5): p. 353-362.
36. Ghasemiyeh, P. and S. Mohammadi-Samani, *Solid lipid nanoparticles and nanostructured lipid carriers as novel drug delivery systems: applications, advantages and disadvantages.* Res Pharm Sci, 2018. **13**(4): p. 288-303.
37. Almeida, A.J., S. Runge, and R.H. Muller, *Peptide-loaded solid lipid nanoparticles (SLN): Influence of production parameters*. 1997. p. 255-265.
38. Christophersen, P.C., et al., *Solid lipid particles for oral delivery of peptide and protein drugs I--elucidating the release mechanism of lysozyme during lipolysis.* Eur J Pharm Biopharm, 2013. **85**(3 Pt A): p. 473-80.
39. Fang, Y., et al., *Lipid-Coated, pH-Sensitive Magnesium Phosphate Particles for Intracellular Protein Delivery.* Pharm Res, 2019. **36**(6): p. 81.
40. Scibior, D. and H. Czeczot, *[Catalase: structure, properties, functions].* Postepy Hig Med Dosw (Online), 2006. **60**: p. 170-80.
41. Li, J., et al., *Biodegradable calcium phosphate nanoparticle with lipid coating for systemic siRNA delivery.* J Control Release, 2010. **142**(3): p. 416-21.
42. Meduri, G.U., et al., *Inflammatory cytokines in the BAL of patients with ARDS. Persistent elevation over time predicts poor outcome.* Chest, 1995. **108**(5): p. 1303-14.
43. Moldoveanu, B., et al., *Inflammatory mechanisms in the lung.* J Inflamm Res, 2009. **2**: p. 1-11.
44. Johnson, E.R. and M.A. Matthay, *Acute Lung Injury: Epidemiology, Pathogenesis, and Treatment.* J Aerosol Med Pulm Drug Deliv, 2010. **23**(4): p. 243-52.
45. Odajima, N., et al., *The Role of Catalase in Pulmonary Fibrosis.* Respir Res, 2010. **11**(1): p. 183.
46. Kellner, M., et al., *ROS Signaling in the Pathogenesis of Acute Lung Injury (ALI) and Acute Respiratory Distress Syndrome (ARDS).* Adv Exp Med Biol, 2017. **967**: p. 105-137.
47. Galvao, A.M., et al., *Cationic liposomes containing antioxidants reduces pulmonary injury in experimental model of sepsis: Liposomes antioxidants reduces pulmonary damage.* Respir Physiol Neurobiol, 2016. **231**: p. 55-62.
48. Rosenblum, D., et al., *Progress and challenges towards targeted delivery of cancer therapeutics.* Nature Communications, 2018. **9**(1): p. 1410.
49. Azzopardi, E.A., E.L. Ferguson, and D.W. Thomas, *The enhanced permeability retention effect: a new paradigm for drug targeting in infection.* J Antimicrob Chemother, 2013. **68**(2): p. 257-74.
50. Barron, L.G., L.S. Uyechi, and F.C. Szoka, Jr., *Cationic lipids are essential for gene delivery mediated by intravenous administration of lipoplexes.* Gene Ther, 1999. **6**(6): p. 1179-83.
51. Uyechi, L.S., et al., *Mechanism of lipoplex gene delivery in mouse lung: binding and internalization of fluorescent lipid and DNA components.* Gene Ther, 2001. **8**(11): p. 828-36.

52. Zhang, J., et al., *Chapter 13 - Nanosuspension drug delivery system: preparation, characterization, postproduction processing, dosage form, and application*, in *Nanostructures for Drug Delivery*. 2017, Elsevier Inc. p. 413-443.
53. Murgia, X., C. De Souza Carvalho, and C.M. Lehr, *Overcoming the pulmonary barrier: New insights to improve the efficiency of inhaled therapeutics.* European Journal of Nanomedicine, 2014. **6**(3): p. 157-169.
54. Yang, W., J.I. Peters, and R.O. Williams, 3rd, *Inhaled nanoparticles--a current review.* Int J Pharm, 2008. **356**(1-2): p. 239-47.
55. Huang, Y.Y. and C.H. Wang, *Pulmonary delivery of insulin by liposomal carriers.* J Control Release, 2006. **113**(1): p. 9-14.
56. Mansour, H.M., Y.S. Rhee, and X. Wu, *Nanomedicine in pulmonary delivery*, in *Int J Nanomedicine*. 2009. p. 299-319.
57. Gumbleton, M., *Caveolae as potential macromolecule trafficking compartments within alveolar epithelium.* Adv Drug Deliv Rev, 2001. **49**(3): p. 281-300.
58. Patel, V.R. and Y.K. Agrawal, *Nanosuspension: An approach to enhance solubility of drugs.* J Adv Pharm Technol Res, 2011. **2**(2): p. 81-7.
59. Gustafson, H.H., et al., *Nanoparticle Uptake: The Phagocyte Problem.* Nano Today, 2015. **10**(4): p. 487-510.
60. Byron, P.R., *Physicochemical effects on lung disposition of pharmaceutical aerosols.* Aerosol Science and Technology, 1993. **18**(3): p. 223-229.
61. Stefano, S. and C. Paolo, *Stealth Properties to Improve Therapeutic Efficacy of Drug Nanocarriers.* Journal of Drug Delivery, 2013: p. 87.
62. Suk, J.S., et al., *PEGylation as a strategy for improving nanoparticle-based drug and gene delivery.* Adv Drug Deliv Rev, 2016. **99**(Pt A): p. 28-51.
63. Miller, C.R., et al., *Liposome-cell interactions in vitro: effect of liposome surface charge on the binding and endocytosis of conventional and sterically stabilized liposomes.* Biochemistry, 1998. **37**(37): p. 12875-83.
64. Lin, P.J., et al., *Influence of cationic lipid composition on uptake and intracellular processing of lipid nanoparticle formulations of siRNA.* Nanomedicine, 2013. **9**(2): p. 233-46.
65. Simberg, D., et al., *DOTAP (and other cationic lipids): chemistry, biophysics, and transfection.* Crit Rev Ther Drug Carrier Syst, 2004. **21**(4): p. 257-317.
66. Sokolova, V. and M. Epple, *Inorganic nanoparticles as carriers of nucleic acids into cells.* Angew Chem Int Ed Engl, 2008. **47**(8): p. 1382-95.
67. Paital, S. and N. Dahotre, *Calcium phosphate coatings for bio-implant applications: Materials, performance factors, and methodologies.* Material Science and Engineering R Reports, 2009. **66**(Issues 1–3): p. 1–70.
68. Li, J., et al., *Biodegradable Calcium Phosphate Nanoparticle with Lipid Coating for Systemic siRNA Delivery.* J Control Release, 2010. **142**(3): p. 416-21.
69. Ariyanto, E., et al., *Effect of initial solution pH on solubility and morphology of struvice crystals.* 2012.
70. Chowdhury, E.H. and T. Akaike, *Fibronectin-coated nano-precipitates of calcium–magnesium phosphate for integrin-targeted gene delivery.* Journal of Controlled Release, 2006. **116**(2): p. e68–e69.

71. Kawamata, H. and G. Manfredi, *Mitochondrial dysfunction and intracellular calcium dysregulation in ALS.* Mech Ageing Dev, 2010. **131**(7-8): p. 517-26.
72. Gunther, T., *Concentration, compartmentation and metabolic function of intracellular free Mg2+.* Magnes Res, 2006. **19**(4): p. 225-36.
73. Bhakta, G., A. Shrivastava, and A. Maitra, *Magnesium phosphate nanoparticles can be efficiently used in vitro and in vivo as non-viral vectors for targeted gene delivery.* J Biomed Nanotechnol, 2009. **5**(1): p. 106-14.
74. Tamimi, F., et al., *Biocompatibility of magnesium phosphate minerals and their stability under physiological conditions.* Acta Biomater, 2011. **7**(6): p. 2678-85.
75. Vossman, *File:Catalase Structure.png - Wikimedia Commons*, C. Structure, Editor. 1 March 2009: Wikipedia.
76. Shaw, K.L., et al., *The effect of net charge on the solubility, activity, and stability of ribonuclease Sa.* Protein Sci, 2001. **10**(6): p. 1206-15.
77. Moore, T.L., et al., *Nanoparticle colloidal stability in cell culture media and impact on cellular interactions.* Chem Soc Rev, 2015. **44**(17): p. 6287-305.
78. Yeeprae, W., et al., *Physicochemical and pharmacokinetic characteristics of cationic liposomes.* Pharmazie, 2006. **61**(2): p. 102-5.
79. De Jong, W.H. and P.J. Borm, *Drug delivery and nanoparticles: Applications and hazards.* Int J Nanomedicine, 2008. **3**(2): p. 133-49.
80. Naidu, P., *Catalase-loaded liposomal magnesium phosphate nanoparticles for intracellular protein delivery*. 2016, University of the Pacific: ProQuest Dissertations Publishing.
81. Briuglia, M.L., et al., *Influence of cholesterol on liposome stability and on in vitro drug release.* Drug Deliv Transl Res, 2015. **5**(3): p. 231-42.
82. Kastner, E., et al., *High-throughput manufacturing of size-tuned liposomes by a new microfluidics method using enhanced statistical tools for characterization.* International Journal of Pharmaceutics, 2014. **477**(1-2): p. 361-368.
83. Bartlett, G.R., *Phosphorus assay in column chromatography.* J Biol Chem, 1959. **234**(3): p. 466-8.
84. Zheng, Y., et al., *Fliposomes: trans-2-aminocyclohexanol-based amphiphiles as pH-sensitive conformational switches of liposome membrane – a structure-activity relationship study.* Chemistry and Physics of Lipids, 2018. **210**: p. 129-141.
85. Shyh-Dar, L., L. Song, and H. Leaf, *Lipoplex and LPD Nanoparticles for In Vivo Gene Delivery.* CSH Protoc, 2006. **2006**(1).
86. Palmer, L.R., et al., *Transfection properties of stabilized plasmid-lipid particles containing cationic PEG lipids.* Biochim Biophys Acta, 2003. **1611**(1-2): p. 204-16.
87. Li, S., et al., *Characterization of cationic lipid-protamine-DNA (LPD) complexes for intravenous gene delivery.* Gene Ther, 1998. **5**(7): p. 930-7.
88. Yang, Y., et al., *Systemic delivery of siRNA via LCP nanoparticle efficiently inhibits lung metastasis.* Mol Ther, 2012. **20**(3): p. 609-15.
89. Tsumoto, K., et al., *Effects of salts on protein-surface interactions: applications for column chromatography.* J Pharm Sci, 2007. **96**(7): p. 1677-90.

90. Reimer, L. and H. Kohl, *Transmission electron microscopy: physics of image formation and microanalysis*. 1984.
91. Baxa, U., *Imaging of Liposomes by Transmission Electron Microscopy.* Methods Mol Biol, 2018. **1682**: p. 73-88.
92. Barreto-Vieira, D.F. and O.M. Barth, *Negative and Positive Staining in Transmission Electron Microscopy for Virus Diagnosis*, in *Microbiology in Agriculture and Human Health*. 2015.
93. Ellis, E.A. and L. Cohen-Gould, *Recognizing and Preventing Artifacts in Microscopy: A Roundtable Discussion | Microscopy and Microanalysis | Cambridge Core.* Proceedings of Microscopy and Microanalysis, 2016. **22**.
94. Asadabad, M.A. and M.J. Eskandari, *Transmission Electron Microscopy as Best Technique for Characterization in Nanotechnology.* Synthesis and Reactivity in Inorganic, Metal-Organic, and Nano-Metal Chemistry, 2014. **45**(3).
95. Liu, M., et al., *Real-time visualization of clustering and intracellular transport of gold nanoparticles by correlative imaging.* Nature Communications, 2017. **8**: p. 15646.
96. Liu, B.R., et al., *Endocytic Trafficking of Nanoparticles Delivered by Cell-penetrating Peptides Comprised of Nona-arginine and a Penetration Accelerating Sequence.* PLoS One, 2013. **8**(6).
97. Shi, X.L., et al., *Therapeutic effect of recombinant human catalase on H1N1 influenza-induced pneumonia in mice.* Inflammation, 2010. **33**(3): p. 166-72.
98. Murdoch, J.R. and C.M. Lloyd, *Chronic inflammation and asthma*, in *Mutat Res*. 2010. p. 24-39.
99. Yeeprae, W., et al., *Physicochemical and pharmacokinetic characteristics of cationic liposomes.* 2006.
100. Diehl, K.H., et al., *A good practice guide to the administration of substances and removal of blood, including routes and volumes.* J Appl Toxicol, 2001. **21**(1): p. 15-23.
101. Kumari, A., et al., *Intranasal curcumin ameliorates lipopolysaccharide-induced acute lung injury in mice.* Inflammation, 2015. **38**(3): p. 1103-12.
102. Southam, D.S., et al., *Distribution of intranasal instillations in mice: effects of volume, time, body position, and anesthesia.* Am J Physiol Lung Cell Mol Physiol, 2002. **282**(4): p. L833-9.
103. Miller, M.A., et al., *Visualization of murine intranasal dosing efficiency using luminescent Francisella tularensis: effect of instillation volume and form of anesthesia.* PLoS One, 2012. **7**(2): p. e31359.
104. Egger, C., et al., *Administration of Bleomycin via the Oropharyngeal Aspiration Route Leads to Sustained Lung Fibrosis in Mice and Rats as Quantified by UTE-MRI and Histology.* PLoS One, 2013. **8**(5).
105. Li, H., et al., *In vivo near infrared fluorescence imaging and dynamic quantification of pancreatic metastatic tumors using folic acid conjugated biodegradable mesoporous silica nanoparticles.* Nanomedicine, 2018. **14**(6): p. 1867-1877.

106. Su, D., *Rational design, characterization and in vivo studies of antibody mimics against HER2 - Dissertations & Theses @ University of the Pacific - ProQuest*. 2015, University of the Pacific.
107. Heidari, R., et al., *Sulfasalazine-induced renal injury in rats and the protective role of thiol-reductants.* Ren Fail, 2016. **38**(1): p. 137-41.
108. Dokka, S., et al., *Oxygen radical-mediated pulmonary toxicity induced by some cationic liposomes.* Pharm Res, 2000. **17**(5): p. 521-5.
109. Zhang, Y. and T.J. Anchordoquy, *The role of lipid charge density in the serum stability of cationic lipid/DNA complexes.* Biochim Biophys Acta, 2004. **1663**(1-2): p. 143-57.
110. Zahednezhad, F., et al., *Liposome and immune system interplay: Challenges and potentials.* J Control Release, 2019. **305**: p. 194-209.
111. Swider, E., et al., *Förster Resonance Energy Transfer-Based Stability Assessment of PLGA Nanoparticles in Vitro and in Vivo.* ACS Appl Bio Mater, 2019. **2**(3): p. 1131-40.
112. Muppidi, K., et al., *PEGylated Liposome Encapsulation Increases the Lung Tissue Concentration of Vancomycin* ▿, in *Antimicrob Agents Chemother*. 2011. p. 4537-42.
113. Howard, M.D., et al., *Endothelial targeting of liposomes encapsulating SOD/Catalase mimetic EUK-134 alleviates acute pulmonary inflammation.* J Control Release, 2014. **177**: p. 34-41.
114. Lertkiatmongkol, P., et al., *Endothelial functions of PECAM-1 (CD31).* Curr Opin Hematol, 2016. **23**(3): p. 253-9.
115. Donovan, J. and P. Brown, *Parenteral injections.* Current Protocols In Immunology, 2006. **Chapter 1**: p. 1.6-1.6.
116. Lai, S.K., Y.Y. Wang, and J. Hanes, *Mucus-penetrating nanoparticles for drug and gene delivery to mucosal tissues.* Adv Drug Deliv Rev, 2009. **61**(2): p. 158-71.
117. Liu, M., et al., *Developments of mucus penetrating nanoparticles.* Asian Journal of Pharmaceutical Sciences, 2015. **10**(4): p. 275-282.
118. Nikoletta, R., K. Antonia, and G.K. Nikolaos, *Inflammation and Immune Response in COPD: Where Do We Stand?* Mediators of Inflammation, 2013: p. 296.
119. Brower, R.G., et al., *Ventilation with lower tidal volumes as compared with traditional tidal volumes for acute lung injury and the acute respiratory distress syndrome.* N Engl J Med, 2000. **342**(18): p. 1301-8.
120. Maeshima, N. and R.C. Fernandez, *Recognition of lipid A variants by the TLR4-MD-2 receptor complex.* Front Cell Infect Microbiol, 2013. **3**.
121. An, X., et al., *Protective effect of oxytocin on LPS-induced acute lung injury in mice.* Scientific Reports, 2019. **9**(1): p. 2836.
122. Chow, C.W., et al., *Oxidative stress and acute lung injury.* Am J Respir Cell Mol Biol, 2003. **29**(4): p. 427-31.
123. Kapoor, K., et al., *PARP inhibitor, olaparib ameliorates acute lung and kidney injury upon intratracheal administration of LPS in mice.* Mol Cell Biochem, 2015. **400**(1-2): p. 153-62.

124. Liang, D., et al., *Shikonin exerts anti-inflammatory effects in a murine model of lipopolysaccharide-induced acute lung injury by inhibiting the nuclear factor-kappaB signaling pathway.* Int Immunopharmacol, 2013. **16**(4): p. 475-80.
125. An, X., et al., *Protective effect of oxytocin on LPS-induced acute lung injury in mice.* Sci Rep, 2019. **9**(1): p. 2836.
126. Ghorani, V., et al., *Experimental animal models for COPD: a methodological review.* Tob Induc Dis, 2017. **15**: p. 25.
127. Hamid, U., et al., *Aspirin reduces lipopolysaccharide-induced pulmonary inflammation in human models of ARDS.* Thorax, 2017. **72**(11): p. 971-980.
128. Tanaka, T., M. Narazaki, and T. Kishimoto, *IL-6 in Inflammation, Immunity, and Disease.* Cold Spring Harb Perspect Biol, 2014. **6**(10).
129. Idriss, H.T. and J.H. Naismith, *TNF alpha and the TNF receptor superfamily: structure-function relationship(s).* Microsc Res Tech, 2000. **50**(3): p. 184-95.
130. Ray, P.D., B.W. Huang, and Y. Tsuji, *Reactive oxygen species (ROS) homeostasis and redox regulation in cellular signaling.* Cell Signal, 2012. **24**(5): p. 981-90.
131. Ayala, A., M.F. Munoz, and S. Arguelles, *Lipid peroxidation: production, metabolism, and signaling mechanisms of malondialdehyde and 4-hydroxy-2-nonenal.* Oxid Med Cell Longev, 2014. **2014**: p. 360438.
132. Limjunyawong, N., J. Mock, and W. Mitzner, *Instillation and Fixation Methods Useful in Mouse Lung Cancer Research.* J Vis Exp, 2015(102): p. e52964.
133. Hasegawa-Baba, Y., et al., *Intratracheal Instillation Methods and the Distribution of Administered Material in the Lung of the Rat*, in *J Toxicol Pathol*. 2014. p. 197-204.
134. Sun, F., G. Xiao, and Z. Qu, *Murine Bronchoalveolar Lavage.* Bio Protoc, 2017. **7**(10).
135. Card, J.W., et al., *Gender differences in murine airway responsiveness and lipopolysaccharide-induced inflammation.* J Immunol, 2006. **177**(1): p. 621-30.
136. Speyer, C.L., et al., *Regulatory effects of estrogen on acute lung inflammation in mice.* Am J Physiol Cell Physiol, 2005. **288**(4): p. C881-90.
137. Namburi, R.P., V. Kancherla, and A.R. Ponnala, *High-dose hook effect.* Journal of Dr. NTR University of Health Sciences, 2014. **3**(1): p. 5-7.
138. D'Almeida, A.P.L., et al., *α-bisabolol-loaded lipid-core nanocapsules reduce lipopolysaccharide-induced pulmonary inflammation in mice.* Int J Nanomedicine, 2017. **12**: p. 4479-91.
139. Williams, O.W., et al., *Airway mucus: From production to secretion.* Am J Respir Cell Mol Biol, 2006. **34**(5): p. 527-36.
140. Knudsen, K.B., et al., *In vivo toxicity of cationic micelles and liposomes.* Nanomedicine, 2015. **11**(2): p. 467-77.
141. Kedmi, R., N. Ben-Arie, and D. Peer, *The systemic toxicity of positively charged lipid nanoparticles and the role of Toll-like receptor 4 in immune activation.* Biomaterials, 2010. **31**(26): p. 6867-75.
142. Vasievich, E.A., W. Chen, and L. Huang, *Enantiospecific adjuvant activity of cationic lipid DOTAP in cancer vaccine.* Cancer Immunol Immunother, 2011. **60**(5): p. 629-38.

143. Vasievich, E.A., et al., *Trp2 peptide vaccine adjuvanted with (R)-DOTAP inhibits tumor growth in an advanced melanoma model.* Mol Pharm, 2012. **9**(2): p. 261-8.
144. Terp, M.C., et al., *Differential efficacy of DOTAP enantiomers for siRNA delivery in vitro.* Int J Pharm, 2012. **430**(1-2): p. 328-34.
145. Voiriot, G., et al., *Interleukin-6 displays lung anti-inflammatory properties and exerts protective hemodynamic effects in a double-hit murine acute lung injury.* Respir Res, 2017. **18**.
146. Lima Trajano, E.T., et al., *Endotoxin-induced acute lung injury is dependent upon oxidative response.* Inhal Toxicol, 2011. **23**(14): p. 918-26.
147. Kalyanaraman, B., et al., *Measuring reactive oxygen and nitrogen species with fluorescent probes: challenges and limitations.* Free Radic Biol Med, 2012. **52**(1): p. 1-6.